



HAL
open science

Hard X-ray spectroscopy of biomolecules and organic polymers

Nicolas Velasquez

► **To cite this version:**

Nicolas Velasquez. Hard X-ray spectroscopy of biomolecules and organic polymers. Astrophysics [astro-ph]. Sorbonne Université, 2023. English. NNT : 2023SORUS445 . tel-04443923

HAL Id: tel-04443923

<https://theses.hal.science/tel-04443923>

Submitted on 7 Feb 2024

HAL is a multi-disciplinary open access archive for the deposit and dissemination of scientific research documents, whether they are published or not. The documents may come from teaching and research institutions in France or abroad, or from public or private research centers.

L'archive ouverte pluridisciplinaire **HAL**, est destinée au dépôt et à la diffusion de documents scientifiques de niveau recherche, publiés ou non, émanant des établissements d'enseignement et de recherche français ou étrangers, des laboratoires publics ou privés.



Sorbonne University

Doctoral School 388

Discipline: Physical Chemistry

Doctoral thesis

Defended on November 14, 2023

Hard X-ray spectroscopy of biomolecules and organic polymers

by

Nicolas Sebastian VELASQUEZ GONZALEZ

Members of the Jury

Tatiana MARCHENKO

Thesis Director

Bernd WINTER

Reviewer

Philippe WERNET

Reviewer

Caterina VOZZI

Examiner

Jean-Hugues FILLION

Jury President, Examiner

Laurent NAHON

Examiner

to my loved ones

Exploding is a perfectly normal medical phenomenon

Graham Chapman

Contents

Contents	vii
Abstract	xi
Résumé	xiii
1 Introduction	1
1.1 Aim and outline	2
1.2 Background	4
1.2.1 Core-ionization, core-excitation & relaxation	5
1.2.2 Normal Auger decay & Post-collision interaction	7
1.2.3 Resonant Auger Spectroscopy	9
1.2.4 Core-hole Clock Spectroscopy	13
1.2.5 Charge Transfer	16
2 Experimental methodology	23
2.1 Synchrotron radiation	24
2.1.1 X-ray generation	24
2.2 SOLEIL Synchrotron	30
2.2.1 GALAXIES beamline	31
2.2.2 HAXPES end-station	32
2.3 Data analysis and treatment	40

2.3.1	Energy calibration	41
2.3.2	Resolution	42
2.3.3	Energy referencing in condensed matter systems	44
2.4	Systems studied	47
2.4.1	Gas phase: thiophene	47
2.4.2	Liquid phase: L-cysteine	49
2.4.3	Solid state: polymers	49
3	Post-collision interaction: from gas phase to solid state	53
3.1	Introduction	54
3.2	Theoretical description	57
3.2.1	Electron effective attenuation length	63
3.3	Experiment	65
3.4	Results and Discussion	69
3.5	Conclusion	74
4	Electron delocalization in conjugated polymers	77
4.1	Introduction	78
4.2	Experiment	81
4.3	Theory	84
4.3.1	Core-hole clock spectroscopy	84
4.3.2	Computational Methods	86
4.4	Results and Discussion	89
4.4.1	Experimental data analysis	89
4.4.2	Computational analysis	95
4.5	Conclusion	104
5	Charge transfer in aqueous L-cysteine	105
5.1	Introduction	106
5.2	Experiment	109

5.3	Theory	111
5.3.1	Core-hole clock spectroscopy	111
5.3.2	Computational methods	111
5.4	Results and Discussion	113
5.4.1	Resonant electron delocalization	122
5.4.2	CT above the ionization threshold	125
5.5	Computational analysis	128
5.6	Conclusion	131
6	Conclusion and perspectives	133
	Bibliography	139
	Acknowledgments	167

Abstract

Hard X-ray synchrotron radiation gives access to ultrafast electron dynamics. By studying core-excitation and decay events, it is possible to probe electron dynamics in a wide range of materials. This thesis describes experimental and theoretical approaches on the interaction of X-rays with systems in the gas phase, in solution, and in the solid state. Through Auger electron spectroscopy and theoretical modeling within the eikonal approximation framework we observed the post-collision interaction (PCI) effect manifested in the organic molecule thiophene and π -conjugated polymers polythiophene (PT) and poly(3-hexylthiophene-2,5-diyl) (P3HT). By means of the core-hole clock spectroscopy (CHCS) technique and ab initio theoretical methods, we observed and quantified ultrafast electron dynamics in the form of electron delocalization in PT and P3HT, shedding light on the electron delocalization mechanism upon resonant excitation with hard X-rays. In solvated systems, where coupling of nuclear and electronic degrees of freedom is non-negligible, we have observed and provided a qualitative assessment of CT taking place upon resonant excitation and upon core-ionization of an aqueous solution of L-cysteine, where CT in the resonantly excited case depends on the protonation state of the amino acid. Our experimental observations provided by Auger electron spectroscopy are supported by preliminary ab initio theoretical techniques.

Résumé

Le rayonnement synchrotron à rayons X durs permet d'accéder à la dynamique ultrarapide des électrons. En étudiant les événements d'excitation et de désexcitation du noyau, il est possible de sonder la dynamique des électrons dans une large gamme de matériaux. Cette thèse décrit les approches expérimentales et théoriques de l'interaction des rayons X avec des systèmes en phase gazeuse, liquide ou solide. Grâce à la spectroscopie électronique Auger et à la modélisation théorique dans le cadre de l'approximation eikonale, nous avons observé l'effet de l'interaction post-collision (PCI) qui se manifeste dans la molécule organique thiophène et dans les polymères conjugués polythiophène (PT) et poly(3-hexylthiophène-2,5-diyl) (P3HT). En utilisant la technique de *core-hole clock spectroscopy* (CHCS) et les méthodes théoriques *ab initio*, nous avons observé et quantifié une dynamique électronique ultrarapide sous la forme d'une délocalisation électronique dans le PT et le P3HT, cela met en lumière le mécanisme de délocalisation électronique lors d'une excitation résonnante avec des rayons X durs. Dans les systèmes solvatés, où le couplage des degrés de liberté nucléaires et électroniques n'est pas négligeable, nous avons observé et fourni une évaluation qualitative de la CT qui a lieu lors de l'excitation résonnante et de la core-ionisation d'une solution aqueuse de l'acide aminé L-cystéine. Dans le cas de l'excitation résonnante, la CT dépend de l'état de protonation de l'acide aminé. Nos observations expérimentales fournies par la spectroscopie d'électrons Auger sont étayées par des techniques théoriques *ab initio* préliminaires.

Chapter 1

Introduction

1.1 Aim and outline

My thesis is part of the Marie Skłodowska-Curie Innovative Training Network **SMART-X: Study of carrier transport in MAterials by time-Resolved specTroscopy with ultrashort soft X-ray light**. Its focus is to bring together ultrafast X-ray spectroscopy and novel theoretical approaches to explore charge carrier dynamics in energy-related materials. As such, the aim of this thesis is to investigate fundamental aspects which may help pave the way towards application-focused studies. More specifically, the goal is to explore electron dynamics in systems of varied and increasing complexity, such as organic polymers and biomolecules in solution, of relevance in biological fields, environmental issues, and industrial applications.

Conjugated organic polymers are excellent targets in which to explore electron dynamics, due to their significant relevance in photo-voltaics, opto-electronics and solar cells. The systems of choice consist of thiophene-based polymers: polythiophene (PT) and poly(3-hexylthiophene-2,5-diyl), commonly known as P3HT. Both, PT and P3HT were showcased in our investigations of post-collision interaction (PCI) in Chapter 3, and ultrafast charge transfer, in Chapter 4. As biological functions and chemical reactions take place in the liquid phase, shedding light on fundamental phenomena in solvated systems is a significant challenge to address. The biomolecule in focus is the amino acid L-cysteine, with it, we explore charge transfer phenomena occurring in aqueous solution, in Chapter 5.

While there is an abundance of different light sources and methods to study electron dynamics, such as lasers, free-electron lasers and synchrotrons, we choose the latter. Hard X-rays from synchrotrons provide us with 1) element- and site-specificity, which allows for localized excitation in extended complex systems, and 2) access to short timescales, which allows us to investigate ultrafast dynamics taking place at the low femtosecond and down to the attosecond regime.

The main physical processes involved in this thesis work, such as core-excitation, core-ionization and decay, will be presented in the following section. In Chapter 2, is presented an account of the experimental methodology, delving into the techniques, data treatment, and sample preparation. The results are comprised of Chapters 3, 4, and 5.

Chapter 3 concerns a comparative study of the PCI effect as observed in thiophene and thiophene-based polymers. Our motivation was to apply the knowledge of PCI, already obtained for atomic and small molecular targets in the gas phase, to extended solid state systems. Such systems can be probed with X-ray photoelectron spectroscopy (XPS) and Auger electron spectroscopy (AES), whose accuracy greatly relies on a meticulous interpretation of the spectrum, which can be substantially affected and influenced by the PCI effect. As such, developing a generalized framework through which to describe the PCI mechanism in condensed matter was of significant practical interest.

In Chapter 4, the hard X-ray core-hole clock spectroscopy (CHCS) technique is introduced. CHCS allowed for the observation of ultrafast electron dynamics in two types of thiophenic polymers. The scientific question addressed is the charge transfer phenomenon, a long-standing, well established research subject, with wide-spread implications in life sciences, chemistry and applied materials sciences. Our chief goal was to elucidate the charge transfer mechanism during core-excitation and decay in conjugated polymers.

In Chapter 5, we investigate charge transfer in the solvated amino acid L-cysteine. Studying amino acids, the building block of proteins, is a step further in attempting to explain electron dynamics taking place in the liquid phase, as a vast array of biochemical functions are carried out by proteins in solution.

Lastly, Chapter 6 is reserved for the conclusions of the thesis and perspectives, with a discussion of the possible and potential applications of the presented work.

1.2 Background

Light matter interaction

Whenever someone looks in a mirror, they are witnessing the interaction between light and matter. The response of highly conductive materials which are rich in free electrons, to electromagnetic radiation in the visible range, translates to an efficient reflection at any given angle. Reflectivity, refraction, and diffraction are some examples of light matter interaction. Shining a green laser pointer on a container with olive oil will produce a change in the color of the light from green to red: the green light is absorbed by chlorophyll molecules in the oil which, in turn, emit red light. A common green laser pointer has a wavelength of 520 nm or ~ 2.4 eV, while the energy needed to eject a S 1s photoelectron is approximately 2.4 keV. This type of *ionizing* radiation falls in the X-ray range of the electromagnetic spectrum. While the distinction between soft and hard X-rays is hazy, in this thesis hard X-rays have energies $\hbar\omega > 1$ keV.

1.2.1 Core-ionization, core-excitation & relaxation

With X-rays, it is possible to probe core-level orbitals in a target system: depending on the incident photon energy, an electron may be promoted to an unoccupied bound state (resonant core-excitation) or it may be ejected into the continuum (core-ionization), as described in Fig. 1.1.

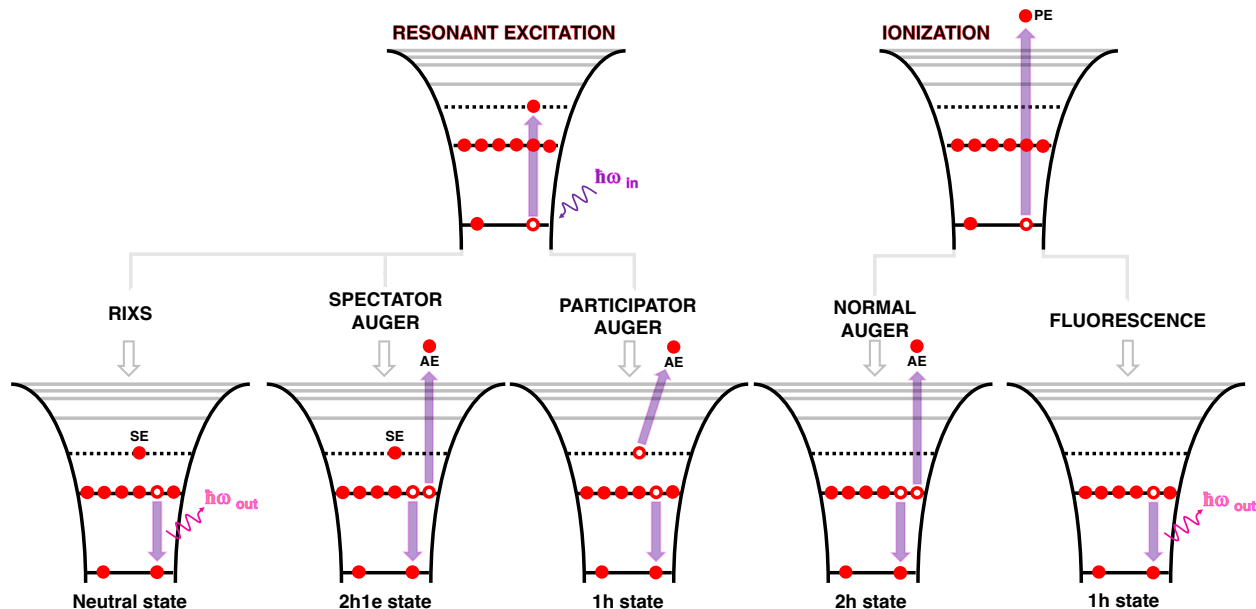


Figure 1.1: Schematic of excitation and decay events –both radiative and non-radiative– upon absorption of an X-ray photon ($\hbar\omega_{in}$). In the non-radiative case, core-ionization with emission of a photoelectron (PE) is followed by normal Auger decay with emission of an Auger electron (AE) leading to a two-hole (2h) final state. Resonant excitation to an unoccupied molecular orbital (dotted line) leads predominantly to resonant spectator Auger decay, when the spectator electron (SE) remains localized in the vicinity of the excited atom, resulting in a two-hole one-electron (2h1e) final state. Alternatively, in participator Auger decay, the promoted electron participates in the decay process, which leads to a single hole (1h) final state. In the radiative case, core-ionization with emission of a photoelectron (PE) is followed by the radiative decay in which a photon ($\hbar\omega_{out}$) is emitted via fluorescence, resulting in a 1h final state. Resonant excitation leads to emission of a photon ($\hbar\omega_{out}$) via resonant inelastic X-ray scattering (RIXS), resulting in a neutral final state.

If the energy of the incident photon is sufficient to overcome the binding energy E_b of an electron, then photoionization will occur, in which a photoelectron will be ejected.

$$E_{kin} = \hbar\omega - E_b. \quad (1.1)$$

The photoelectric effect, first observed and detected by Hertz [1], and later explained by Einstein [2], states that the kinetic energy E_{kin} of the detected photoelectron is linked to incident photon energy $\hbar\omega$, and to the binding energy as indicated in Eq. 1.1, which is the fundamental premise upon which photoelectron spectroscopy (PES) is built.

Core-ionization and core-excitation, both result in a highly unstable system. In a core-ionization event, upon emission of a photoelectron, the system has two available channels of relaxation: Auger decay and X-ray emission. Non-radiative Auger decay represents the major decay channel in light elements ($Z \leq 20$), while radiative decay in the form of fluorescence considerably dominates relaxation as the atomic number Z increases, as described in Fig. 1.2.

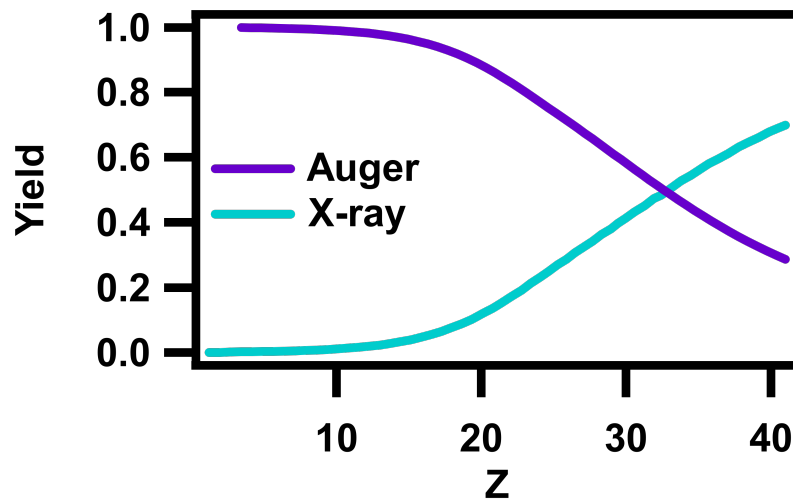


Figure 1.2: Fluorescence and Auger electron emission yields from K -shells. Adapted from [3].

X-ray emission

Relaxation may occur via radiative decay, as sketched in Fig. 1.1. When the incident photon energy is larger than the ionization threshold, the process taking place corresponds to X-ray fluorescence (XRF). Here, as the core vacancy is filled by a valence or inner-shell electron, a photon is emitted. The fluorescence spectrum contains sharp lines which are characteristic to the atom where the core vacancy was created. XRF is therefore a remark-

ably useful technique to elucidate chemical composition.

When radiative decay takes place from a core-excited system, with an electron promoted to an unoccupied orbital, the relaxation process is commonly referred to as resonant inelastic X-ray scattering (RIXS). RIXS is a very capable photon-in photon-out method that gives access to electronic properties similar to resonant Auger spectroscopy (RAS). RIXS and RAS are therefore go-to spectroscopic techniques in investigations of atomic, molecular, and extended systems, probing not only the chemical surroundings of the target atom but also dynamics taking place during the core-excitation-decay process.

1.2.2 Normal Auger decay & Post-collision interaction

Normal Auger (NA) decay occurs when the core-hole vacancy left behind by the photoelectron is filled by an electron from an outer shell, as depicted in Fig. 1.1. In the classical two-step picture, upon filling of the core-vacancy by the electron in the outer shell, the energy remaining in the system will be released via ejection of an Auger electron. This NA decay path leads to a two-hole (2h) final state. The kinetic energy of the Auger electron is determined by the binding energies of the electrons involved in the Auger process. Therefore, the Auger electron resulting from the NA process has a *constant* kinetic energy, which is independent of the incident photon energy.

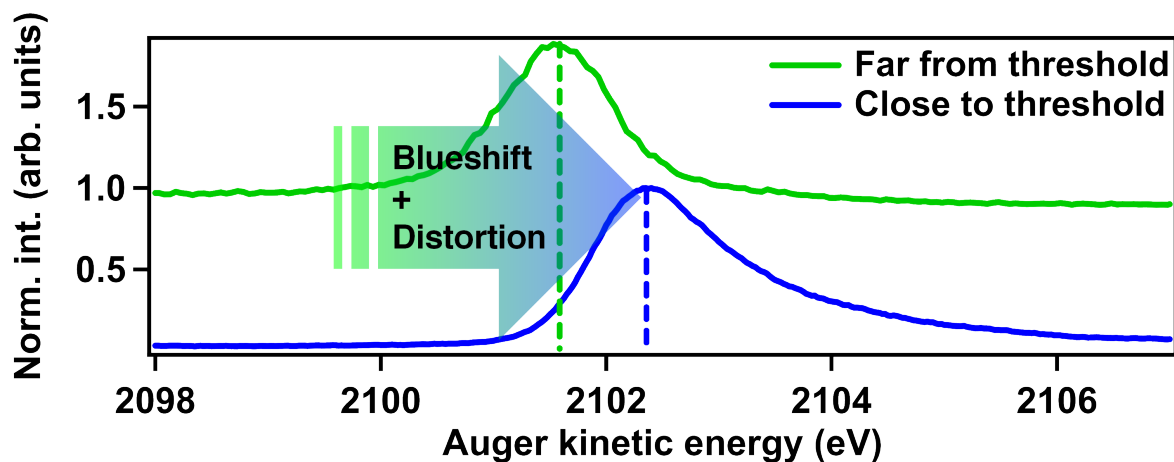


Figure 1.3: PCI-induced distortion in S *KLL* Auger electron lines.

This energy independence, however, does not hold close to the ionization potential (IP) threshold of the core-ionized atom. This is due to the Coulomb interaction between photoelectron, Auger electron and remaining ion, known as post-collision interaction (PCI), which is a broadly studied phenomenon [4–8]. PCI induces a distortion of the energy distributions of both photoelectrons and Auger electrons, as exemplified in Fig. 1.3, for the Auger case. From a classical standpoint, PCI distortion is a result of an energy exchange between the emitted Auger electron, photoelectron, and the residual cation.

A number of studies performed on small systems such as Ar and OCS, which targeted 1s-shell photoionization in the gas phase, allowed for the extraction of intermediate-state lifetime during the Auger decay cascade event through analysis of PCI-influenced photoelectron lines obtained using coincidence spectroscopy [9, 10]. A PCI *shift* (magnitude of the blueshift of the Auger electron lines measured close to the ionization threshold with respect to the normal Auger lines measured far from threshold) and distortion of Auger energy distribution was observed in Ar following core-ionization, at incident photon energies of up to 200 eV above the IP [11].

In an effort to further our understanding of PCI and how it is manifested in the solid state, we have targeted the sulfur-containing aromatic molecule thiophene and its polymers: PT and P3HT. By recording and analyzing the PCI shift in S *KLL* Auger spectra we were able to determine a stronger shift in both polymers contrasted to the isolated thiophene case [12]. Through a combined experimental and theoretical effort, based on the eikonal approximation [13], an explanation of the stronger PCI-effect manifested in the solid state case was found to arise from the combined effect of photoelectron scattering and polarization screening.

1.2.3 Resonant Auger Spectroscopy

By taking advantage of the properties of synchrotron light, such as energy tunability and high monochromaticity, an electron can be resonantly promoted from a core-shell to a specific unoccupied orbital, as depicted in Fig. 1.1, leading to resonant core-excitation. In the non-radiative scenario, the unstable system may decay in two ways. In the first one, the promoted *spectator* electron remains localized in the vicinity of core-hole, and does not participate in the relaxation process. Here, a valence or inner-shell electron fills the vacancy, with concomitant ejection of a resonant Auger electron. Resonant spectator Auger decay leads to a two-hole one-electron final state (2h1e). The second decay path, involves the promoted electron which actively participates in the decay event, being ejected upon filling of the core vacancy. Resonant participator Auger decay leads to a one-hole final state (1h). Generally, the relative intensity of the participator decay channel is significantly lower than that of the spectator. For inner-shell core-holes, the promoted electron has a higher probability of remaining localized in a bound state than to participate in the Auger process. The *participator* Auger decay final state can also be attained by UV photoelectron spectroscopy. In spectator Auger decay, the kinetic energy of the spectator electron lines may experience a blueshift with respect to the normal Auger electron kinetic energy. This effect, called *spectator shift*, is a result of the screening of the promoted electron acting on the core-hole in the intermediate state and the two holes of the 2h1e final states. All peaks in the spectator Auger spectrum shift by a constant value, with respect to the kinetic energy of the normal Auger line.

Auger resonant Raman effect

When the incident photon bandwidth is narrower than the lifetime broadening of the core-excited state, a RAS experiment is compliant with the so-called Auger resonant Raman (ARR) *conditions*. Under ARR conditions, two effects can be observed. First, a linear dispersion of the spectator Auger lines as a function of the incident photon energy may be detected [14]. Second, if the photon energy is tuned to the resonance, the peaks cor-

responding to the resonant Auger decay channel will experience narrowing [15]. The combined manifestation of these two phenomena is commonly referred to as the ARR *effect*, and it was first observed and reported by Brown et al. and Armen et al., in gaseous Xe and Kr [16–19].

In the atomic case, the physical explanation behind linear dispersion stems from energy conservation. Upon resonant Auger decay, the energy imparted by the incident photons is carried away by the ejected resonant Auger electron. To describe narrowing, we must first introduce the lineshape which characterizes lines in decay spectra. Among the factors that may determine the shape and width of lines are: 1) width of the absorption line, defined as a Lorentzian, 2) experimental contributions, which may be defined as a Gaussian shape. These experimental contributions contain the monochromator function, and the analyzer function. Additionally, contributions from final states may have to be accounted for, which are defined as a Lorentzian shape. The latter contributions may be neglected in some cases, as the width of the final state may be considerably small with respect to the other factors. However, in the hard X-ray case convolution with the natural width of the final state may have to be carried out to describe the Auger energy distribution [20,21]. Lastly, with high kinetic energy electrons, Doppler broadening contributions must be considered.

Within the non-radiative resonant Raman scattering theory [14, 20, 22, 23], resonant core-excitation and decay are considered as a single scattering process, in which an electron in an initial electronic ground state of energy E_o is promoted to an electronic final state of energy E_f due to interaction with an incident photon with energy $\hbar\omega$, resulting in ejection of a resonant Auger electron of energy $E_{\text{Auger}} = \hbar\omega - (E_f - E_o)$ and a mono-cationic final state. The intermediate resonantly core-excited state becomes a band-pass filter, which results in a "selection" of incident photons centered at the nominal resonant excitation energy $\hbar\omega_i$, limited by the Lorentzian lifetime broadening Γ_i of the resonant state with a lineshape $L_i(\hbar\omega - \hbar\omega_i, \Gamma_i)$.

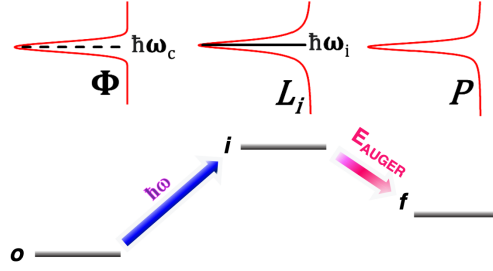


Figure 1.4: Schematic of three-step core-excitation and Auger decay processes, with one intermediate and one final state. The photon energy distribution Φ , is centered at $\hbar\omega_c$. In an experimental setting, Φ can be approximated to have a Gaussian shape. The Lorentzian distribution L_i of the core-excited state has a nominal resonant excitation energy $\hbar\omega_i$. P is the Auger electron energy distribution. Dashed and solid lines indicate the center of mass of $\hbar\omega_c$ and $\hbar\omega_i$, respectively. Initial (ground), intermediate (core-excited), and final states labeled as o, i, f , respectively. Adapted from [20].

In the case of broadband excitation, the probability P of absorption of an incident photon and ejection of an Auger electron, is therefore defined by the Lorentzian distribution $L_i(\hbar\omega - \hbar\omega_i, \Gamma_i)$. The probability reaches a maximum at the nominal resonant excitation energy $\hbar\omega_i$ leading to emission of a resonant Auger electron with a nominal kinetic energy $E_{\text{Auger } 0}$.

In the general case, the Lorentzian component $L_i(\hbar\omega - \hbar\omega_i, \Gamma_i)$ must be convoluted the spectral function $\Phi(\hbar\omega - \hbar\omega_c, \Gamma_p)$ with a centroid $\hbar\omega_c$, and width Γ_p (photon bandwidth). However, under a three-step model approximation for an excitation and decay event, consisting of a single intermediate state and a single stable final state, as illustrated in Fig. 1.4, the energy distribution of the Auger electron $P(E_{\text{Auger}})$ is given by the product

$$P(E_{\text{Auger}}) \propto \Phi(\hbar\omega - \hbar\omega_c, \Gamma_p) L_i(\hbar\omega - \hbar\omega_i, \Gamma_i). \quad (1.2)$$

If the distributions $L_i(\hbar\omega - \hbar\omega_i, \Gamma_i)$, and $\Phi(\hbar\omega - \hbar\omega_c, \Gamma_p)$ should be very dissimilar, the overall shape of the distribution will be determined by the narrower one. Under ARR conditions –when the width Γ_p of the photon energy distribution is indeed narrower than the natural broadening Γ_i of the core-excited intermediate state– the linewidth of the

spectral features will therefore be defined by the photon energy distribution. In other words, when the incident photon energy exciting the target has a narrower bandwidth than the lifetime broadening of the target system, the latter may essentially be "removed" from the resonant Auger lines. In Fig. 1.4, the ideal case when the incident photon energy is tuned exactly to the resonant excitation energy is shown ($\hbar\omega_c = \hbar\omega_i$). Only in this case will the Auger electron energy distribution be centered at the nominal kinetic energy $E_{\text{Auger } 0}$. Upon detuning from the resonance, the maximum of the Auger electron energy distribution shifts, and it no longer matches $E_{\text{Auger } 0}$. The detuning is described by Eq. 1.3.

$$\Omega = \hbar\omega_c - \hbar\omega_i. \quad (1.3)$$

When compliant with ARR conditions, a narrow photon bandwidth will cause the Auger electron energy distribution to display a dispersive behavior as a function of Ω , which is unerringly linear for the case of isolated atoms, while in molecules, nonlinear dispersion reflecting bond elongation, a sign of nuclear dynamics, may be observed [24]. The dispersive behavior is of the Auger electron lines against the detuning Ω described by Eq. 1.4

$$E_{\text{Auger}} = E_{\text{Auger } 0} + \Omega. \quad (1.4)$$

As indicated by Eq. 1.4, and recalling that $E_{\text{Auger}} = \hbar\omega - (E_f - E_o)$, the kinetic energy of the Auger lines follows the energy conservation or Raman dispersion law.

To describe the observed lineshapes, we must consider the experimental contribution originating from the electron analyzer. The finite resolution of the latter takes the form of spectrometer broadening, with a width Γ_g . Consequently, the Auger electron energy distribution $P(E_{\text{Auger}})$ has to be convoluted with the Gaussian-shaped spectrometer

function [25,26].

1.2.4 Core-hole Clock Spectroscopy

In order to unveil ultrafast dynamical processes in molecules and systems of higher complexity, timescales ranging from the low femtosecond, down to the attosecond regime become a necessity. Electron dynamics span attosecond timescales, while nuclear dynamics do so in the femtosecond regime.

In this ultrafast regime, exploration of dynamics can be done through time-resolved techniques or by taking advantage of the internal clock present in the target system. While the time-resolved approach makes use of short-pulsed excitation sources, the internal clock approach or core-hole clock spectroscopy (CHCS) technique has no such requirement. As an example, in third row elements, the $1s$ -shell lifetime ranges between ~ 900 attoseconds to 3 femtoseconds. These timescales are accessible through the CHCS technique, provided the experiment complies with ARR conditions, which enables us to investigate ultrafast processes [14,27].

As the name implies, CHCS takes advantage of the core-hole lifetime τ_{CH} , to use as a "stop watch" for processes occurring in the system investigated. τ_{CH} is determined by the core-hole lifetime broadening Γ of the core-excited state of a spectral feature in X-ray absorption or photoemission spectra, as described by Eq. 1.5

$$\tau_{CH} = \frac{\hbar}{\Gamma}. \quad (1.5)$$

Upon creation of an inner-shell vacancy, the resulting core-excited state is highly unstable and undergoes relaxation through emission of Auger electrons and/or X-rays. If another process occurs in the system on the same timescale as the core-hole lifetime, it will be reflected on the spectrum. This is the basis behind CHCS.

The lifetime provides a time-window to observe processes taking place on femto-second to attosecond timescales upon core-excitation [27–31]. It is possible to take advantage of the detuning Ω (Eq. 1.3) to manipulate core-excitation and decay events [25, 32–35]. Detuning away from the resonant excitation energy provides a tool with which to influence the scattering event. The *effective scattering lifetime* (τ_{eff}), can describe the duration of the scattering event, as described by Eq. 1.6 [25, 34]

$$\tau_{eff} = \frac{\hbar}{\sqrt{\Omega^2 + \Gamma^2}}. \quad (1.6)$$

During an experiment, τ_{eff} is controlled through Ω . As Ω increases, τ_{eff} decreases. When $\Omega = 0$, $\tau_{eff} = \tau_{CH}$. By having command over τ_{eff} , we can influence the system, e.g., we can shorten the observation window in our measurements.

A concrete example of the successful application of the technique is in allowing for the manipulation of molecular fragmentation during ultrafast dissociation (UFD) processes. This was demonstrated in ref. [36], by Travnikova et al., where through RAS, it was shown that multistep UFD in HCl could be controlled by tuning the incident photon energy, leading to significant changes in nuclear dynamics taking place at the attosecond timescale. Moreover, formation of atomic fragments depends on the sign of the detuning: positive detunings lead to a decrease in fragment formation due to interplay between potential energy gradients and τ_{eff} , both of which depend on the incident photon energy [36]. This is illustrated in Fig. 1.5.

Another example of CHCS showcased through RIXS in a study of CH₃I and CH₃Cl, where dispersion of the emission lines was drastically different in the two halogens. While in CH₃Cl, the dispersion of the peak position is significantly nonlinear across the resonance, CH₃I displays a minor deviation from linearity of the emission lines [37]. In CH₃Cl, the lifetime is ~ 1 femtosecond at the Cl *K*-shell, which allows for nuclear dynamics. Contrarily, CH₃I has an *L*-shell lifetime of ~ 200 attoseconds,

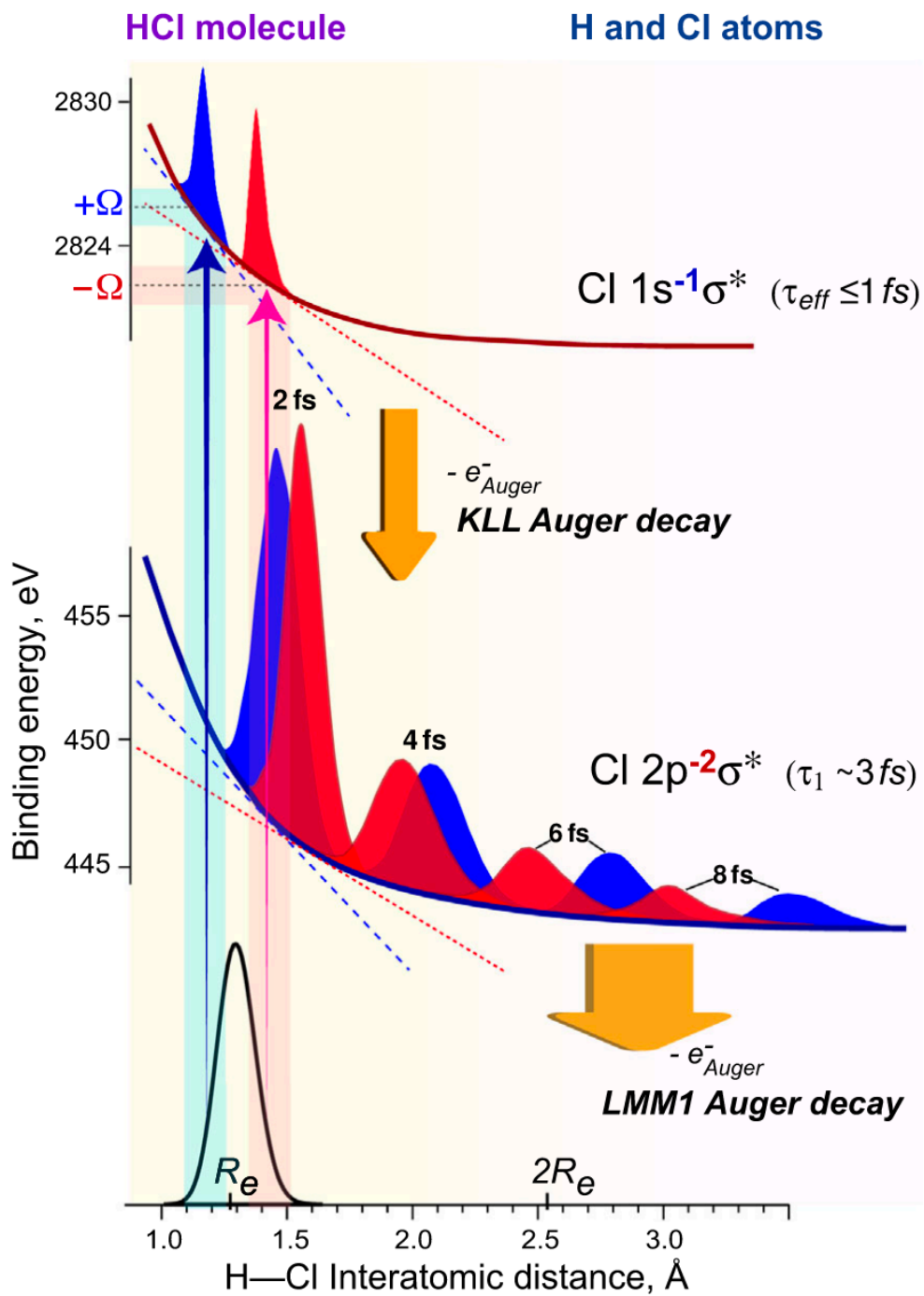


Figure 1.5: Energy gradient effect on wave packet dynamics in Auger decay for positive (blue) and negative (red) detunings Ω . Used with permission from [36].

impeding energy transfer to the nuclei before emission of a photon [37].

1.2.5 Charge Transfer

In chemical systems, charge transfer (CT) frequently acts as the guiding entity controlling the sequence of interactions upon electronic excitation of the target systems [31]. While CT may occur on time-scales as lengthy as milliseconds, in this thesis, charge transfer refers to the process through which an electron is delocalized on timescales comparable to the core-hole lifetime, a feat made possible by the CHCS method. Ultrafast electronic processes can also be probed with attosecond resolution [38], where the use of isolated pulses has opened the door to explorations of increasingly complex systems [39]. Combining attosecond pulses with wavelengths in the X-ray regime is at the forefront of developments taking place at, i.e., free-electron lasers [40,41], which promise exploration of X-ray induced attosecond dynamics directly in the time domain.

As opposed to the more common way of studying dynamics directly in the time domain (commonly through pump-probe laser spectroscopy techniques), the CHCS method offers element-specific core-shell excitation, an essential requisite when CT processes involve complex systems with non-negligible nuclear and electron dynamics.

Our understanding about ultrafast dynamical processes has deepened as the state-of-the-art has evolved. Before the CHCS technique became feasible, shake-up features due to charge transfer were observed to occur in alkaline and alkaline earth metals from the 3rd and 4th row [42]. Using synchrotron light, allowed for the observation of CT on a femtosecond timescale by employing the CHCS technique already three decades ago, as demonstrated by Björneholm et al., where, CT was detected in both chemi-sorbed and physi-sorbed model systems on different substrates [43].

In a highly complex system such as genomic DNA, observation of dynamics by CHCS unraveled an additional electron delocalization mechanism occurring on a sub-femtosecond timescale [44]. This highlights both the importance and the motivation

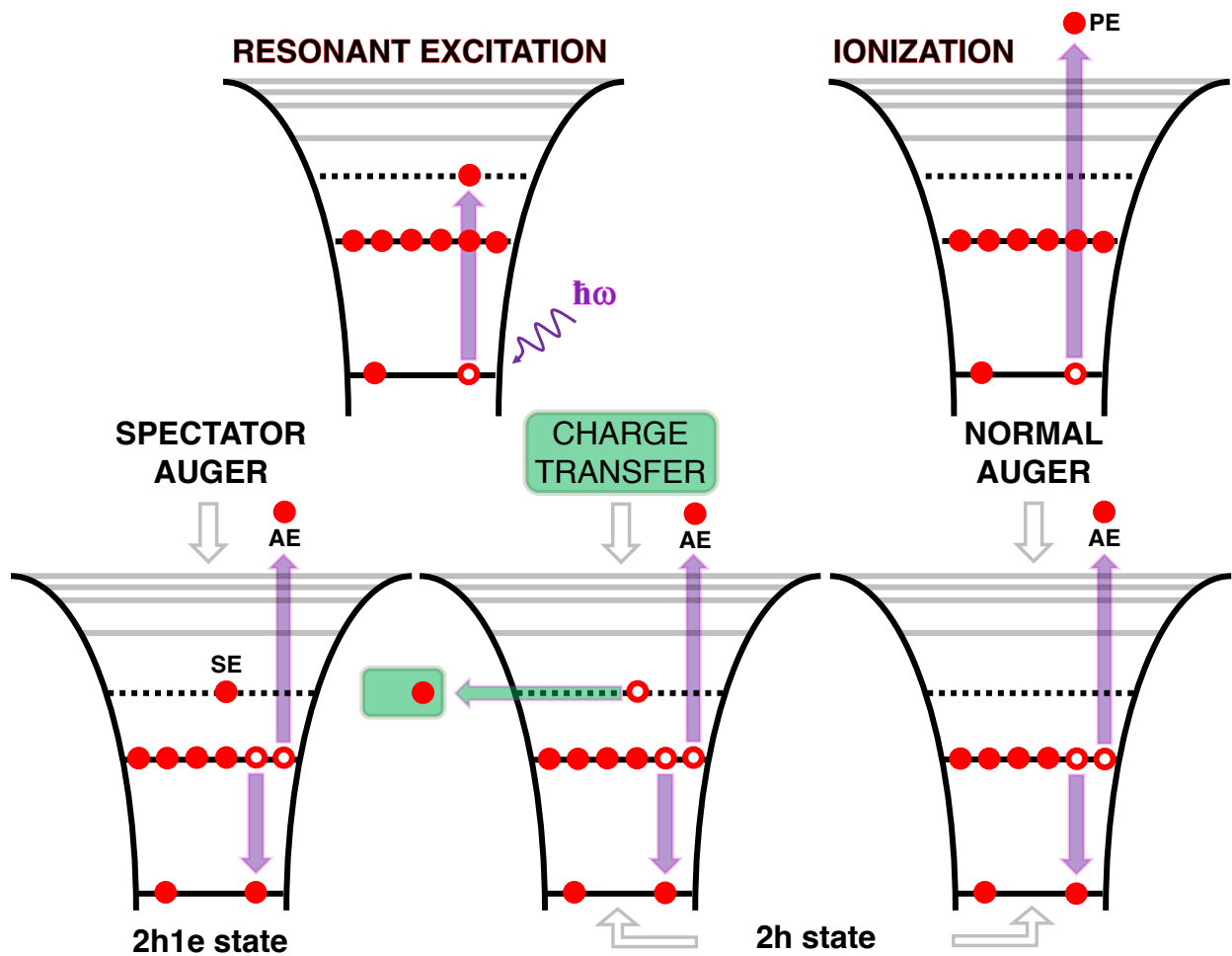


Figure 1.6: Schematic of excitation and decay events upon absorption of an x-ray photon. Ionization with emission of a photoelectron (PE) is followed by the normal Auger decay with emission of an Auger electron (AE). Resonant excitation leads to resonant spectator Auger decay, when the spectator electron (SE) remains localized on the excited atom, or, to a CT decay channel, occurring in the case of delocalization of the resonantly promoted electron to the environment. Green box represents destination environment of the delocalized electron. The spectator Auger decay leads to a mono-cationic final state (2h1e), whereas both the CT and the normal Auger decay channels lead to a di-cationic (2h) final state.

for exploring ultrafast delocalization in extended systems: in the DNA molecule, charge transfer can be taken advantage of to diagnose radiation-induced damage and repair of DNA [45].

As described earlier, a core-shell electron can be resonantly promoted to an unoccupied molecular orbital. Provided favorable conditions, delocalization of the promoted electron towards the environment is possible, as depicted in Fig. 1.6. Relaxation upon delocalization is akin to normal Auger decay, where the final state is locally di-cationic (2h), and the Auger electron energy is constant and close to the energy of the NA line. Due to the screening of the inner-shell vacancies by the spectator electron, the resulting spectator Auger kinetic energy is blueshifted with respect to the NA line. The presence of the spectator shift is paramount, allowing for the separation of the spectator Auger channel and the CT channel when the incident photon energy matches the resonant excitation photon energy.

The timescale of CT (τ_{CT}) in a core-excited state can be detected via the CHCS technique in the following way [30,31,46]:

$$\tau_{CT} = \tau_{CH} \times \frac{I_{Raman}}{I_{CT}}, \quad (1.7)$$

where I_{Raman} , and I_{CT} correspond to the integrated intensities of the resonant Raman (spectator), and charge transfer channels, respectively. The S 1s vacancy has a core-hole lifetime $\tau_{CH} \approx 1$ femtosecond [47]. We apply this method to reveal CT in two types of media: conjugated polymers and solutions.

CT in π -conjugated polymers

A promising type of materials of considerable importance to opto-electronics, photo-voltaics, and organic solar cells are conjugated polymers [48–51]. In conjugated polymers, conductivity of the electron takes place along the delocalized π -electrons which extend

over the carbon atoms forming part of the conjugated (alternating single and multiple bonds) framework. One such type of π -conjugated polymer is polythiophene (PT), a sulfur heterocycle compound, which earned Heeger et al., the Nobel Prize in Chemistry at the turn of the millennium [48]. An earlier investigation of PT in powder form using CHCS yielded inconclusive results as to the conductive properties of the sample [52]. In the study, focusing on resonant Auger spectra measured around the sulfur K-edge, there was no discernible trace of delocalization. Electron delocalization properties were investigated in an ensuing study [53], where through a RAS experiment, evidence of charge transfer was found on a PT film. The investigators ascribed their findings to the order present in the film and polymer chain interaction. In a film, the sample has a highly ordered structure, contrary to the case of powders where the polymer is completely disorganized. Structural organization, or lack thereof, may determine the mechanism through which the electron can delocalize. In powders the only delocalization channel available is *along* the polymer chain (intra-chain mechanism), while in a film, the electron may delocalize both *along* and *between* polymer chains (inter-chain mechanism). Both intra- and inter-chain mechanisms are depicted in the schematic in Fig. 1.7.

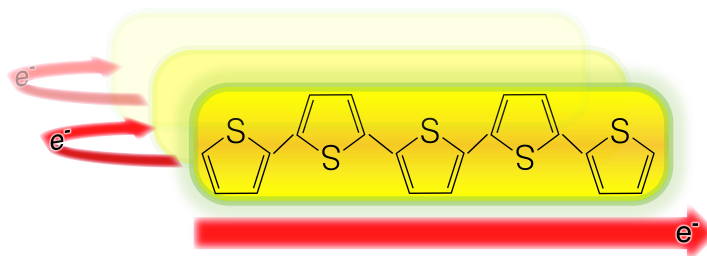


Figure 1.7: Schematic of electron delocalization mechanism. Yellow sheets represent polymer chains. In powders only the intra-chain mechanism is available (straight arrow). In ordered films, both intra- and inter-chain mechanisms are accessible to the electron (straight and curved arrows).

To gain a better insight concerning the electron delocalization mechanism, we have investigated the π -conjugated polymers: PT in powder form, and poly(3-hexylthiophene-2,5-diyl), commonly known as P3HT, as a thin film. Our aim was to verify the results and interpretation of the previous investigations in refs. [52, 53], and

elucidate the role that structural organization of the polymer chains in highly ordered films plays for CT.

CT in solvated systems

Charge transfer processes are essential for biological processes. The majority of such processes take place in the liquid phase. Furthermore, radiation damage undergone by biomolecules (e.g. DNA) occurs secondarily through radicals or ions created as water is ionized [54]. Consequently, investigating the electronic structure and dynamical processes occurring in solvated systems is crucial. The intimate correlation between the electronic structure of amino acids and their biological functions serves as a driving force for the considerable interest present in the spectroscopy of amino acids.

The presence of a carboxyl, an amino, and a thiol group in the cysteine molecule makes it a standard reference for amino acid studies. The protonation or deprotonation of these functional groups is dependent on the pH level of the solution. Extensive investigations of solvated L-cysteine were carried out using XPS in the soft X-ray range [55]. The study, which also involved various theoretical techniques, focused on understanding the protonation states of cysteine in water solutions at different pH levels, and found that the chemical shift of the S $2p$ line is markedly regulated by the protonation state of the thiol group. In a RIXS study of solvated cysteine performed in the soft X-ray regime, protonation / deprotonation effects were also observed [56].

In the soft X-ray range, the kinetic energies of photoemitted electrons fall below ~ 1 keV, constraining the mean free path to 1 nm, in turn, only allowing to perform surface-sensitive measurements. As a consequence, exploring the bulk electronic properties of a liquid sample, entails the use of hard X-ray photons and high kinetic energy electrons, with techniques such as HAXPES.

Previous X-ray absorption spectroscopy (XAS) investigations of zwitterionic L-cysteine in solution measured at the S K -edge, showed the presence of strong transitions

to orbitals of mixed character, and non-resonant features which are greatly influenced by the solvation cage around the thiol group [57]. An extended theoretical-experimental case study using transition potential density functional theory (TP-DFT) and XAS on a variety of amino acids in solution, revealed how pH significantly affects both the number and energy of transitions around the S K-edge in cysteine [58].

Our goal is to study charge transfer taking place between solute and solvent, where coupling of electronic and nuclear degrees of freedom is present. More specifically, our motivation is to investigate how the protonation state of the thiol (-SH) group in cysteine can influence the electron delocalization process.

Chapter 2

Experimental methodology

In this chapter are presented the experimental methodology and instrumentation utilized throughout the duration of the project. In order to access processes such as those addressed in this thesis, the capabilities of a synchrotron facility were needed. All experiments and results presented herein were performed using synchrotron radiation, where highly monochromatic X-ray radiation and electron spectroscopy approaches were used.

2.1 Synchrotron radiation

When charged particles traveling at relativistic speeds are subjected to a magnetic field, their trajectory follows a curved path, resulting in the emission of synchrotron radiation. The synchrotron, in essence a specific type of particle accelerator, owes his name to a pioneering paper by Ed McMillan [59], who, along with the Soviet physicist Vladimir Veksler, conceived the notion of the synchrotron [60]. Synchrotron radiation was first observed in 1947 [61], at the General Electric Research Laboratory in Schenectady, New York, where it was deemed as problematic in particle physics, as it posed a considerable source of energy loss in closed-ring accelerators [60, 62]. Not a decade later, the new possibilities that this unwanted radiation offered were described [63], which eventually birthed the first facility dedicated to regular users, the Synchrotron Ultraviolet Radiation Facility (SURF I).

For a more comprehensive account of the history of synchrotron radiation and technical details, the reader is referred to the works in [60, 62] and references therein.

2.1.1 X-ray generation

In 1895, X-ray radiation was discovered by Wilhelm C. Röntgen [64]. Ever since, X-rays have become an indispensable tool to elucidate structural properties of matter. From his findings it transpired that X-ray absorption depends strongly on the atomic number Z . When it comes to diffraction phenomena, another vast and exceptionally important application of X-rays, Max Von Laue obtained the first diffraction pattern from a copper sulfate crystal [65]. Shortly after, W. H. Bragg and his son W. L. Bragg, established the groundwork for the field of crystallography, ultimately allowing, e.g., for the determination of structural properties of molecules [64]. Investigative works involving crystallography and diffraction, while extremely important, fall outside the scope of this thesis.

After Röntgen's discovery, production of X-rays took a stride forward through the use of an X-ray tube and a rotating anode. Here, electrons are produced by a glowing

filament and then accelerated towards a metal anode. Impinging of the electrons on the anode leads to generation of X-rays. The design of this "Coolidge" tube in 1912, after W.D. Coolidge from General Electric Research Laboratory, bar minor refinements, has remained basically unchanged since its conception. One limitation exhibited by the tube, was that the intensity of the generated radiation was limited by the cooling capacity of the metal anode. It took approximately half a century for rotating anodes, which have superior heat dissipating capabilities, to be commercially available.

As depicted in Fig. 2.1, the spectral landscape of this type of X-rays consists of a continuous *bremsstrahlung* background, caused by the strong deceleration of electrons on the anode, and a sharp feature or *characteristic radiation*. The latter corresponds to fluorescence emission, characteristic for a given atomic species. This type of X-ray radiation, however, cannot be fine-tuned to a specific desired frequency. Moreover, an experiment might necessitate higher intensity than that provided by the X-ray tube. Such disadvantages are absent from synchrotron generated X-ray radiation, which can produce highly monochromatic tunable light, with a brilliance orders of magnitude higher than that of laboratory X-ray sources.

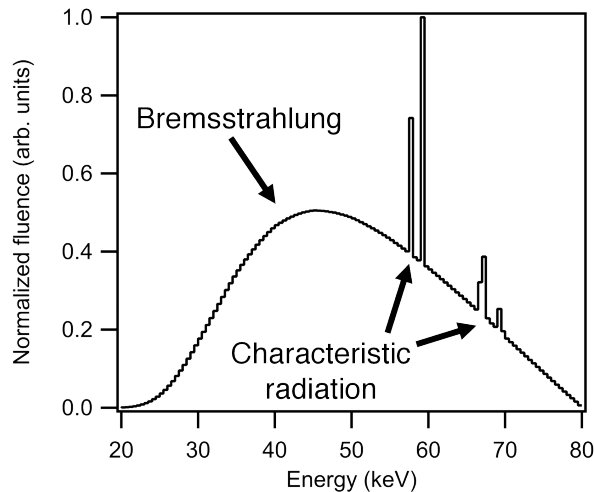


Figure 2.1: Bremsstrahlung spectrum of a 10 mm thick layer of Al at an anode angle of $\theta = 45^\circ$. Simulated using the SpekPy toolkit [66].

Second generation synchrotrons used bending magnets to alter the trajectory of the charged particles with velocities nearing the speed of light. **Bending magnets** (purple boxes in Fig. 2.2) alter the path of the electron, with the chief purpose of keeping the electrons circulating on a closed trajectory inside an evacuated storage ring. In a constant magnetic field, the result is therefore a constant acceleration of the electron beam. Synchrotron radiation from a bending magnet is of the broadband emission type.

Electrons lose energy concomitantly as synchrotron radiation is generated, which, if not restored would lead to loss of the electrons as they circle towards the storage ring walls. This is countered by the **RF cavity** (yellow box in Fig. 2.2), which supplies a steady stream of energy to counter the loss at each revolution.

Bending magnets, however, are limited in that the produced radiation is inherently tied to the properties of the magnet lattice — which houses bending magnets as well as focusing and correcting magnets — which may restrict, e.g., their peak emitted photon energy. As synchrotron facilities evolved, however, insertion devices, such as wigglers and undulators, allowed for a substantial increment in brilliance produced at synchrotrons, giving origin to new, third generation synchrotron facilities.

Wigglers are inserted in straight segments of the storage ring (blue-red boxes in Fig. 2.2), they consist of a periodic array of magnets (or a series of smaller bending magnets), in which electrons *wiggle* due to the Lorentz force exerted by the magnets. As described in Fig. 2.2, due to the left to right movement of the electrons along the x-axis, at each oscillation the electrons move twice in parallel fashion along the propagation axis of the wiggler. The resulting radiation will then be proportional to the number of wiggler periods N , and its power spectrum (as shown in Fig. 2.2, inset) will be analogous to that of the bending magnet. As a consequence of the large amplitude of the wiggles, the emission cone comes in and out of the detector, causing the emitted photons to be perceived as short pulses in the time domain, which thus produces a broad bandwidth in the energy domain, as depicted in the inset of Fig. 2.2.

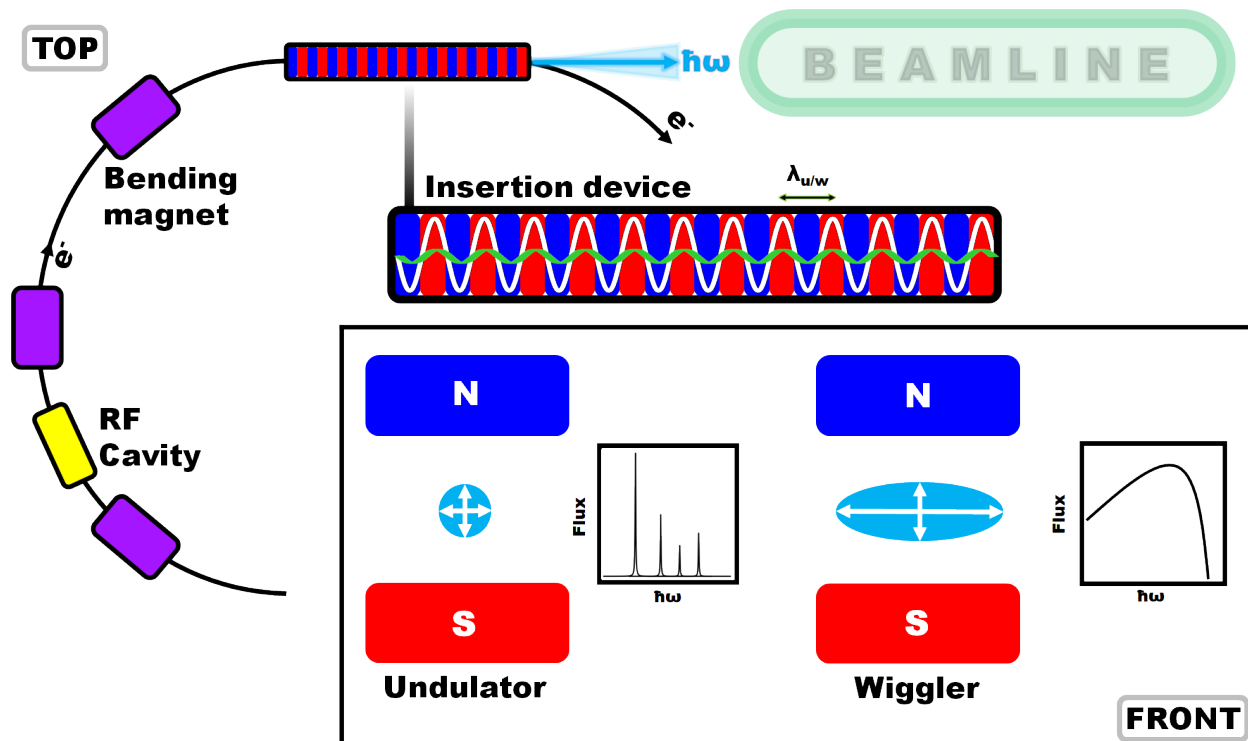


Figure 2.2: Top view schematic of an electron storage ring. Bending magnets, and radio frequency cavity shown in purple and yellow, respectively. Insertion device shown as sequential blue and red boxes (magnetic poles), with emission cones from wiggler (diverging) and undulator (arrow), shown between the insertion device and the beamline. A slightly larger insertion device schematic is also shown with white waves indicating radiation from wigglers and green waves indicating undulator radiation. In the inset to the bottom right is presented a front view of insertion device, where the radiated photon emission cone is indicated in light blue. In the inset are also presented flux vs photon energy spectra for each type of insertion device, with a qualitative representation of the intensity and shape for the emitted radiation.

The wiggler radiation opening angle Φ is inversely proportional to the relativistic correction parameter γ ,

$$\gamma = \frac{E_{electron}}{m_e c^2} = \frac{1}{\sqrt{1 - (v/c^2)}}, \quad (2.1)$$

where $E_{electron}$ is the total energy for the electron storage ring, m_e is the classical mass of the electron, c is the speed of light, and v is the electron velocity. For electrons accelerated to relativistic velocities, emitted radiation is constricted to a narrow cone along the propagation axis, where photons are emitted tangentially to the orbit of the charged particle. As hinted by the emission cones depicted in Fig. 2.2, wiggler radiation is broader than that of produced by undulators, described next.

Undulators, contrarily to the bending magnet or wiggler case, produce radiation with a spectral structure consisting of narrow bands separated at regular intervals (as depicted in the inset of Fig. 2.2). We assumed that in the wiggler case, radiation emanated from one wiggle is not dependent on the rest of the wiggles (as the photons are *seen* as short pulses by the detector). Let us imagine wiggles which are much weaker —black (smaller) oscillations in top (front) view, Fig. 2.2)—, so that their emission cone falls entirely within the detector. The result is that in time domain there will be a long pulse, which in the energy domain translates as a series of evenly spaced narrow bands, conferring monochromatic properties to radiation from the undulator. Additionally, undulators have other important characteristics arising from these weaker wiggles. Each wavefront emitted upon each wiggle movement may interfere with the other wiggles, which, if they do so destructively, removes wavelengths corresponding to destructive interference, leading to partially coherent light.

Parameters determining the properties of undulator radiation are γ , undulator period λ_u , and the undulator magnetic deflection parameter K , which in the undulator case is approximately unity, and can be fine-tuned by adjusting the gap between magnets. For undulator radiation, the vertical and horizontal components of angular divergence

$\sigma_{x,y}$ are given by:

$$\sigma_{x,y} = \frac{1}{\gamma} \left[\frac{(1 + \frac{K^2}{2})}{2mN} \right]^{1/2} \approx \frac{1}{\sqrt{mN}\gamma'} \quad (2.2)$$

where N is the number of undulator periods times 2 (number of poles), m is the harmonics index. The vertical and horizontal angular divergence components for the wiggler are given by the natural opening angle $1/\gamma$, and K/γ , respectively. In the wiggler case the magnetic deflection parameter is usually $10 < K < 50$, and can be expressed as a function of the magnetic field strength:

$$K = \frac{eB_0\lambda_u}{2\pi m_e c} = 0.934\lambda_u(\text{cm})B_0(\text{T}), \quad (2.3)$$

where e is the elementary charge, and B_0 is the maximum magnetic field strength. With the given parameters we now have an expression for the undulator wavelength:

$$\lambda = \frac{\lambda_u}{2\gamma^2} \left(1 + \frac{K^2}{2} + \gamma^2\theta^2 \right), \quad (2.4)$$

$$\theta = \frac{1}{2\gamma'}, \quad (2.5)$$

where θ corresponds to the angular divergence as seen from the frame of the observer.

Having provided a very rudimentary overview of the key variables in the generation of X-rays from relativistic electrons, a description of the *brilliance* can be given by:

$$\text{Brilliance} = \frac{\frac{\text{photons}}{\text{second}}}{(\text{mm}^2 \text{ source area}) (\text{mrad})^2 (0.1\% \text{ bandwidth})}, \quad (2.6)$$

where 0.1% originates from the convention to characterize the photon energy range as a relative energy bandwidth, due to the differences of the X-rays from different sources. Brilliance expresses how the spectral flux is distributed both spatially and angularly (phase-space).

2.2 SOLEIL Synchrotron

To make use of the brilliance and photons coming from the undulator, we, *the users*, perform our experiments at a synchrotron **beamline**. In broad terms, a beamline consists of an optical and an experimental section (commonly referred to as a hutch). As mentioned in the beginning of this chapter, all results obtained and presented in this thesis were performed using synchrotron radiation. The synchrotron facility in question is the French national synchrotron SOLEIL.

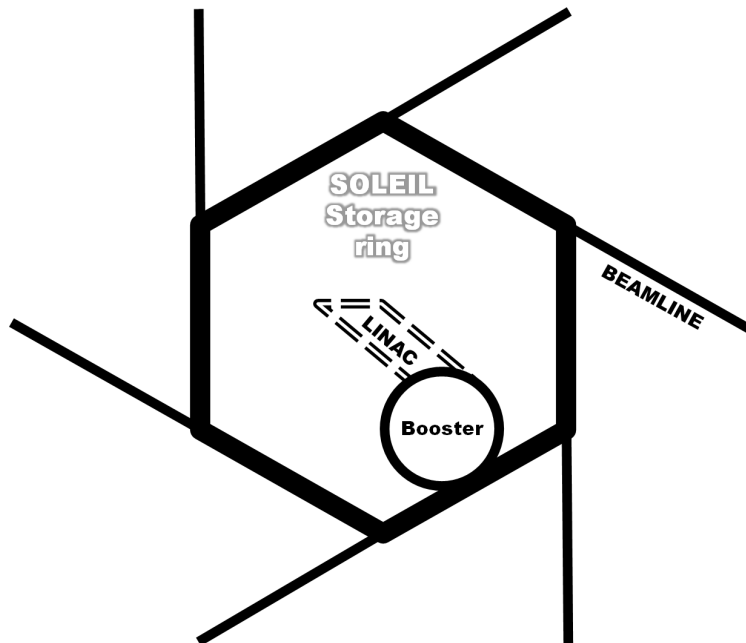


Figure 2.3: Diagram of the SOLEIL storage ring, linear accelerator, booster ring and beamlines.

The SOLEIL (Source Optimisée de Lumière d’Energie Intermédiaire du LURE) synchrotron (depicted in Fig. 2.3), located in the outskirts of Paris, France, is a third generation facility, which generates radiation ranging from far infrared to hard X-rays. At SOLEIL, electrons are first emitted as a thin beam from an electron gun, and accelerated in a linear accelerator or LINAC, where they achieve extremely high speeds with kinetic energies of ~ 100 MeV. Following acceleration, the beam then enters a circular accelerator or booster, where the energy reaches the nominal operative value for SOLEIL at 2.75

GeV, after which the electrons enter the main storage ring (indicated by the hexagonal structure in Fig. 2.3). After traveling the circumference for a determined period of time, they are subsequently converted to synchrotron radiation by the wigglers or undulators, upon which they are directed to the optical section of the beamline. The entirety of the experimental work herein presented and discussed was executed at the GALAXIES (Great beAmLine for Advanced X-ray Inelastic scattering and Electron Spectroscopy) hard X-ray beamline at SOLEIL.

2.2.1 GALAXIES beamline

The GALAXIES beamline at SOLEIL is geared towards resonant inelastic X-ray scattering (RIXS) and hard X-ray photoemission spectroscopy (HAXPES). A brief account of the beamline characteristics will be given here, while a full detailed account on the capabilities of the beamline can be found in refs. [67–69]. The optics array of the beamline, as shown in Fig. 2.4, are tailored to provide a highly focused X-ray beam, with high resolution and high flux within a photon energy range of 2.3 keV – 12 keV.

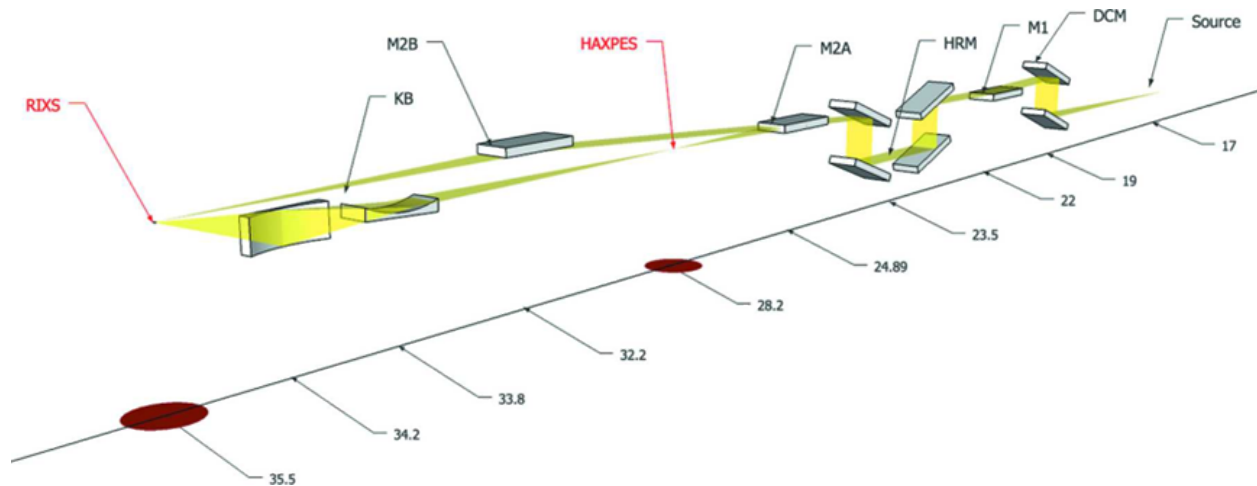


Figure 2.4: Optical layout diagram for the HAXPES and RIXS end-stations at GALAXIES. M2B: toroidal mirror used to focus the beam onto the RIXS end-station. KB: Kirkpatrick- Baez mirrors used to attain a μ -beam spot at the RIXS sample coordinates. Adapted and reproduced with permission of the International Union of Crystallography [67].

The beamline is furnished with a 20 mm-period (98 periods, 1.96 m in length)

undulator U20, which covers the aforementioned photon energy range. Incident photons are selected with a double-crystal Si(111) monochromator (DCM) with an energy resolution ΔE from 0.1 — 1 eV at 8 keV. After the impinging on the DCM, photons are reflected on the M1 spherical mirror and high-resolution monochromator (HRM). The beam is subsequently focused by the palladium-coated M2A toroidal mirror onto the HAXPES end-station.

2.2.2 HAXPES end-station

The HAXPES end-station, as shown in Fig. 2.5, is used for electron spectroscopy of samples in the gas phase, in solution and in the solid state.

It is placed in the focal plane of the M2A mirror (Fig. 2.4) [69]. The electrons emitted after the incident X-rays interact with the sample, are collected, and their kinetic energy recorded by a VG SCIENTA EW-4000 hemispherical electron analyzer. A schematic diagram of the electron analyzer is shown in Fig. 2.6. The analyzer can detect kinetic energies of up to 12 keV. At 10 keV it can provide a resolution of 35 meV [69], with high transmission, owing to the total acceptance angle of the lens (60°), which enables observation of processes with small cross-sections, e.g., double core-hole states [70], among others. Additionally, two other modes can be utilized: 1) high-angular resolution (45°), and 2) transmission mode. The analyzer is mounted on an ultra-high-vacuum experimental chamber, with the electrostatic lens placed perpendicular with respect to the incident radiation and parallel to the polarization vector of the beam. As shown in Fig. 2.6, after the photoemission process, electrons go through the electrostatic lens array, tasked in this case with the retardation of the electrons before they enter the analyzer. Reduction of the kinetic energy is achieved by selecting a specific pass energy E_p . The pass energy is defined as the kinetic energy at the center of the measured energy band when the electron travels through the hemispheres of the analyzer. For the EW4000 hemispheric analyzer the pass energy ranges from 10 eV to 500 eV.

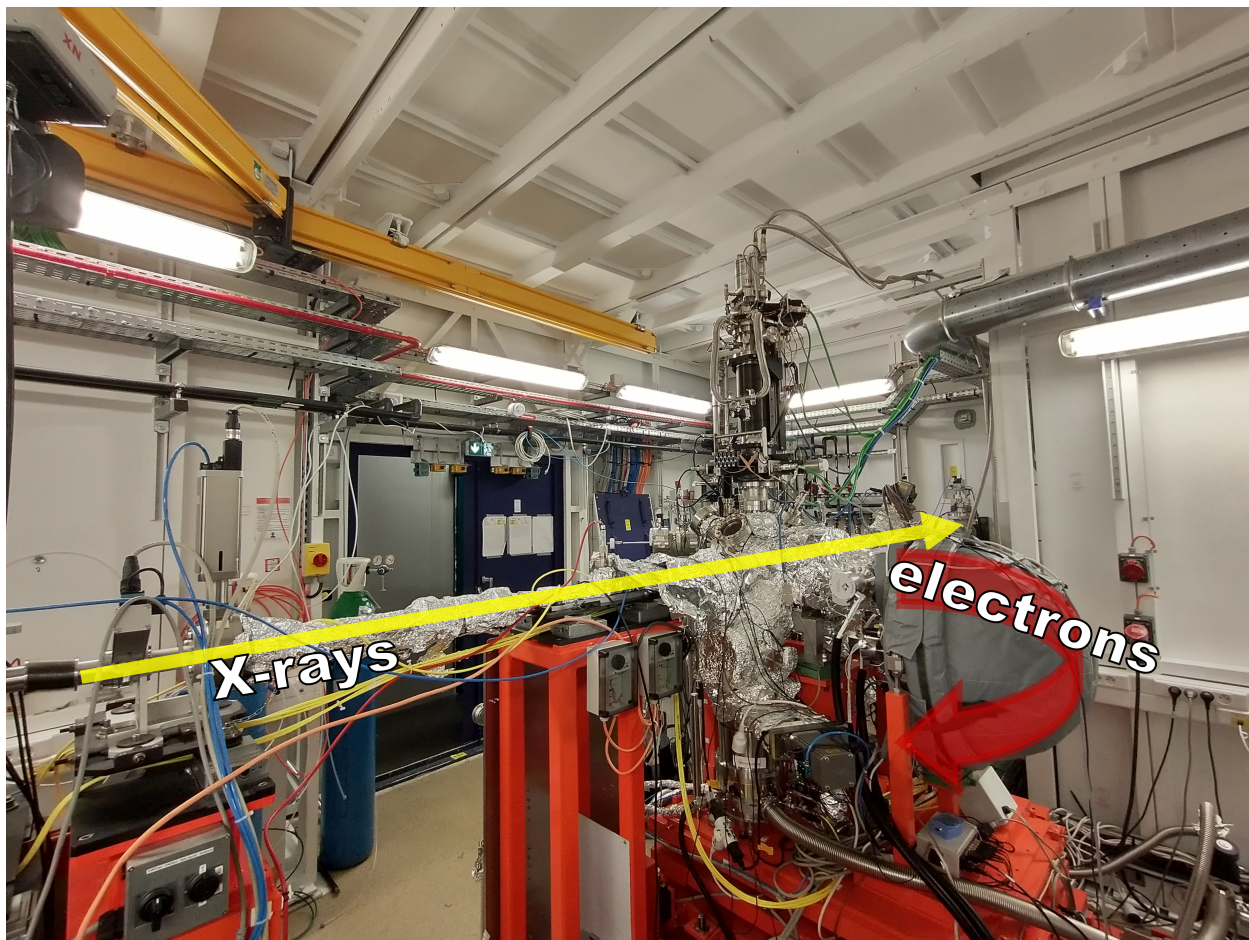


Figure 2.5: HAXPES end-station at the GALAXIES beamline. X-rays coming traversing through the optics hutch, interact with the sample, emitting electrons which are collected and analyzed with a hemispherical electron analyzer.

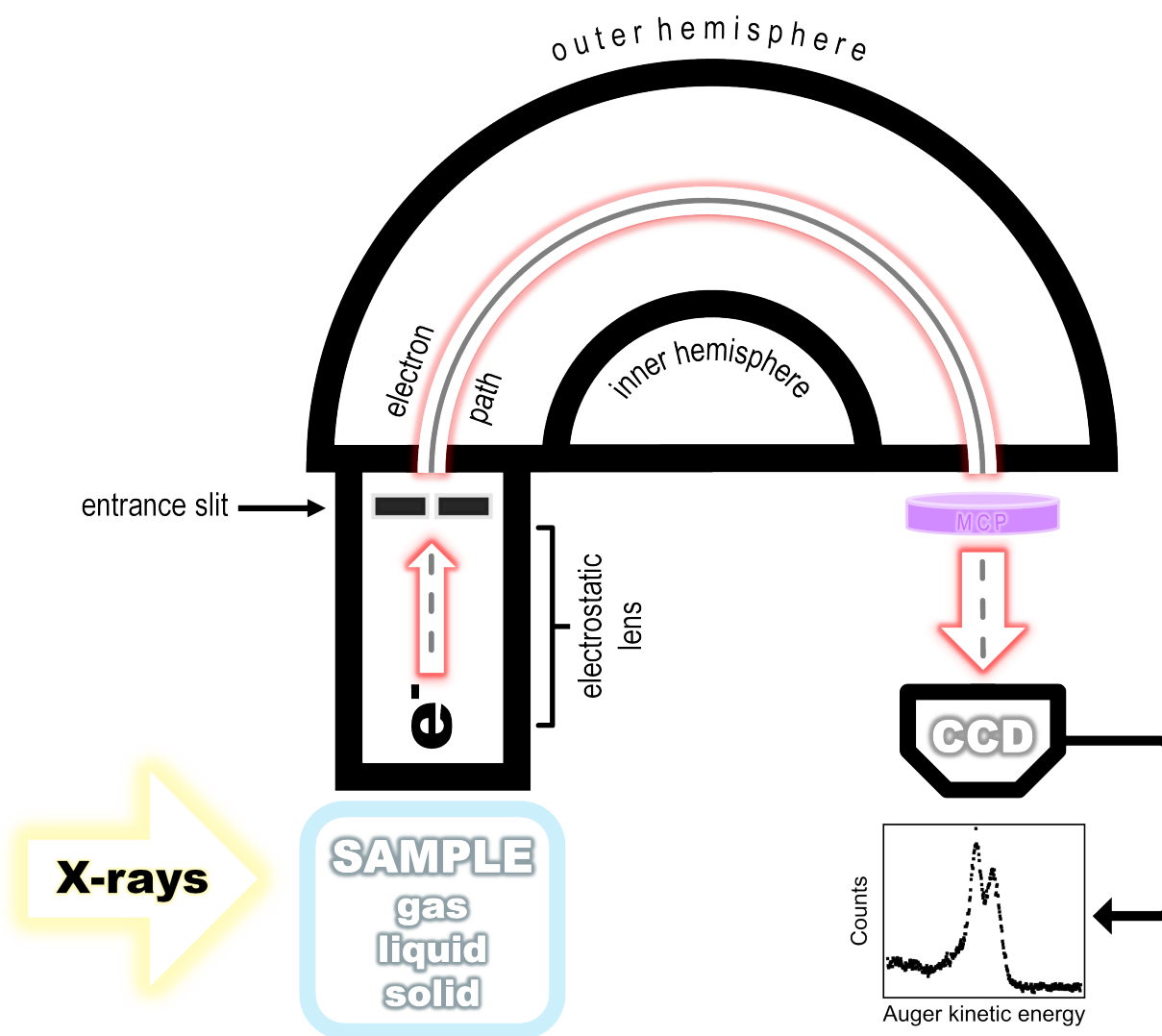


Figure 2.6: Schematic diagram of the VG SCIENTA EW-4000 hemispherical electron analyzer installed at the HAXPES end-station at the GALAXIES beamline. After the sample interacts with the incident light, electrons are emitted and collected by the analyzer.

After the electrons are directed through the lens and entrance slit, they enter the analyzer, in which energy dispersion and consequently recording of the electron kinetic energy takes place. The analyzer consists of two concentric hemispheres, as shown in the schematic diagram in Fig. 2.6, the outer, which is negatively charged, and the inner hemisphere, which has a positive charge. The path taken by the electrons is bent in an electrostatic field of 180° between the hemispheres, with a pass energy determined by the electrostatic field between the latter. The bending radius is determined by the initial kinetic energies of the photoemitted electrons, and will in turn result in an electron kinetic energy distribution as they impinge on the detector. However, before the electrons reach their final destination, they collide onto a micro-channel plate (MCP), consisting of a multitude of electron multipliers placed in parallel fashion with respect to one another, and whose task is to magnify the initial signal by emission of secondary electrons [71]. The ensuing cascade reaches a phosphor screen, and the by now, vastly enhanced signal reaches a charged-coupled device (CCD) camera, giving a 2D image of the electron distribution. Every flash originating from an electron is thus recorded by the CCD, where the position on the latter carries information on the spatial and energetic origin of the electron. The obtained spectrum (an example of which is shown in Fig. 2.6, bottom right, corresponding to *S KLL* Auger) will have a kinetic energy resolution determined by the entrance slit aperture size (and shape), and the pass energy E_p , as shown in Eq. 2.7,

$$\delta E \approx \frac{s \times E_p}{2r}, \quad (2.7)$$

where, s is the slit width, and r is the mean radius of the analyzer. As a general approximation, the highest resolution is obtained with low pass energy and smaller slit apertures. Such a configuration leads to lower count rates, and ultimately experimental settings are such that there is a compromise between adequate resolution and a viable number of counts.

Gas phase experiments

For experiments at the HAXPES end-station involving dilute species such as gaseous samples, a gas cell is in place, propped on a 4-axes manipulator at the bottom part of the main chamber. A differential pumping system is also in place which maintains ultra-high vacuum in the beamline as gas flows through the cell [69].

Solid state experiments

For solid state studies, there is in place a motorized copper sample-stage situated on the upper part of the chamber. The stage can house two sample plates. Unlike XAS measurements in the gas phase, which can only be performed in partial electron yield mode, here, they can be done with a picometer, and photon yield using a Si diode, in addition to partial electron yield mode. Preparation of the sample is carried out in a satellite UHV chamber, attached to the main compartment. Fig. 2.7, shows another view of the HAXPES end-station, displaying the preparation chamber in which solid samples are introduced, prior to a measurement.

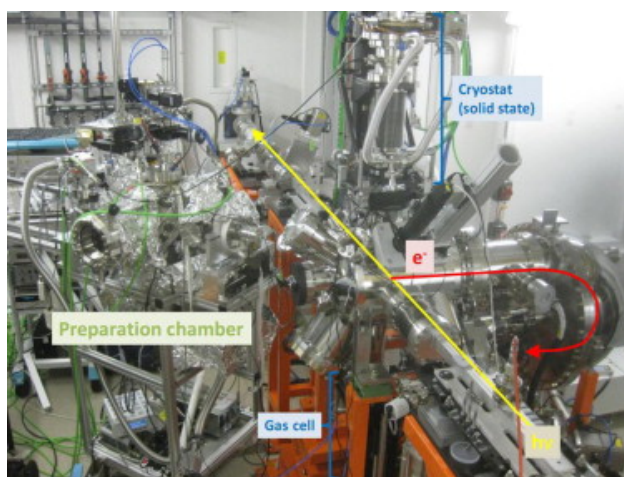


Figure 2.7: HAXPES end-station with preparation chamber, gas cell and cryostat in sight.

Liquid jet experiments

The liquid jet setup is not permanently installed at the end-station. Moreover, liquid-phase experiments, however rewarding, are quite challenging, which is why the description of the setup is somewhat more elaborate than the previous two.

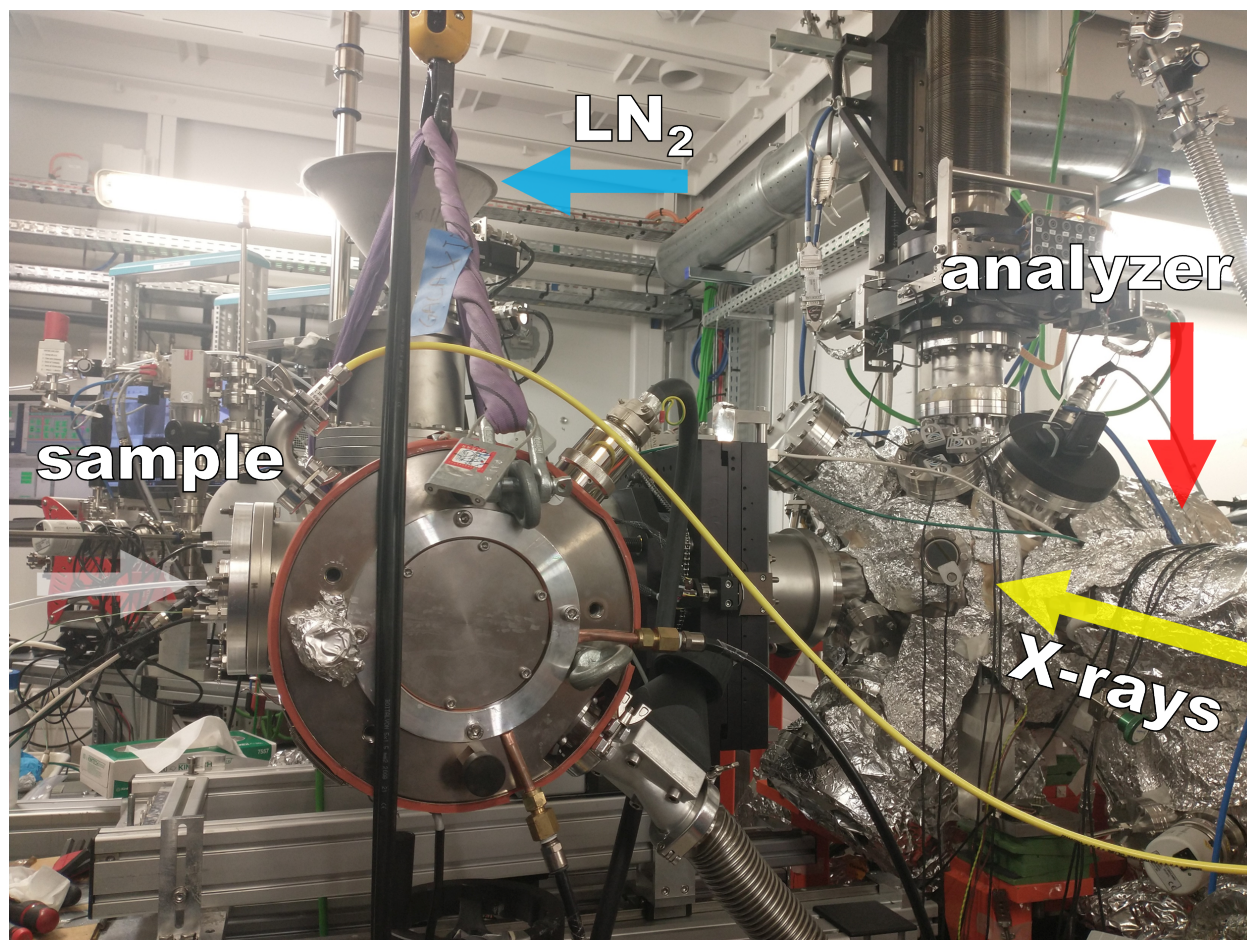


Figure 2.8: Liquid jet set up located on the HAXPES end-station. The sample is introduced to the main chamber using a HPLC pump containing the sample. A hose, carrying the solution stemming from the pump enters the chamber through the left-most flange, as indicated by the white arrow.

The liquid jet setup (developed in conjunction with Microliquids [72]), as visualized in Fig. 2.8 (used in my thesis for the studies on solvated cysteine), is mounted on the main chamber, connected to a flange opposite to the analyzer. The sample is connected to an HPLC pump (not shown in the figure), which is in turn connected to the main chamber

via a differentially pumped insert with two openings allowing for entrance of the photon and exit of the electron. A liquid nitrogen cold trap helps maintain a pressure of $\sim 10^{-5}$ mbar within the insert.

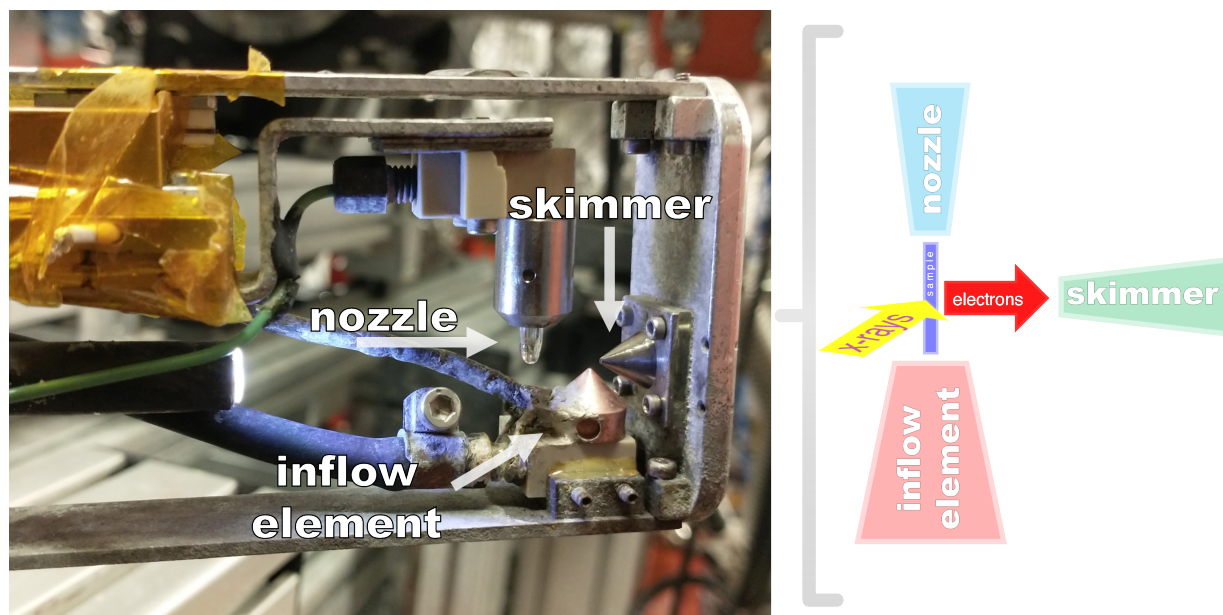


Figure 2.9: Liquid jet arm picture on the left, featuring the main constituents: nozzle, inflow element, and skimmer. On the right, a schematic of the geometry after alignment: photoemitted electrons ejected after impingement of x-ray photons on the jet (in blue) enter through the skimmer and towards the electron spectrometer.

The insert, which couples through the left-most flange, houses an arm in which a set of hoses carry the sample to the main chamber and remove the waste. At the end of the arm are located a nozzle, a skimmer, and an inflow element or catcher, as shown in Fig. 2.9. The sample flows through the nozzle, consisting of a glass capillary ($\text{\O} 20 \mu\text{m}$), where the jet is intersected by the incident x-rays, ensued by photoemission. The resulting electrons travel towards the spectrometer through the skimmer (and the insert opening). The waste is collected on the catcher ($\text{\O} 300 \mu\text{m}$). As the experiment takes place in vacuum, and in order to avoid frozen sample deposits, the catcher is heated up to $\sim 120 \text{ }^\circ\text{C}$. For a more encompassing review of the liquid jet and overall capabilities of the HAXPES end-station the reader is referred to [73].

Why HAXPES?

All experimental results presented in this thesis were possible due to HAXPES. By using hard X-rays, we can induce processes which result in the emission of high kinetic energy electrons. One key feature of HAXPES is its bulk sensitivity, allowing for significant minimization of surface effects [74]. Furthermore, at incident photon energies in the hard X-ray regime it is possible to explore phenomena such as nuclear dynamics, recoil effects, interference effects, double core-hole spectroscopy (DCH), cascade Auger events, photoelectron recapture and PCI effects [75]. Simon et al., showed how residual Ne ions experience recoil in the opposite direction and show a velocity dependence on the high kinetic energy of the photoemitted electrons due to momentum conservation [76]. Electronic-state lifetime interference effects in Ar were probed by Céolin et al. In the study, through the use of hard X-rays, deep core-shells can be accessed resulting in a coherent excitation of a manifold intermediate states ($1s \rightarrow np$ or $1s \rightarrow \text{continuum}$). The coherent excitation process, in turn, results in interference in the decay events to the same final states [77].

Still in Ar, in a PCI study by Guillemin et al., [11], it was shown how the line-shape distortion and blueshift of the Auger lines is strongest when the incident photon energy is just above the $1s$ ionization potential threshold. In addition, the probability of photoelectron recapture to high-lying Rydberg states was elucidated close to the ionization potential threshold. This is made possible by the high kinetic energy of the Auger electrons combined with the short lifetime of the Ar $1s$ vacancy of ~ 1 fs [47].

Regarding DCH, one of its more appealing features is its higher sensitivity to chemical environment as compared to traditional PES [78]. Püttner et al., demonstrated that in Ar, electron correlation processes can be accessed through photoelectron spectroscopy using HAXPES [79]. The HAXPES technique also enables dynamical processes to be probed with DCH, as demonstrated by Marchenko et al., [80]. In the combined experimental-theoretical study, spectral features in the hyper-satellite (HS) Auger spectrum revealed the presence of ultrafast proton motion in gas-phase water molecules, oc-

curing within the lifetime of the DCH states of the molecule. HS Auger spectroscopy as enabled by HAXPES, has the advantage that it is applicable at any incident photon energies which exceed the double-core IP. With hard X-rays, it is also possible to excite deep core-shells of atoms which are relevant to molecular systems, e.g. Cl $1s$ and I $2p$. Indeed, combining hard X-rays with the CHCS method, allows probing of ultrafast dynamics taking place in resonantly excited molecules on the same timescales as the core-hole lifetime, as demonstrated by Marchenko et al. [21]. In the study, it was possible to reconstruct the potential energy surface and extract the lifetime of the I $3d^{-2}$ DCH state in the CH_3I molecule upon core-excitation with hard X-ray synchrotron radiation.

In studies in the liquid phase and solid state, such as the ones presented in this thesis, HAXPES will therefore allow us to directly probe the bulk of our samples. The site- and element-specificity provided by hard X-rays and high kinetic energy electrons make HAXPES the ideal tool to explore both PCI and charge transfer in condensed matter.

2.3 Data analysis and treatment

After acquisition of a spectrum, it is necessary to correct for both the electron kinetic energies and photon energies. The electron energies recorded by the analyzer can be calibrated by recording a well-characterized Auger spectrum. In the approach presented here, the procedure entails measuring Ar $L_{2,3}M_{2,3}M_{2,3}$ Auger lines, as shown in Fig. 2.10. Subsequently, the calibrated incident photon energy can be determined by measuring a well-defined photoelectron spectrum, an example of which are Ar $2p$ photolines, as shown in Fig. 2.11. Unless otherwise stated in this thesis, all fitting procedures were executed using the SPANCF macro suite [81] for Igor Pro. This approach is valid for gas phase experiments only.

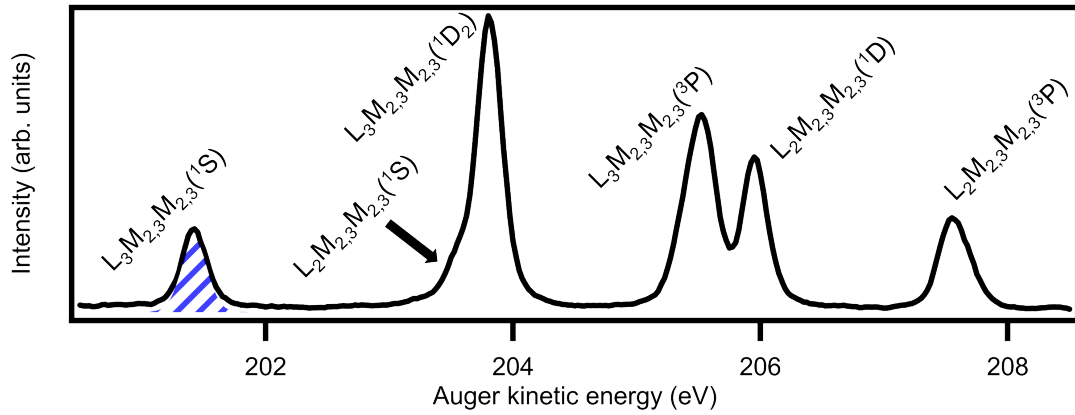


Figure 2.10: Auger spectrum of Ar $L_{2,3}M_{2,3}M_{2,3}$, recorded at incident photon energy $\hbar\omega = 2700$ eV. Black line corresponds to experimental data. Blue striped area under the first peak $L_3M_{2,3}M_{2,3}(^1S)$ obtained from a fitting procedure using a Voigt lineshape.

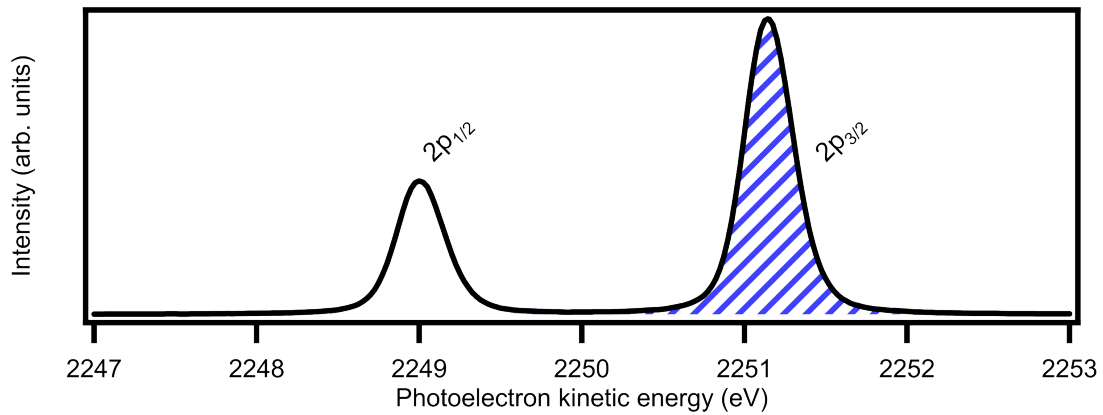


Figure 2.11: Ar $2p^{-1}$ photoelectron lines, recorded at incident photon energy $\hbar\omega = 2500$ eV. Black line corresponds to experimental data. Blue striped area under the $2p_{3/2}$ peak obtained from a fitting procedure using a Voigt lineshape.

2.3.1 Energy calibration

In Fig. 2.10 is presented the Ar $L_{2,3}M_{2,3}M_{2,3}$ Auger spectrum, measured at an incident photon energy $\hbar\omega = 2700$ eV. To calibrate the kinetic energy scale, the measured Auger spectrum should be measured with the same setup parameters as those of the experiment, namely the pass energy E_p and the slit width. The kinetic energy scale can be calibrated accordingly by using the experimental kinetic energy (E_{kin}^{exp}) of the well-isolated Ar

$L_3M_{2,3}M_{2,3}(^1S)$ peak (blue striped area) and a reference kinetic energy E_{kin}^{ref} . The latter is estimated as follows:

$$E_{kin}^{ref} = E_b^{ref} - Ar^+ - Ar^{2+} - E(Ar^{III}), \quad (2.8)$$

where E_b^{ref} is the binding energy of the L_3 electron in Ar, corresponding to 248.63(1) eV [82], Ar^+ , Ar^{2+} are the ionization energies of the mono- and di-cationic states in Ar, corresponding to 15.76 eV and 27.63 eV [83], respectively. Lastly $E(Ar^{III})$ is the energy level of the 1S term, corresponding to 4.12 eV [84]. The reference kinetic energy of the Ar $L_3M_{2,3}M_{2,3}(^1S)$ peak, therefore, amounts to $E_{kin}^{ref} = 201.12(1)$ eV. E_{kin}^{exp} is obtained via a routine fitting procedure, and subtracting the latter from E_{kin}^{ref} , will ultimately produce the kinetic energy offset ($\Delta E_{kin}^{cal} = E_{kin}^{ref} - E_{kin}^{exp}$) needed for calibration of the electron lines.

Calibration of the incident photon energy is hence straightforward, and following fitting of the Ar $2p^{-1}$ photoelectron lines, as shown in Fig. 2.11, the procedure is as follows:

$$E_b^{exp} = \hbar\omega^{exp} - (E_{kin(PE)} + \Delta E_{kin}^{cal}), \quad (2.9)$$

$$\hbar\omega^{cal} = \hbar\omega^{exp} + (E_b^{ref} - E_b^{exp}), \quad (2.10)$$

where E_b^{exp} is the experimental binding energy of an Ar $2p$ electron (Ar $2p_{3/2}^{-1}$ in the procedure described herein), $\hbar\omega^{exp}$ is the incident photon energy before calibration, $E_{kin(PE)}$ is the recorded kinetic energy of the photoelectron. The calibrated incident photon energy $\hbar\omega^{cal}$ is obtained by addition of the offset resulting from the term in parentheses as shown in Eq. 2.10.

2.3.2 Resolution

The total resolution pertaining a measurement arises from line broadenings originating from the electron analyzer ($\varphi_{analyzer}$), photon bandwidth ($\varphi_{\hbar\omega}$), and thermal broadening originating from the Doppler effect ($\varphi_{D(T)}$) [85]. The total resolution (φ_{total}) in this ap-

proach, will thus correspond to the Gaussian component of a well-defined photoelectron line, and is given by:

$$\varphi_{\text{total}}^2 = \varphi_{\text{analyzer}}^2 + \varphi_{\hbar\omega}^2 + \varphi_{\text{D(T)}}^2. \quad (2.11)$$

The contribution corresponding to thermal Doppler broadening is determined as follows [85]:

$$\varphi_{\text{D(T)}} = 0.723 \left(\frac{ET}{M} \right)^{\frac{1}{2}} \text{ meV}, \quad (2.12)$$

where E is the kinetic energy of the electron (eV), T is the temperature (K), and M is the mass of the studied atom or molecule (atomic mass units).

To determine $\varphi_{\text{analyzer}}$, we utilize the Ar $L_{2,3}M_{2,3}M_{2,3}$ Auger spectrum. Given a well-defined and well-isolated peak, it is possible to extract the lineshape components of the latter. Auger peaks can be described by a Voigt lineshape, corresponding to a convolution of a Gaussian and Lorentzian distribution function. The FWHM of the latter is in our case indicative of the lifetime (Γ) of an L^{-1} state, in which a $2p$ electron has been ejected. For an Ar $2p_{3/2}$ electron in the gas phase, $\Gamma_{L_3^{-1}} = 128$ meV [47]. The Gaussian FWHM, in turn, will account for experimental line broadening contributions. Since the spectral properties of electrons emitted as a result of normal Auger decay do not depend on the bandwidth of the incoming light, we can use this information to obtain the analyzer broadening contribution. Upon fitting our target peak, $L_3M_{2,3}M_{2,3}(^1S)$, as shown in Fig. 2.10, the FWHM of the Gaussian distribution will contain $\varphi_{\text{analyzer}}$:

$$FWHM(G)^2 = \varphi_{\text{analyzer}}^2 + \varphi_{\text{D(T)}}^2 + \varphi_{\text{D(Auger)}}^2, \quad (2.13)$$

where $\varphi_{\text{D(Auger)}}$ corresponds to the Doppler shift due to ion recoil upon ejection of a photoelectron, and which is manifested in Auger spectra. $\varphi_{\text{D(Auger)}}$ can be quantified as

follows [76]:

$$\varphi_{D(\text{Auger})} = m_e \cdot |\vec{v}_{\text{Auger}}| |\vec{v}_{\text{nucleus}}| = \frac{\sqrt{E_{\text{kin(Auger)}} \times E_{\text{kin(eff)}}}}{918 \times M}, \quad (2.14)$$

$$E_{\text{kin(eff)}} = E_{\text{kin(PE)}} \left(1 + \frac{E_{\text{kin(PE)}}}{2m_e c^2} \right), \quad (2.15)$$

where \vec{v}_{Auger} and \vec{v}_{nucleus} are the velocities of the Auger electron and nucleus, respectively. m_e is the mass of the electron, $E_{\text{kin(Auger)}}$ is the kinetic energy of the Auger electron, M is the atomic or molecular mass of the studied system as above. $E_{\text{kin(eff)}}$ is the kinetic energy of the photoelectron ($E_{\text{kin(PE)}}$) corrected for relativistic effects. The denominator in Eq. 2.15, containing twice the m_e and the squared speed c of light amounts to 1.022 MeV.

Lastly, to estimate the photon bandwidth broadening $\varphi_{\hbar\omega}$, we make use of Eq. 2.11. Assuming $\Gamma = 128$ meV as the FWHM of the Lorentzian distribution, φ_{total} will consequently correspond to the FWHM of the Gaussian distribution, which is obtained after fitting an Ar $2p^{-1}$ photoelectron spectrum, as exemplified in Fig. 2.11.

As an in-house developed procedure, caution must be exercised with the choice of spectra, where an exceedingly large number of counts may result in lineshape distortion, producing skewed results. Another more subtle caveat is the choice of system upon which to base the calibration and resolution estimation procedures, where involvement of a non-negligible $2p^{-2}$ final state lifetime may introduce a new source of broadening contained in the FWHM of the Lorentzian distribution.

2.3.3 Energy referencing in condensed matter systems

In the case of gas-phase experiments, the kinetic energy of the detected electron is inherently measured with relation to the vacuum level far from the probed system (VL^∞) [86], and it is given by the Einstein relation described in Eq. 2.16.

$$E_{\text{kin}} = \hbar\omega - E_b. \quad (2.16)$$

However, when performing measurements in condensed matter samples, VL^∞ is not applicable. Instead, it is appropriate to consider the VL just outside the sample [87,88]. Additionally, in electron spectroscopy of condensed matter systems, it is preferable to reference the kinetic energy of the electron with respect to the Fermi level (FL). Consequently, the energy difference between this local VL and the FL corresponds to the work function Φ . The work function is defined as the minimum energy needed to remove an electron, located at the FL, from a given material into the VL just outside the sample [87–90].

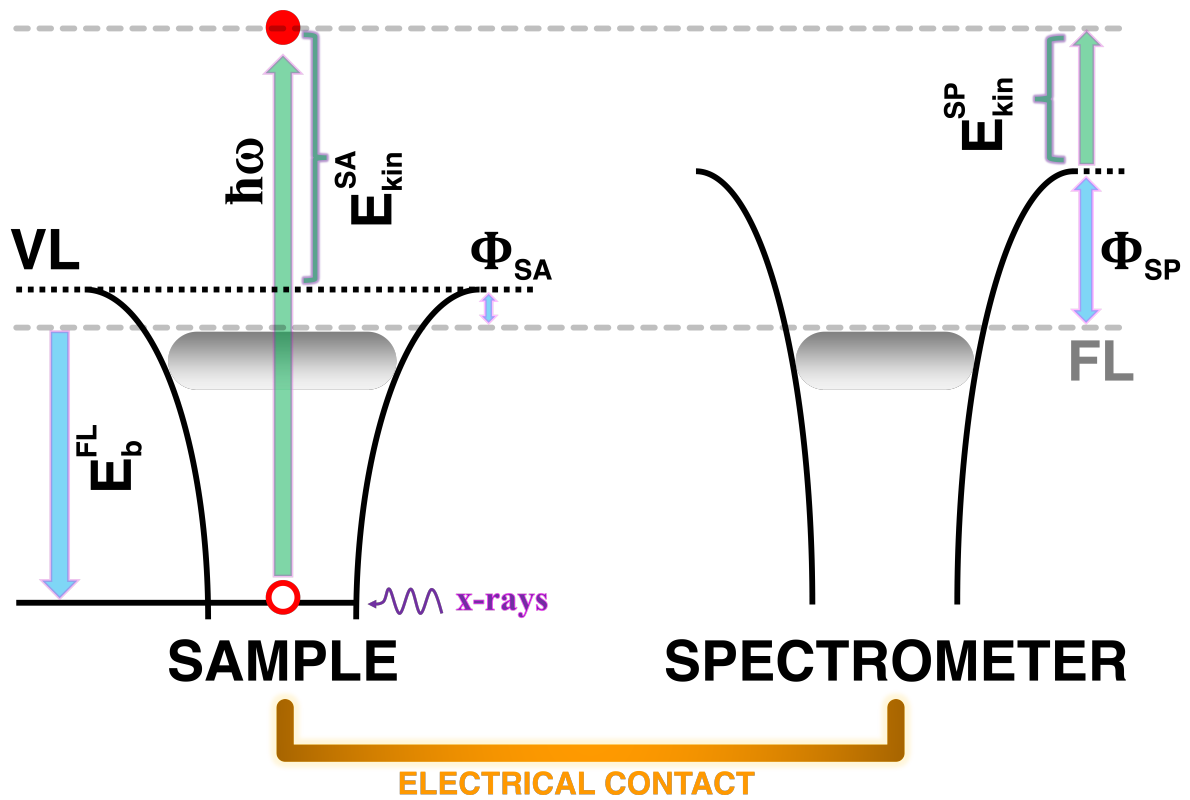


Figure 2.12: Energy level diagram scheme for a solid sample in a photoemission experiment with good electrical contact between sample and grounded electron analyzer. FL: Fermi level. VL: vacuum level just outside the sample. Φ_{SP} : spectrometer work function. Φ_{SA} : sample work function. $E_{\text{kin}}^{\text{SA}}$: electron kinetic energy referenced to VL. $E_{\text{kin}}^{\text{SP}}$: electron kinetic energy measured by spectrometer. Adapted from [91] p. 44.

As described in Fig. 2.12, the impinging x-ray photon will eject a photoelectron (or an Auger electron is emitted as a result of photoionization) which must first overcome the binding energy with respect to FL (E_b^{FL}) and then the sample work function Φ_{SA} before being ejected from the sample. The kinetic energy of the electron (E_{kin}^{SA}) will thus be given by Eq. 2.17.

$$E_{kin}^{SA} = \hbar\omega - E_b^{FL} - \Phi_{SA}. \quad (2.17)$$

In order to avoid the space-charge effect in photoemission experiments involving solid or liquid samples, there must good electrical contact between sample and spectrometer [86]. The latter results in an alignment of the FL of both sample and spectrometer, as depicted in the energy level diagram presented in Fig. 2.12. The alignment originates from transfer of electrons from the sample to the spectrometer if the sample work function is smaller than the spectrometer work function $\Phi_{SA} < \Phi_{SP}$, and vice versa if $\Phi_{SP} < \Phi_{SA}$. In the case of good electrical contact, and a subsequent alignment of sample and spectrometer FL, the electron kinetic energy measured by spectrometer (E_{kin}^{SP}), will be given by Eq. 2.18 [86].

$$E_{kin}^{SP} = \hbar\omega - E_b^{FL} - \Phi_{SP}. \quad (2.18)$$

As further described in Fig. 2.12, the potential barrier "experienced" by the detected electron will ultimately correspond to the spectrometer work function (Φ_{SP}). This is crucial for photoemission experiments, as Φ_{SP} is constant, and binding energies will be directly given by the kinetic energy as recorded by the spectrometer (E_{kin}^{SP}) and the incident photon energy. Φ_{SP} can be determined in a straightforward fashion by measuring the spectrum of a reference sample, such as the photoelectron spectrum of Au $4f_{7/2}$. In our calibration procedures using the above-mentioned photoline, $\Phi_{SP} = 4.90(1)$ eV.

$$E_{\text{kin}}^{\text{cal}} = E_{\text{kin}}^{\text{SP}} + \Phi_{\text{SP}}. \quad (2.19)$$

In the next chapter, the Auger electron kinetic energies ($E_{\text{kin}}^{\text{cal}}$) are presented with respect to the FL and are therefore blueshifted by $\Phi_{\text{SP}} = 4.90(1)$ eV to account for the spectrometer work function, as indicated in Eq. 2.19.

The aforementioned approach is valid with a small caveat, in that the samples involved are assumed to be non-insulators. For insulators, the FL is poorly defined. The studied solid samples which will be presented in the next section are indeed semiconductor polymers. Concerning liquid-phase experiments, where deionized water, an insulator, was used to prepare the different studied solutions, it becomes a semiconductor upon addition of electrolytes.

2.4 Systems studied

As broached in the introductory chapter, the systems under investigation considered in this work consist of sulfur-containing samples ranging from the gas phase, to liquid phase, and the solid state. Broadly and generally speaking, the systems investigated have applications which are relevant to chemistry and life sciences, as well as organic electronics and solar energy harvesting and industrial applications [92]. Below is given a description of the sample preparation procedures, most of which will be recounted in a more concise manner in the following chapters.

2.4.1 Gas phase: thiophene

Gaseous thiophene, whose schematic structure is shown in Fig. 2.13, was used for the study concerning post-collision interaction effects in thiophene and solid-state thiophenic polymers.

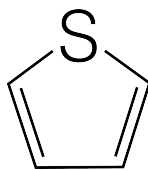


Figure 2.13: Schematic structure of thiophene.

To measure thiophene in the gas phase using the HAXPES set up, liquid thiophene was placed in a test tube and connected to the gas manifold inlet, as shown in Fig. 2.14, followed by a freeze-thaw-pump cycle for degassing. The vapor generated in the head-space was then gently introduced into the gas cell through a micro-leak valve, keeping a constant pressure of $\sim 10^{-5}$ mbar inside the experimental chamber. This pressure was sufficiently low for the molecules in the gas cell to be considered as isolated.

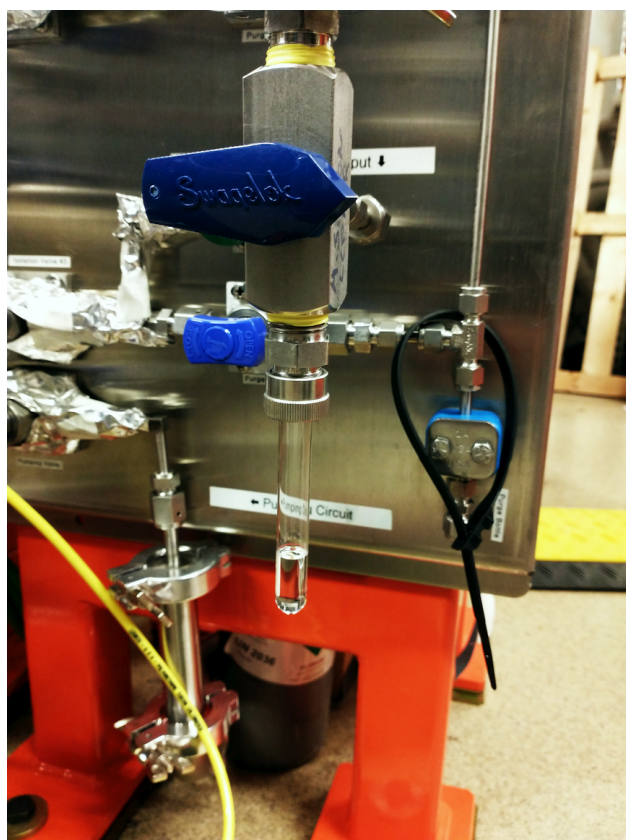


Figure 2.14: Container with liquid thiophene connected to the gas inlet leading to experimental chamber.

2.4.2 Liquid phase: L-cysteine

Experiments in liquid phase were carried out using the amino acid L-cysteine (structure shown in Fig. 2.15) in crystalline powder form dissolved in deionized water. The L-cysteine solution was measured at five different pH values: 1, 5, 9, 12.

Cysteine powder was poured in a container with deionized water and stirred until it was fully dissolved, upon which it was filtered to remove impurities. The pH was adjusted and monitored constantly by adding aqueous HCl or a concentrated solution of NaOH to the solution of L-cysteine in water, maintaining a final concentration of ~ 0.5 M. While higher concentrations would have been preferred, it posed a risk as the extreme pH solutions could have damaged the pump mechanism and jet.

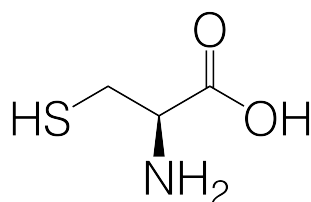


Figure 2.15: Schematic structure of L-cysteine.

2.4.3 Solid state: polymers

Charge transfer and PCI studies both involved solid state polymeric samples. The π -conjugated polymers polythiophene, and poly(3-hexylthiophene-2,5-diyl), or P3HT, whose schematic structures are presented in Fig. 2.16.

Polythiophene suffers from poor electric conductivity, and thus it was necessary to mix it with graphite powder to tackle space-charge buildup. The latter may shift and distort energy distribution of measured electrons [93]. Thus, pure polythiophene powder was mixed in approximately equal mounts with graphite powder, and finely ground until a homogeneous looking blend was obtained. The blend was then sprinkled on carbon tape, which was fixed on the sample holder. After covering the entire surface, additional

carbon tape was placed on the edges of the blend, ensuring a proper electrical connection between the sample surface and the stainless steel sample holder. The resulting powder blend is shown in Fig. 2.17.

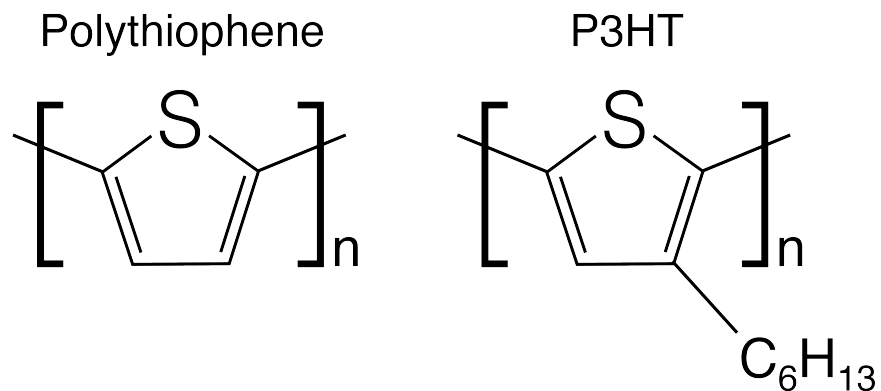


Figure 2.16: Schematic structure of polythiophene and P3HT.

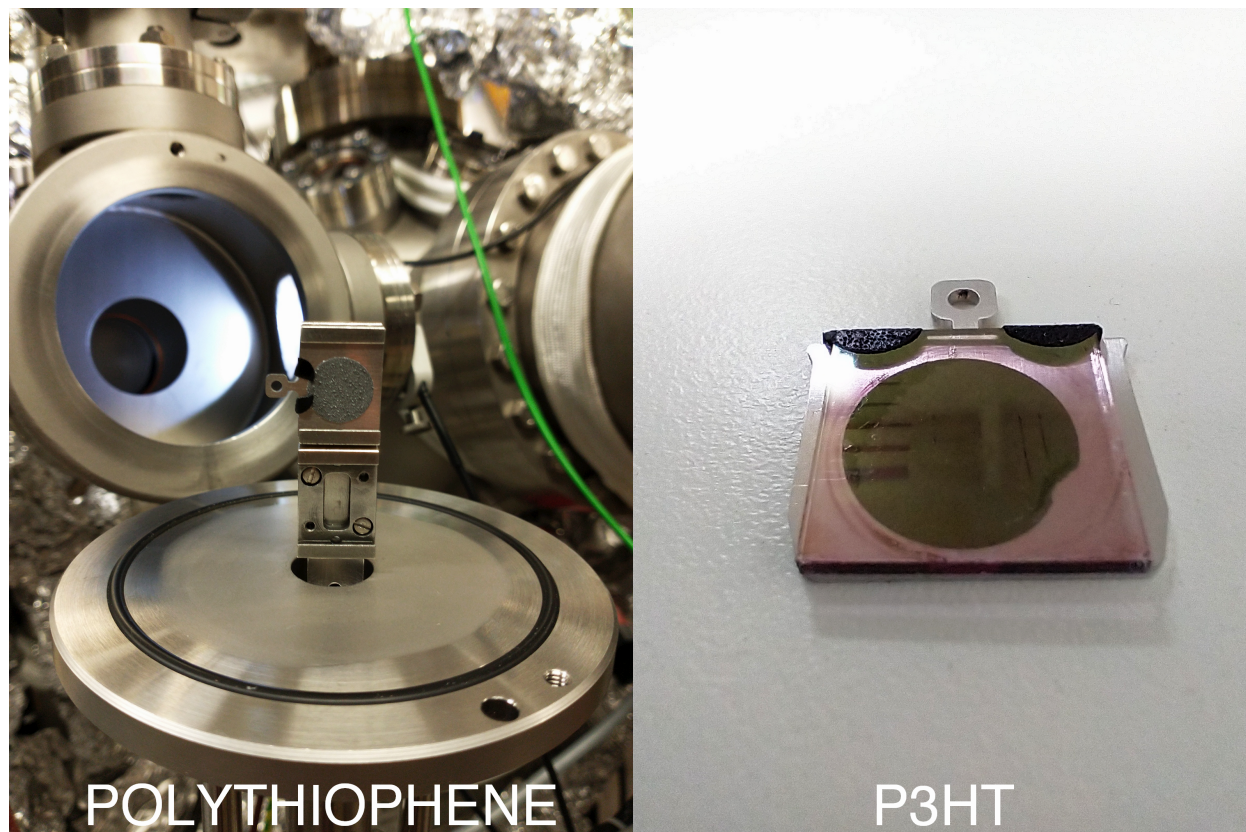


Figure 2.17: Polymer samples as prepared before measurements. Polythiophene in powder form. P3HT prepared as a thin-film.

P3HT was prepared by Laure FILLAUD, from the Laboratoire Interfaces et Systèmes Electrochimiques at Sorbonne Université. It was dissolved in chloroform to a concentration of 5 mg/mL and subsequently spin-coated onto an indium-tin-oxide (ITO) substrate at ~ 2000 RPM. The resulting film was placed on a stainless steel sample holder and affixed with carbon tape, which, once more, served as an electrical conductor. The thin-film is presented in Fig. 2.17. Also visible on the surface of the latter are lines resulting from the impingement of the X-rays on the sample. To ensure that the sample was not being damaged during the experiment it was vertically moved between each scan. This rastering motion was used with both polymers.

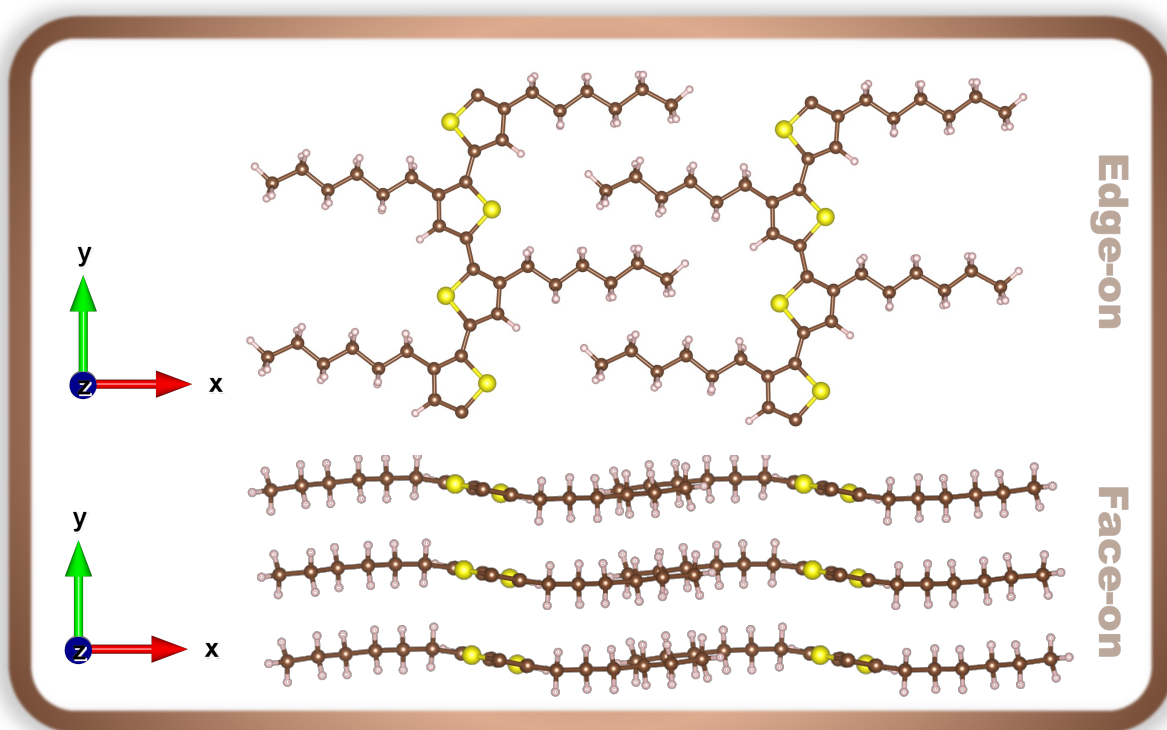


Figure 2.18: P3HT thin-film in edge-on and face-on orientations. X(Y)-axis parallel (perpendicular) to the sample surface. Sample surface fixed on the ZX plane.

Depending on the procedure used to prepare the P3HT thin-film, as indicated by Fig. 2.18, there are two potential orientations of the polymer chains on the substrate [94]. In the edge-on orientation, the self-organized lamellae are positioned perpendicular to

the substrate, while in the face-on orientation, the lamellae are fixed parallel to the substrate. The resulting ~ 34 nm thin-film was not thermally treated and was used as-is. The combination of the rotational spin-coating frequency and the chloroform solution concentration lead to the formation of a face-on orientation [95]. Furthermore, X-ray diffraction analysis of the thin-film, using a Cu $K\alpha$ source in a symmetric $\theta/2\theta$ geometry, revealed a signature at 24° corresponding to the inter-chain $\pi - \pi$ stacking, which hints at a face-on orientation of the film [96, 97]. Additionally, no sharp structures typical for an edge-on orientation were observed.

Chapter 3

Post-collision interaction: from gas phase to solid state

3.1 Introduction

The ionization of atomic inner shells leads to the creation of intermediate excited states and their subsequent relaxation via emission of electrons and x-ray photons. The Coulomb interaction between the emitted electrons and the remaining ion noticeably distorts the electron spectra, and this phenomenon is known as post-collision interaction (PCI) effect. The PCI effect has been thoroughly explored for decades in gas phase atoms [4, 5] and molecules [6–8, 10]. Fewer studies have been performed on PCI in condensed media [98–103].

Meanwhile, understanding the mechanism of PCI and its manifestation in solids is of significant practical interest. Methods such as X-ray photoelectron spectroscopy and Auger electron spectroscopy are widely used in material science for analysis of surfaces and interfaces of a vast range of materials. The accuracy of these methods strongly relies on the careful description and interpretation of the shape and energy position of the spectral lines, which can be significantly affected by the PCI effect. Aiming at the development of a generalized description of the PCI effect in a variety of media, we have performed a comparative study in gas phase thiophene and in solid thiophene-based polymers.

The first observation of the PCI effect was made in atoms bombarded by slow ions [104, 105]. In the following 20 years the PCI effect was studied in a process of electron-impact excitation of the atomic autoionizing states or in the photoionization of the atomic inner shells followed by the Auger decay. In the latter case ionization is described by the following two-step process. In the first step, photoabsorption yields a photoelectron and a meta-stable singly charged ion with an inner-shell vacancy, which in the next step undergoes relaxation through emission of an Auger electron leaving the ion doubly charged.

The PCI effect is reduced in this case to the Coulomb interaction between three charged particles: the emitted photoelectron, the Auger electron, and the remaining ionized atom. Their interaction results in energy exchange between the two emitted elec-

trons. Coulomb repulsion between the outgoing fast Auger electron and the slow photoelectron in the field of the residual ion accelerates the former and slows down the latter. In a classical picture, the closer the photoelectron to the ion at the moment of Auger decay, the larger the energy gain of the Auger electron and, consequently, the energy loss of the photoelectron. Thus, close to the ionization threshold, PCI leads to a substantial distortion and energy shift of both the Auger electron and the photoelectron spectral lines.

The PCI effect in isolated atoms has been extensively studied both theoretically and experimentally. On the theoretical side, a number of models describing PCI have been developed on the basis of classical [105, 106], semiclassical [107–110] and quantum mechanical [13, 111, 112] approaches. On the experimental side, several techniques have been developed, such as photoelectron-ion coincidence spectroscopy [9], Auger electron spectroscopy [11], multielectron-coincidence spectroscopy [113, 114], which allow addressing different aspects of the PCI effect [9, 11, 113, 115, 116].

The first investigations of the PCI effect in molecules made use of ion time-of-flight mass spectroscopy [6] and two-dimensional photoelectron spectroscopy [8]. Later, photoelectron-ion coincidence spectroscopy performed in the gas phase OCS molecule, revealed the hallmark PCI features and showed that the magnitude of the PCI shift depends on the number of electrons emitted during the Auger cascade [10]. In this study, the theoretical semiclassical approach, originally used for the atomic case, was successfully extended to the molecular case.

For larger and more complex systems, few examples are found in the literature concerning either experimental or theoretical studies [98–102]. These works revealed two competing mechanisms that affect the PCI in the condensed medium, namely, screening of the Coulomb interaction and electron scattering. While screening weakens the Coulomb interaction and, consequently, suppresses PCI, electron scattering reduces the distance that the photoelectron can travel from the ion in the condensed medium before the Auger decay occurs, and therefore, enhances PCI in comparison to the case of an

isolated atom.

A significant reduction of PCI was observed in metal as opposed to an insulator medium due to a stronger screening of the Coulomb interaction between the charged particles [98]. A suppression of the PCI effect in photoionization of atoms deposited on a metallic substrate was reported in Refs. [99, 100]. This observation was attributed to polarization screening of the Coulomb interaction between the charged particles near the metallic surface that was taken into account by the image charges. Furthermore, an investigation of the PCI effect in X-ray photoelectron spectra measured in isolated noble-gas atoms and atomic clusters, showed that the PCI effect in the bulk of a cluster is reduced compared to that of an atom [101]. These findings were also explained with the polarization screening of the bulk medium in the clusters.

The influence of electron scattering on PCI processes was theoretically studied for $L_3M_{4,5}M_{4,5}$ Auger spectrum in solid state copper [102]. Inelastic electron scattering which slows down photoelectron propagation was shown to amplify the PCI effect. Recently, an observation of the PCI effect in KLL Auger spectra of solvated K^+ and Cl^- ions in aqueous solution has been reported [103].

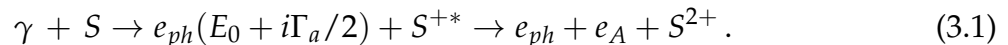
In this paper, we develop a general description of PCI in a condensed medium, thus extending the well-established quantum mechanical description of PCI for an isolated atom. Namely, we demonstrate the presence of the PCI effect in sulfur KLL Auger spectra measured for the gas phase thiophene and in solid state organic polymers: polythiophene (PT) and poly(3-hexylthiophene-2,5-diyl), commonly known as P3HT. The choice of these conjugated semiconducting polymers is motivated by their promising applications in optoelectronic devices and organic field-effect transistors [48, 117–119]. The advantage of using KLL Auger spectroscopy after S 1s ionization for PCI investigation is related to the short lifetime of the S 1s core hole and a well-defined high kinetic energy of the Auger electron resulting in a strong three-body interaction of the charged particles. The PCI effect is manifested as a distortion and a blueshift of the normal Auger

S *KLL* spectrum when S 1s ionization occurs close to the ionization threshold. Our investigation shows that the PCI-induced shift of the Auger spectra is stronger in the solid state polymers than in the gas phase organic molecule.

Our theoretical approach is based on the well-known eikonal approximation [13] which allows incorporating effects of both polarization screening and electron scattering. The model developed within the framework of the eikonal approximation provides a good agreement with the experimental observations. The performed analysis demonstrates that the PCI-based energy exchange between the photoelectron and the Auger electron in the polymer medium is qualitatively similar to the case of an isolated atom, although modified by photoelectron scattering and charge screening. We show that electron scattering in the polymer has a stronger effect on the PCI energy shift than the polarization screening, which effectively results in the enhancement of the PCI effect in the considered PT and P3HT polymers compared to the isolated thiophene molecule.

3.2 Theoretical description

The process of 1s shell photoionization of an isolated sulfur atom, followed by *KLL* Auger decay, can be represented by the following scheme



In the first step the incident photon γ ionizes the 1s shell of the sulfur atom leaving the residual ion S^{+*} in a metastable autoionizing state with the lifetime width of $\Gamma_a = 0.59$ eV [47]. Consequently, the emitted photoelectron e_{ph} in the intermediate state has the complex energy $E_0 + i\Gamma_a/2$, where $E_0 = E_\gamma - IP$ is the excess photon energy, E_γ is the incident photon energy and IP is the 1s shell ionization potential. Note that such a complexity of the particles' energy is usual for the description of two-step processes, which involve the creation and decay of metastable states (see, e.g. [4]).

In the second step, the intermediate autoionizing state of the S^{+*} ion with $1s^{-1}$ vacancy decays via KLL Auger transition to the doubly-charged sulfur ion S^{2+} with two vacancies in the $2p$ shell resulting in emission of the fast, 2.1 keV, Auger electron e_A . In the present study the excess photon energy E_0 ranges from nearly zero at the threshold up to ~ 210 eV. This means that the photoelectron energy $E_{ph} \simeq E_0$ is smaller than the Auger electron energy E_A by at least an order of magnitude. Hence, the Auger electron instantly leaves the interaction region at the moment of Auger decay and the photoelectron experiences a sudden change of the ion field from the potential of the singly- to doubly-charged sulfur ion. Consequently, the photoelectron loses part of its total energy due to the negative change of its potential energy. Note that this photoelectron energy loss is not accepted by the residual ion but transmitted to the outgoing Auger electron. The heavy ion does not participate in the energy exchange due to its large mass. Thus, the actual force responsible for PCI energy exchange is the Coulomb repulsion between the photoelectron and Auger electron in course of their recession in the field of the doubly charged ion. The outgoing Auger electron as a faster particle accelerates due to the Coulomb repulsion and gains additional energy while the photoelectron decelerates and loses its energy. This energy exchange distorts the respective energy spectra: red shifting the maximum of the photoelectron line and blue shifting by the same value ΔE the maximum of the Auger electron line.

The focus of the present paper is the PCI-induced energy shift. In the case of an isolated atom it has been well described within numerous theoretical approaches [4, 5]. For our study we chose the eikonal approximation [13] because it provides a closed analytical expression for the PCI energy shift (here and throughout the paper we use the CGS-Gaussian system of units):

$$\Delta E = \frac{\Gamma_a}{2\hbar} \left(\frac{e^2}{v_{ph}} - \frac{e^2}{|\mathbf{v}_A - \mathbf{v}_{ph}|} \right), \quad (3.2)$$

where v_{ph} is the photoelectron velocity and \mathbf{v}_{ph} and \mathbf{v}_A denote velocity vectors of the

photoelectron and the Auger electron, respectively. On the other hand, the approximation, which has been developed for the case of an isolated atom, can be extended to the case of an atom embedded in the bulk medium by taking into account both the effect of charge screening and the effect of electron scattering.

The only drawback of the approximation is its limited applicability close to the ionization threshold. Equation (3.2) can be applied if the PCI energy shift is much smaller than the photoelectron energy $\Delta E \ll E_{ph}$ [13] which, according to Eq. (3.2), means that $E_0 \gg \Gamma_a^{2/3} E_H^{1/3} / 2$ where $E_H = 27.2$ eV is the atomic unit of energy. Under this condition, the approximation provides a good agreement with experimental observations (see, e.g. [120]). The better this condition is fulfilled the higher is the accuracy provided by Eq. (3.2). For the ionization process considered in Eq.(3.1), in the case of an isolated sulfur atom, $\Gamma_a^{2/3} E_H^{1/3} / 2 \simeq 1$ eV. For the excess energy $E_0 = 10$ eV Eq. (2) gives the correct PCI energy with accuracy of 96%, whereas for $E_0 = 5$ eV and $E_0 = 1$ eV the accuracy is 90% and 67%, respectively. In the case of a sulfur atom embedded in the polymer, this condition must be adapted as discussed below.

Let us first consider the applicability of the eikonal approximation in the case of a molecule. According to Eq. (3.2), the PCI energy shift depends on the lifetime width and the electron velocities, i.e. on the excess photon energy, Auger transition energy and kinematics of the electron emission. In the particular case of the ionization process considered in Eq. (3.1), the Auger electron is much faster than the photoelectron. Therefore, the first term in the right-hand side of Eq. (3.2) is the leading one, while the second term with inverse relative velocity of the Auger electron and the photoelectron provides a small contribution. Hence, ΔE depends on two parameters: Γ_a and $v_{ph} = \sqrt{2E_{ph}/m} \simeq \sqrt{2E_0/m}$, where m is the electron mass.

In this case, Eq. (3.2) for the PCI energy shift has a simple classical interpretation. The negative PCI energy shift of the photoelectron spectrum, $-\Delta E$, equals to the sudden change of ionic potential $-e^2/r$ at the moment of the Auger decay, where r denotes

the photoelectron distance from the ion. It can be demonstrated [105] that the energy exchange between the two electrons occurs with the largest probability density at time delay $2\hbar/\Gamma_a$ after K-shell ionization when the photoelectron has moved from the ion at the distance $r = 2\hbar v_{ph}/\Gamma_a$. It leads exactly to a PCI energy shift $-\Delta E$ given by Eq. (3.2) at $v_{ph} \ll v_A$. Typically, the distance r , where the PCI energy exchange takes place, is much larger than the Bohr radius, $r \gg a_0 = \hbar^2/me^2$, because of small values of the lifetime width $\Gamma_a \ll E_H$. In our case even at the excess energy $E_0 = 1$ eV one obtains $r \simeq 25a_0$.

Therefore, in the molecular case, the PCI between the electrons resulting from the atomic inner-shell ionization, does not differ from the case of an isolated atom [10]. On the other hand we consider the S *KLL* Auger transition between the deep inner atomic shells. It means that the influence of the molecular environment on the widths and energies of the initial and final ionic states can be neglected. That is why we will use the Eq. (3.2) to describe the PCI energy shift of the Auger electrons emitted from the thiophene molecule.

However, in the case of ionization of a sulfur atom within the thiophene-based polymer, Eq. (3.2) should be modified. Polarization of the polymer weakens the Coulomb interaction between the residual sulfur ion, the photoelectron and the Auger electron. This effect can be taken into account by means of polymer dielectric permittivity ϵ . Namely, we will replace the squared electron charges e^2 by their screened values e^2/ϵ as in Ref. [101].

Generally, the permittivity ϵ depends on the frequency of the electric field. To properly account for the charge screening, the permittivity needs to be computed over a wide frequency range, which is beyond the scope of the present study. The relative permittivity values for P3HT and PT reported in literature fluctuate between ~ 3 – 7 depending on the measurement method and the sample environment [121–125]. In our experiment the permittivity can be strongly affected by such factors as heating of the sample by the X-ray beam, electric contact with the sample holder, P3HT film thickness and blending of polythiophene with the conductive graphite powder. Therefore, in our simulations

we use permittivity as a fitting parameter and obtain $\varepsilon = 6.5$ for both polymers, which is within the range of values provided in the literature.

Another effect that should be taken into account is electron scattering which affects electron propagation through the solid medium. On the one hand, the photoelectron may lose energy during inelastic scattering processes. On the other hand, elastic scattering strongly affects the electron trajectory. Such changes in the electron propagation direction effectively reduce the distance that the photoelectron travels in the solid by the time the Auger decay occurs, resulting in amplification of the PCI effect. The electron propagation through the bulk medium is a very well studied phenomenon. Regardless of the mechanism of electron scattering (intra-molecular scattering [126], electron-phonon collisions [127], scattering off structural imperfections of the medium [128], etc.), this process leads to attenuation of the electron beam intensity $I(x) = I_0 \exp(-x/L)$, where x is the electron path and L is the effective attenuation length (EAL).

It should be noted that even in the case of ionization of an isolated atom the photoelectron propagation is described by the damped wave function $|\psi(r)|^2 \propto \exp(-r\Gamma_a/\hbar v_{ph})$ because of the complexity of the photoelectron energy $E_0 + i\Gamma_a/2$. The eikonal approach employs the time dependent representation of the electron wave function $\psi(t) \propto \exp(-\Gamma_a t/2\hbar)$ [13]. In the case of photoelectrons propagating through the solid medium, electron scattering reduces the effective attenuation length, i.e. compared to a free atom, the distance between the photoelectron and the ion at the moment of the Auger decay is reduced. This can be described through an additional contribution $\Gamma_d = \hbar v_{ph}/L$ to the photoelectron linewidth. Consequently, the effective photoelectron linewidth that should be used within the eikonal approach is given by the sum

$$\Gamma = \Gamma_a + \Gamma_d = \Gamma_a + \frac{\hbar v_{ph}}{L}. \quad (3.3)$$

Similar to the molecular case, the value of the lifetime width Γ_a for atomic sul-

fur can be used also in the case of polymers due to negligible influence of the molecular environment on the *KLL* Auger transition rate. The *L* values corresponding to the EAL, may be obtained from theoretical calculations or experimental measurements. To our knowledge, no EAL measurements neither in P3HT nor in PT polymer samples in the range of the photoelectron energies relevant for our experimental conditions have been reported to date. We have therefore used calculated values obtained using the NIST Electron Effective-Attenuation-Length Database tools [129,130]. More details on the calculation of the EAL factors can be found in the following subsection.

Combining the effects of charge screening and electron scattering in the bulk medium we replace within the eikonal approach all Coulomb potentials e^2/r by the screened ones $e^2/\epsilon r$ and the atomic lifetime width Γ_a by the effective photoelectron width Γ . With these substitutions quantum mechanical calculations within the eikonal approach [13] lead to the following expression for the PCI energy shift in a non-metallic medium

$$\Delta E = \frac{\Gamma}{2\hbar\epsilon} \left(\frac{e^2}{v_{ph}} - \frac{e^2}{|\mathbf{v}_A - \mathbf{v}_{ph}|} \right), \quad (3.4)$$

where the effective photoelectron linewidth Γ is given by the Eq. (3.3). Applicability condition of the generalized Eq.(3.4) remains the same as in the case of an isolated atom: $\Delta E \ll E_{ph}$. However, the restriction for the excess energy changes due to the renormalization of the electric charge and the modified photoelectron effective width: $E_0 \gg (\Gamma/\epsilon)^{2/3} E_H^{1/3}/2$.

Furthermore, if under the experimental conditions the emission direction of the electrons is not fixed, the eikonal PCI energy shift provided by Eq.(3.2) or Eq.(3.4) has to be integrated over all the photoelectron and the Auger electron emission angles [13,110,111]. This leads to the final expression for the PCI shift in solid medium

$$\Delta E = \frac{\Gamma}{2\hbar\epsilon} \left(\frac{e^2}{v_{ph}} - \frac{e^2}{v_A} \right), \quad (3.5)$$

which we apply for our sulfur Auger *KLL* measurements in P3HT and PT samples.

3.2.1 Electron effective attenuation length

To calculate the electron effective attenuation length EAL (L in Eq. (3)) [131], we used the NIST Standard Reference Database tools 71 and 82 [129, 130].

To describe photoelectron scattering within the polymer media, the EAL calculations account for both inelastic and elastic scattering contributions. Inelastic scattering enters the EAL in the form of the inelastic mean free path (IMFP), average distance between successive inelastic collisions of an electron moving in a medium with a given energy [132]. Elastic scattering enters the EAL as the transport mean free path (TMFP), average distance that the electron must travel before its momentum in the initial direction of the motion is reduced, by elastic scattering alone, to $1/e$ of its initial value [133]. As an example, in Table 3.1 we show IMFP and TMFP values for both P3HT and PTC calculated at a photoelectron kinetic energy of 50 eV.

Table 3.1: IMFP and TMFP values for P3HT and PTC calculated at a photoelectron kinetic energy of 50 eV.

Sample	IMFP (Å)	TMFP (Å)
P3HT	4.2	6.6
PTC	3.9	6.9

The EAL depends on the depth from the surface into the material z , electron emission angle with respect to the surface normal α , IMFP and TMFP.

Fig. 3.1 shows a dependence of the EAL on the photoelectron kinetic energy calculated for P3HT at $z = 1 \text{ \AA}$, and $z = 8 \text{ \AA}$. The former depth value was also used in the calculations shown in Fig. 3.5. The NIST tools set a limitation of 50 eV as a bottom threshold for the electron kinetic energy. This is because the relativistic TPP-2M (Tanuma, Powell and Penn) equation used to simulate the IMFP is not reliable in the optical range below 50 eV [134]. EAL values were calculated within the $\sim 50\text{--}200$ eV photoelectron

kinetic energy range, corresponding to the excess photon energy E_0 . Sampling was done every ~ 10 eV. The input parameters include the atom fraction of polymer component, the number of valence electrons, band-gap and density. The atom fractions used are H = 0.56, C = 0.4 and S = 0.04, and a density = 1.1 g/cm³ [135]. The number of valence electrons was set to 2, and the band gap was set to 2 eV [136].

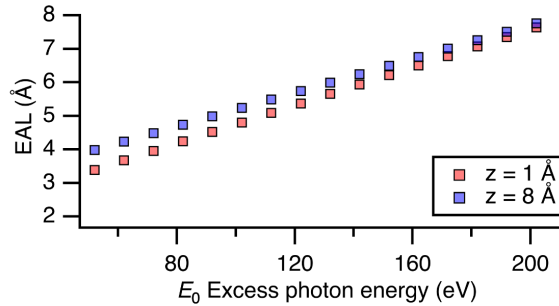


Figure 3.1: EAL as a function of photoelectron kinetic energy calculated for P3HT at $z = 1$ Å (orange squares), and $z = 8$ Å (purple squares).

To demonstrate how each parameter affects the PCI shift, Fig. 3.2 shows ΔE and its dependence on z and ϵ for P3HT.

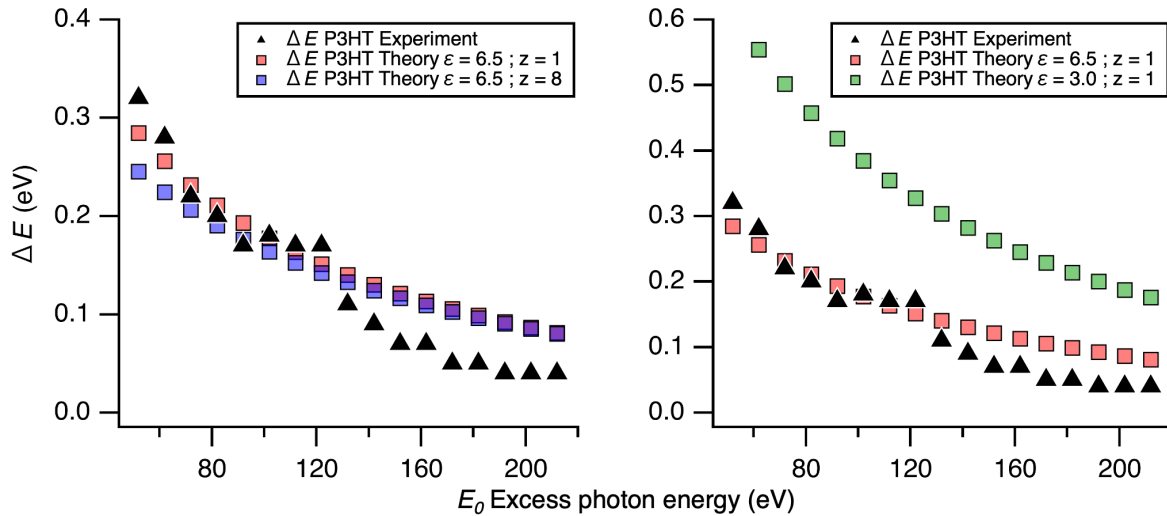


Figure 3.2: Left: calculated PCI shift for P3HT at $z = 1$ Å (orange squares), $z = 8$ Å (purple squares). Right: calculated PCI shift for P3HT at $\epsilon = 3$ (green squares), $\epsilon = 6.5$ (orange squares). Experimental data in black triangles.

3.3 Experiment

The experiments were performed at the French national synchrotron facility SOLEIL, GALAXIES beamline [67], on the high-resolution HAXPES end-station dedicated to hard-x-ray photoelectron spectroscopy [69]. Linearly polarized light is delivered by a U20 undulator and the photon energies are selected by a Si(111) double-crystal monochromator. Incoming electrons are analyzed by a large-acceptance angle EW4000 Scienta hemispherical analyzer, whose lens axis is set parallel to the polarization vector of the incoming beam. A pass energy of 200 eV and a curved slit of 0.3 mm width were used in the experiment. The instrumental resolution was estimated at ~ 180 meV and the photon bandwidth δE provided by the beamline was ~ 225 meV and ~ 380 meV at 2.5 keV and 3.5 keV photon energy, respectively. Note that the photon bandwidth does not contribute to the experimental resolution of the normal Auger spectra.

Pure liquid thiophene was purchased from Sigma Aldrich, and was subjected to three freeze-pump-thaw-degassing cycles. Thiophene vapor present in the head-space above the liquid was slowly injected into a gas cell with the use of a micro-leak valve and kept at a constant pressure of $\sim 10^{-5}$ mbar in the experimental chamber, which was sufficiently low to consider the molecules as isolated.

P3HT purchased from Sigma Aldrich was dissolved in CHCl_3 to a concentration of 5 mg/mL and spin-coated on an indium-tin-oxide (ITO) substrate at ~ 2000 RPM. The obtained P3HT film was placed on the metal sample-holder and kept in place with carbon tape, which also served as a conductor connecting the sample to the metal holder.

The PT sample was prepared as a blend of pure PT powder and graphite powder, in approximately equal amounts, both purchased from Sigma Aldrich. Preparation of the blend, denoted as PTC in the following, allowed us to tackle the space-charge build-up, which can shift and distort the energy distribution of the Auger electrons [93]. Equivalent amounts of polythiophene and graphite powders were finely ground together until

a homogeneous blend was obtained. The resulting powder was deposited on the carbon tape, ensuring the entire surface was covered, and fixed on the metal sample-holder. Additionally, carbon tape was placed along the perimeter of the PTC blend improving the electric connection between the surface of the sample and the sample-holder.

P3HT and PTC samples were placed in the preparation chamber of the HAXPES end-station and subsequently transferred to the main chamber. In order to avoid radiation damage to the samples, intensity filters were introduced in the beam and the samples were continuously moved during the measurements.

Auger *S KLL* electron spectra were measured in gas phase thiophene, P3HT film and PTC powder blend at the photon energies from 2475 eV to 3500 eV with variable steps, these are described in the following. A low-excess energy data set, from ~ 0 to 5 eV above threshold with an energy step of 0.5 eV. A mid-excess energy data set, from ~ 5 to 20 eV above the ionization threshold, with an energy step of 1 eV. A high-excess energy data set from ~ 20 to 200 eV above threshold, with an energy step of 10 eV. In addition, two measurements were performed at ~ 500 eV and ~ 1000 eV above threshold, in order to assert an incident photon energy where the PCI shifts are absent. The electron kinetic energy and the photon energy were calibrated using the Argon *LMM* Auger and Argon $2p^{-1}$ and $1s^{-1}$ photoelectron spectra [82, 137] measured under the same experimental conditions.

Note, that in the gas phase experiments the kinetic energy of the detected electron is naturally measured with respect to the vacuum level (VL) [86]. However, in solid state experiments the electrons ejected from the sample must overcome an additional potential barrier at the surface, known as the sample work function, which results from the energy difference between the vacuum level and the Fermi level (FL). If the sample and the spectrometer are in a good electric contact (as is the case in our experiment), an electron exchange between them results in a common FL. The kinetic energy of the electron ejected from the sample and propagating to the analyzer is further modified by the spectrometer

work function ϕ_{SP} [86]. In our calibration measurement using the Au $4f_{7/2}$ photoline we obtained $\phi_{SP} = 4.90(1)$ eV. Therefore, in P3HT and PTC the electron kinetic energy referenced to the FL, is shifted by the latter amount towards higher values with respect to the kinetic energies measured by the spectrometer.

It is convenient to trace the evolution of the PCI energy shift as a function of the excess energy E_0 , which is defined above in the atomic case as the difference between the incident photon energy and the S 1s IP. Therefore, in the gas phase measurements, the reference photon energy E_{γ}^{ref} , where the excess energy $E_0 = 0$ eV, equals the S 1s IP.

The S 1s IP in thiophene was determined using S 1s photoelectron spectra recorded at 2700 eV photon energy. The obtained value IP=2478.6(3) eV is in good agreement with the 2478.4(5) eV value reported in earlier investigations for the gaseous thiophene [138].

In solid samples the IP, generally measured with respect to the FL, lies below the near edge x-ray absorption fine structure (NEXAFS) features. Therefore, for a consistent comparison to the gas phase measurements, we define the reference photon energy E_{γ}^{ref} in our solid samples by adding the term value of 5.0(3) eV, found for the first S 1s NEXAFS feature in gaseous thiophene [138], to the energy of the equivalent S 1s NEXAFS feature in PT [53] and P3HT [139]. The obtained reference photon energy values, where the excess energy $E_0 = 0$ eV, are $E_{\gamma}^{ref} = 2477.6$ eV for PT and $E_{\gamma}^{ref} = 2478.2$ eV for P3HT.

To extract the position of the Auger S *KLL* line as a function of the photon energy, the Auger spectra were fitted using the SPANCF fitting suite for Igor Pro [81]. At photon energies where peak distortion caused by the PCI effect was deemed negligible, the spectra were fitted with Voigt profiles and a Shirley background, where necessary. The width of the Lorentzian component in the Voigt function was fixed to the S $1s^{-1}$ core-hole lifetime broadening of 0.59 eV [47]. At photon energies close to E_{γ}^{ref} , the Auger electron spectra were fitted with asymmetric PCI profiles based on Ref. [110].

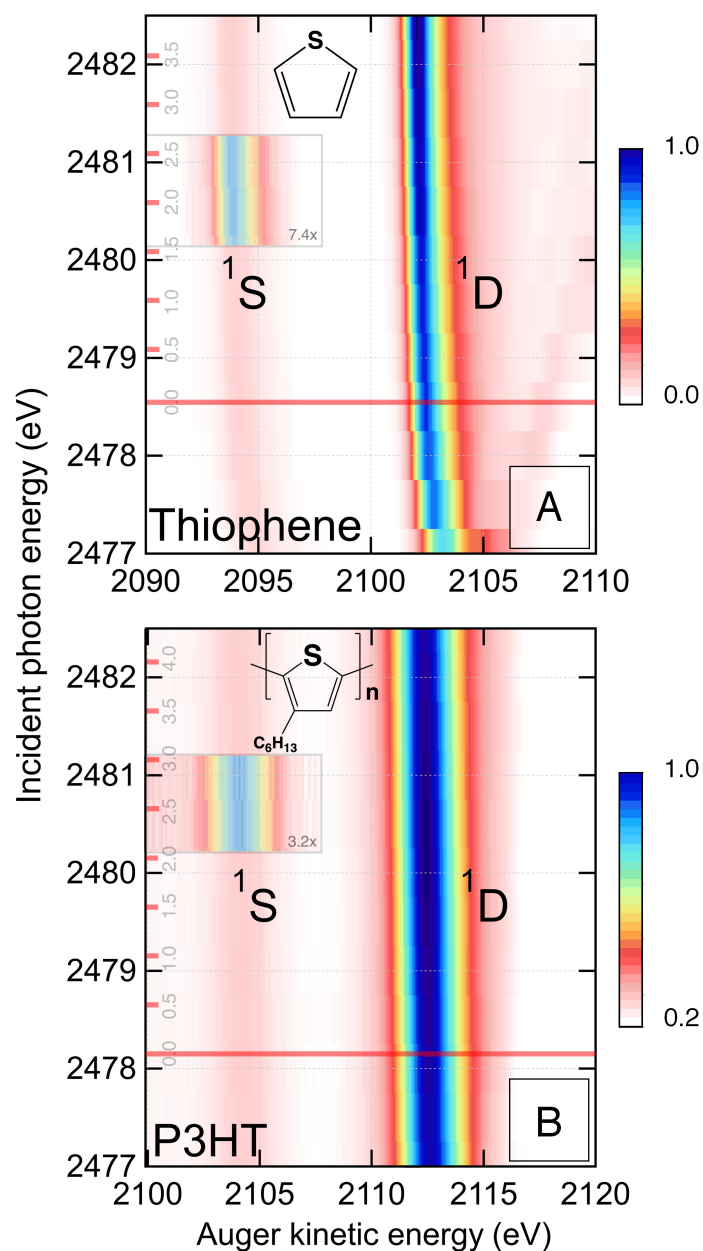


Figure 3.3: 2D maps of S $KL_{2,3}L_{2,3}$ Auger spectra recorded in A: thiophene, B: P3HT. Red horizontal lines show the reference photon energy E_{γ}^{ref} , where the excess energy $E_0 = 0$ eV. Multiplet lines corresponding to the $1S$ and $1D$ terms of the $2p^{-2}$ final-state configuration are labelled in the 2D maps. Red ticks, and adjacent labels correspond to the E_0 scale. Insets show the $1S$ term with intensity scaled by a factor of 7.4 and 3.2 for thiophene and P3HT, respectively.

3.4 Results and Discussion

The S $KL_{2,3}L_{2,3}$ Auger spectra for thiophene and P3HT are presented in Fig. 3.3 as 2D maps showing Auger electron kinetic energies as a function of the incident photon energy. The intensity is represented by a color scale. The maps are normalized to the integrated intensity. In PTC the measurements were limited to selected photon energies, which explains the absence of a 2D map. The shown Auger spectra were recorded at photon energies varying with a step of 0.5 eV around the reference photon energy E_{γ}^{ref} , which is marked on the maps with a red horizontal line. The Auger spectra observed at the photon energies below E_{γ}^{ref} correspond to the relaxation of the intermediate states resulting from resonant excitation to the densely lying unoccupied orbitals, which in the case of polymers form a conduction band. In Fig. 3.3 B, the Auger electron kinetic energy is shown with respect to the FL as in the previously reported Auger S KLL spectra in P3HT [139]. The S KLL Auger spectrum consists of three multiplet lines corresponding to the 1S , 1D and 3P (not shown in the maps due to low intensity) terms of $2p^{-2}$ final-state configuration. Our analysis is focused on the strongest $2p^{-2}(^1D)$ multiplet line. We expect identical results for the less intense $2p^{-2}(^1S)$ and $2p^{-2}(^3P)$ lines.

The PCI effect can be observed in the 2D maps as a distinctive blueshift of the $2p^{-2}(^1D)$ spectral line as the photon energy decreases and approaches E_{γ}^{ref} . The S KLL Auger spectra zoomed in around the $2p^{-2}(^1D)$ line are shown in Fig. 3.4 for thiophene, P3HT and PTC for selected excess photon energies. Again, the Auger electron kinetic energy of the polymers is shown with respect to the FL. The black vertical dashed line marks the maximum of the $2p^{-2}(^1D)$ line in the Auger spectra measured at high E_0 values, where alteration induced by the PCI effect is absent (see Table 3.2 for the position of the black lines). Red vertical dashed lines show the $2p^{-2}(^1D)$ spectral line maximum in the spectra measured at the lowest E_0 value for each system, where the line distortion and magnitude of the PCI shift ΔE are the largest. In the following, the Auger electron kinetic energy values summarized in Table 3.2, will serve as a reference for calculating the PCI

shift with respect to the "unshifted" spectral line.

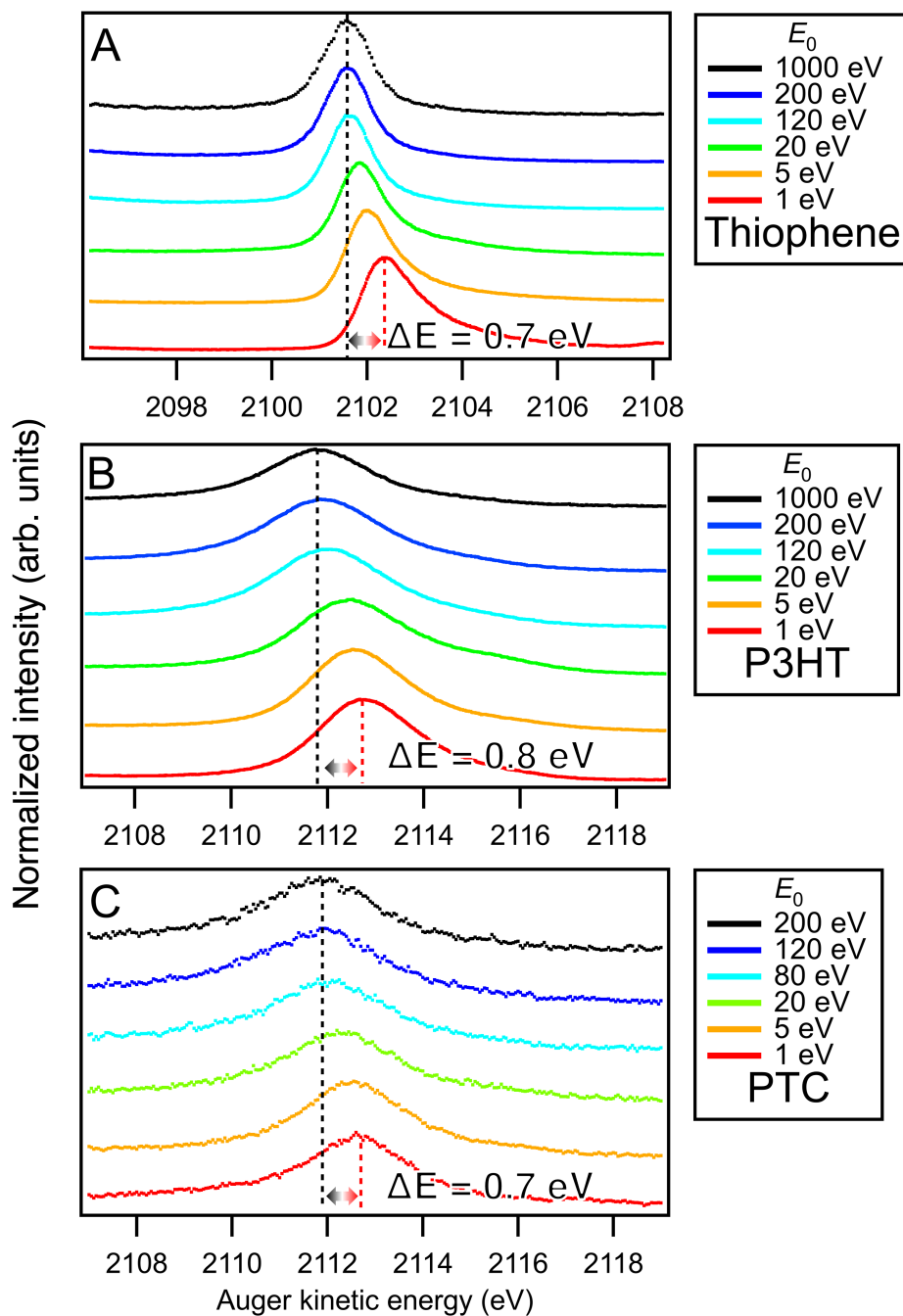


Figure 3.4: Experimental S $KL_{2,3}L_{2,3}(^1D)$ Auger line profiles for selected excess photon energies E_0 for thiophene (A), P3HT (B), and PTC (C). Vertical dashed lines show the position of the spectral line at the highest (black) and at the lowest (red) values of E_0 . The magnitude of the PCI shift measured at the lowest E_0 value is shown for each system.

In thiophene (Fig. 3.4 A), we observe the PCI-induced distortion of the Auger line, resulting in a strong asymmetry towards high kinetic energies as the E_0 decreases. This distortion is less pronounced in P3HT and PTC (Fig. 3.4 B and C), which is probably related to the significant inhomogeneous broadening of the Auger line in the polymer samples compared to the gaseous thiophene.

Table 3.2: Position of the $S KL_{2,3}L_{2,3}(^1D)$ spectral line in the Auger electron spectra in thiophene, P3HT and PTC, measured at high excess photon energy E_0 where PCI shifts are absent. Uncertainties in E_0 and E_{kinetic} estimated from photon and kinetic energy calibration procedures.

Sample	E_0 (eV)	E_{kinetic} (eV)
Thiophene	1000.0(3)	2101.60(1)
P3HT	1000.0(3)	2111.80(1)
PTC	200.0(3)	2111.90(1)

The PCI shift ΔE observed at the lowest E_0 value with respect to the position of the unshifted Auger line (marked by the black dashed line), has approximately the same magnitude in thiophene ($\Delta E = 0.7$ eV) and in both polymers ($\Delta E = 0.8$ eV and 0.7 eV for P3HT and PTC, respectively). However, the evolution of the PCI shift with the excess photon energy E_0 is different. In thiophene, at $E_0 = 120$ eV and above, the asymmetry is imperceptible, and the line shift is close to zero. In contrast, in P3HT and PTC, the PCI shift is still appreciable at $E_0 = 120$ eV.

The experimentally measured PCI shift of the $S KL_{2,3}L_{2,3}(^1D)$ Auger line ΔE as a function of excess photon energy in thiophene, P3HT, and PTC, is shown in Fig. 3.5 together with the theoretical results obtained within the eikonal approximation outlined above. Error bars correspond to the statistical error with a confidence interval of 95%. The inset shows the $E_0 = 0$ –25 eV range in greater detail. Remarkably, apart from the threshold energy region, both P3HT and PTC polymers clearly show a stronger PCI line shift compared to the gas phase thiophene molecule up to $E_0 = 150$ eV. At higher excess photon energies, ΔE gradually converges to zero for all systems. A close proximity of the results for the two polymer samples can be attributed to their similar density and dielectric permittivity. Different morphology of the samples in the form of powder (PTC)

and a film (P3HT) has no apparent effect on the PCI shift.

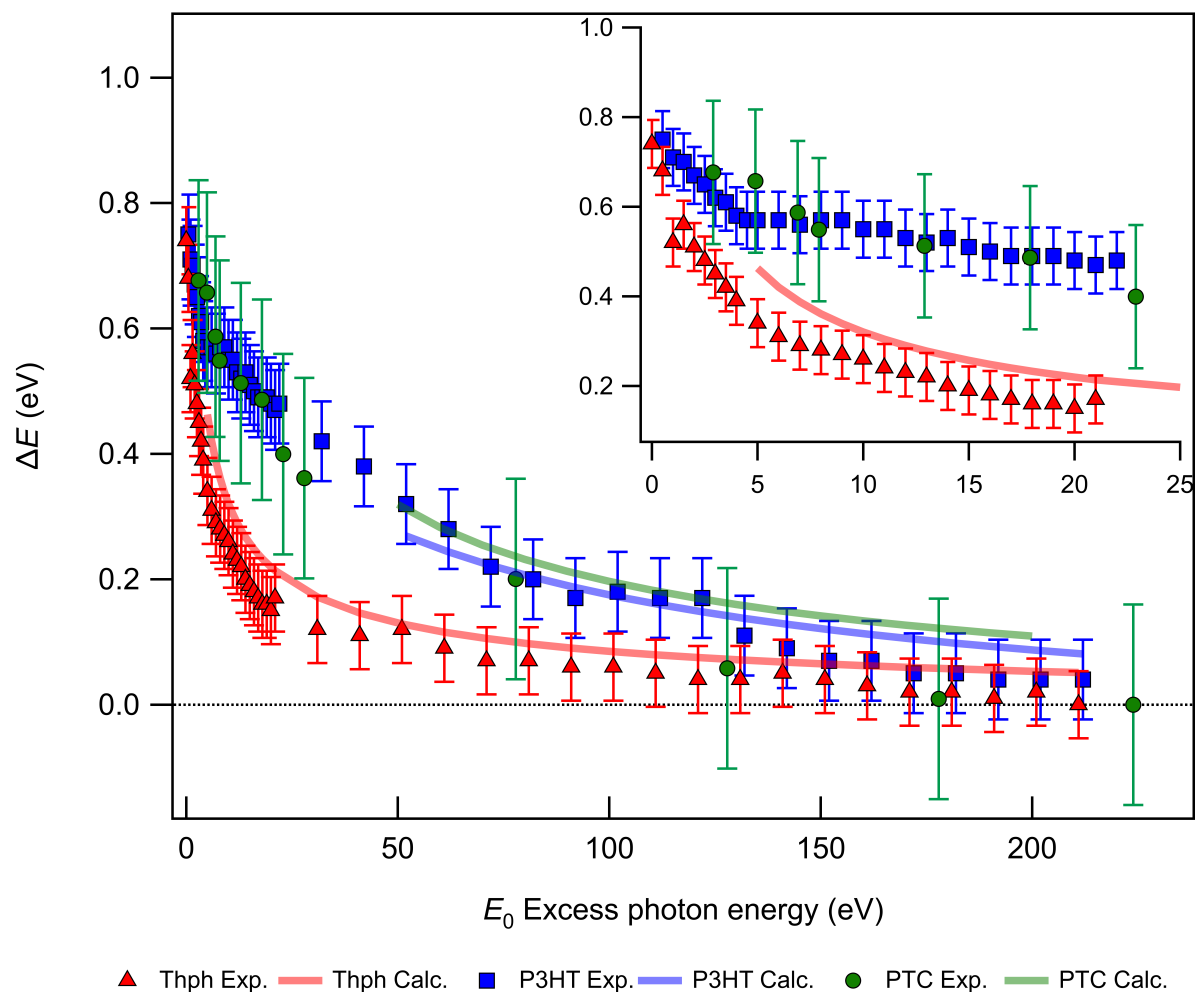


Figure 3.5: Measured (thiophene: red filled triangles, P3HT: blue filled squares, PTC: green filled circles) and calculated (red continuous lines for thiophene, blue for P3HT, green for PTC) PCI shift of the $S KL_{2,3}L_{2,3}(^1D)$ Auger line ΔE as a function of excess photon energy above the $S 1s$ ionization threshold. Horizontal dotted line corresponds to $\Delta E = 0$. The inset shows the 0–25 eV range in detail. Error bars on measured data correspond to statistical error with a confidence interval of 95%.

Theoretical results obtained using Eq. (3.2) for thiophene (continuous red line) and Eq. (3.5) for P3HT (continuous blue line) and PTC (continuous green line) are shown in Fig. 3.5. A very good overall agreement between the experimental data and the theoretical results is observed.

For gas phase thiophene, the divergence from the experiment visible at $E_0 < 10$ eV

(see inset), is related to the limitation of the eikonal approximation close to the ionization threshold (see [4] and discussion in Section 2), and therefore we do not show calculations below $E_0 = 5$ eV. Nevertheless, a reasonable agreement at higher E_0 , demonstrates the validity of our model using the eikonal approximation for the PCI effect in relatively large organic molecules.

As regard the polymers, the calculations are limited to the $E_0 > 50$ eV range due to a limitation imposed by the NIST Electron Effective-Attenuation-Length Database tools [129, 130]. Nonetheless, an excellent agreement obtained at the accessible range of excess photon energies, corroborates our model proposed to describe the PCI effect in a solid medium (see Eq. (3.5)).

Propagation of a slow photoelectron in the polymers is strongly influenced by elastic scattering affecting the electron trajectory and thus reducing the distance that it can travel before the Auger decay occurs. Furthermore, inelastic scattering may lead to electron energy loss. Both types of scattering result in the enhancement of the PCI effect. On the other hand, the dielectric medium efficiently screens the electron charges and, thus, affects the Coulomb interaction between the photoelectron and the Auger electron, leading to a reduction of the PCI effect. Therefore, the resulting PCI shift depends on the interplay of the two competing effects of the solid environment on the interacting electrons.

The PCI shift observed in the $10 \lesssim E_0 \lesssim 120$ eV region, is on average approximately two times larger in the polymers than in thiophene molecule. According to Eqs. (3.2) and (3.5) amplification is given by the ratio $(\Gamma_a + \Gamma_d)/\Gamma_a \epsilon$. On the one hand, the damping width Γ_d is in the order of ~ 7 – 8 eV over the considered E_0 region, whereas $\Gamma_a = 0.59$ eV, leading to PCI shift amplification by about a factor of 13 due to electron scattering. On the other hand, dielectric screening reduces the shift by a factor of 6.5. A combination of both effects ultimately doubles the PCI shift in polymers.

At $E_0 < 10$ eV the difference between the PCI energy shifts in polymers and the

molecule decreases and eventually disappears at the photoionization threshold. Despite the lack of calculations for EAL and the corresponding values of Γ_d for $E_0 < 50$ eV, the observed trend implies a reduction of the electron damping width Γ_d in this energy region.

A strong reduction of the PCI effect previously observed in XPS spectra of rare-gas clusters, compared to the isolated atoms, was interpreted by dielectric screening of the electron charge propagating in the cluster bulk [101]. However, a possible effect of electron scattering on the PCI effect had not been considered. One can assume that in a relatively small-size medium such as clusters with mean size $\langle N \rangle \approx 1600$ as considered in Ref. [101], photoelectron scattering does not play an essential role for the PCI shift, whereas polarization screening has a dominant effect on PCI. In contrast, in extended solid media, such as the polymers considered in our work, both elastic and inelastic electron scattering play a preponderant role in the PCI effect and overtake the diminishing effect that polarization screening may have.

3.5 Conclusion

In this paper we present an investigation coupling experimental and theoretical results of the PCI effect in thiophene and thiophene-based polymers. We have studied the $KL_{2,3}L_{2,3}$ Auger decay spectra in gaseous thiophene and in solid state organic polymers polythiophene and poly(3-hexylthiophene-2,5-diyl).

The PCI between Auger electron, photoelectron and residual doubly charged ion has been observed in all samples. The interaction manifested itself as a significant distortion and a blue-shift of the Auger spectral lines close to the ionization threshold. The PCI shift, reaching a value close to ~ 1 eV just above the ionization threshold, is gradually reduced with increasing photon energy. However, it remains visible up to ~ 150 eV above the ionization threshold.

Furthermore, we have shown that in solid state samples, the PCI effect is signifi-

cantly larger between $10 \lesssim E_0 \lesssim 120$ eV, compared to the gas phase molecule. We propose a model for the PCI in condensed matter, based on the eikonal approximation, which takes into account the effect of the polarization screening of the electron charges in the dielectric medium and the effect of photoelectron scattering. While the dielectric permittivity of the medium screens the electron charges and reduces the PCI effect, electron scattering counterbalances this reduction, decreasing the travel distance of a slow photoelectron in the medium, thus, enhancing the PCI effect.

Apart from these findings, a very good agreement between experimental and theoretical results in thiophene demonstrates the validity of the eikonal approximation for the PCI description in relatively large organic molecules.

Our work paves the way towards future investigations of the interplay between charge screening and electron scattering for PCI in various media. The general nature of the PCI effect, showcased in our work in an isolated organic molecule and in solid organic polymers, calls for further studies of PCI in cluster, liquid and solid media.

Chapter 4

Electron delocalization in conjugated polymers

4.1 Introduction

The process of charge transfer (CT) involving electron and nuclear dynamics is a long-standing research topic, which nevertheless remains bustling, essentially due to its significance for multiple applications in chemistry, biology and materials sciences [140]. Continuous progress in experimental and theoretical methods provides for an increasingly deeper understanding of the CT process. Rapid development of time-resolved spectroscopy allows nowadays probing the dynamics of CT in various systems on femtosecond and even attosecond timescale [141]. In complex systems, the control over nuclear and electron dynamics in time and space requires for a localized excitation of the CT process. This can be achieved by X-ray sources allowing for element-specific core-shell excitation. A combination of attosecond resolution with the X-ray photon energy range is at the heart of the current developments at free-electron laser and high-harmonic sources [40, 142, 143].

Meanwhile, high-resolution X-ray spectroscopy in the energy domain can also provide a useful insight into ultrafast dynamical processes in molecular systems. Using monochromatic synchrotron X-ray radiation, resonant excitation of a specific atomic core-shell in a molecule becomes possible. The lifetime of a core-excited state varies from a few femtoseconds for relatively shallow core holes with excitation energy up to 1 keV, down to the attosecond timescale for deep core holes with higher excitation energy. Relaxation of a resonantly core-excited molecule via emission of an X-ray photon or an Auger electron, occurring within the lifetime of a core-excited state, can serve as a probe of any dynamical process taking place in the molecule on the same timescale. This is the basic concept of “core-hole clock” spectroscopy (CHCS) [28] (introduced in Chapter 1). Didactic reviews on applications of CHCS in relation to various CT processes can be found in Refs. [30] and [31].

X-ray induced site-specific electron dynamics, monitored by CHCS, offers an exciting opportunity to explore the conduction properties of macromolecules. A remark-

able example of attosecond intramolecular electron delocalization in a genomic DNA molecule was demonstrated using resonant Auger spectroscopy of the powdered samples pressed onto a solid substrate [44]. The mechanism of electron delocalization was attributed to the presence of extended unoccupied electronic states along the phosphate groups in the DNA backbone. This finding may constitute an additional pathway of CT in DNA, along with the widely accepted mechanism of long-range charge transport through the π -stacked arrays of bases of the DNA double-helical structure [144]. Importantly, the intramolecular conductivity of DNA is directly related to its structural integrity and therefore, can serve for the diagnostics and repair of the radiation induced damage [145].

The phenomenon of electron dynamics in organic molecules is also of great relevance in optoelectronics, where charge transport in organic polymers is the key issue for the efficiency of organic photovoltaic devices. In conjugated polymers characterized by a sequence of alternating single and double bonds, electric conduction is mainly due to the π -electrons delocalized over several carbon atoms along the polymer backbone. Apart from delocalization of π -electrons, key factors for charge transport are inter-chain π - π stacking interactions through the aromatic rings and side groups [49, 146].

The conduction properties of conjugated polythiophene polymers were explored in [52] using CHCS upon resonant excitation of sulfur atoms near the S K -edge. Interestingly, no signature of electron delocalization has been observed in the resonant Auger spectra of the powdered samples. However, a subsequent study of the same polymer deposited on a substrate as a thin film clearly revealed electron delocalization in the low-femtosecond regime [53]. This effect was attributed to the interaction between the polymer chains in the highly ordered films, since in powder form, the electrons may only be delocalized along the polymer chain (intra-chain mechanism), while in polymer films the delocalization path can be two-fold: intra-chain and/or between the polymer chains (inter-chain mechanism). However, experimental restrictions in the previous studies [52, 53], in terms of a limited number of the recorded Auger spectra and their insufficient statistical quality, may have affected the reliability of the spectral assignment, which

results in ambiguity concerning the role of polymer chain ordering in oriented films for the electron transport.

In the light of the discussions presented above, concerning electron delocalization in conjugated polythiophene, the motivation for our work is to find answers to the following open questions: What is the dominant mechanism of electron delocalization in thiophene-based polymer powders and films upon resonant excitation at the S *K*-shell - along the polymer backbone (intra-chain) or through the π - π stacks (inter-chain)? Can we control the electron localization/delocalization by selective excitation of a specific resonance in the sulfur atom? Can we quantify the probability of electron delocalization from the specific core-excited state?

In this paper we address the issue related to the mechanism of CT in sulfur-containing polymers - polythiophene (PT) powder and poly(3-hexylthiophene-2,5-diyl), commonly known as P3HT, film. The CT is locally induced by resonant excitation of sulfur atoms at the S *K*-shell and monitored by RAS. Our experimental results reveal the signature of CT in both P3HT film and in PT powder occurring on the low-femtosecond timescale. The fact that CT is observed both in powder and in film points towards the dominance of an intra-chain electron delocalization mechanism. Theoretical analysis of the dynamic processes, using real-time time-dependent density functional theory (RT-TDDFT) and Ehrenfest molecular dynamics (EMD) simulations, confirms this hypothesis. Furthermore, our detailed theoretical analysis reveals that the CT process along the polymer chain can only be initiated upon the resonant excitation of the S $1s^{-1}\sigma^*$ state, whereas the resonant excitation of the S $1s^{-1}\pi^*$ state does not lead to electron delocalization. The electron dynamics simulations show that CT occurs on a sub-femtosecond timescale upon creation of the S $1s$ core hole, which compares reasonably well with the experimental estimate. This detailed mechanistic insight in the ultrafast electron/nuclear dynamics in core-level excitation in complex extended systems is made possible by an efficient implementation of RT-TDDFT in the CP2K software [147].

4.2 Experiment

The experiments were carried out at the SOLEIL French national synchrotron facility using the high-resolution HAXPES station for hard X-ray photoemission spectroscopy [69] located at the GALAXIES beamline [67]. Linearly polarized light was provided by a U20 undulator followed by a Si(111) double-crystal monochromator. Electrons were detected by a large-acceptance angle EW4000 Scienta hemispherical analyzer, the lens axis of which was parallel to the polarization vector of the incident beam. A 200 eV pass energy and a 0.3 mm width curved slit were used for the measurements. The spectrometer resolution was determined at ~ 180 meV while the beamline photon bandwidth δE was ~ 225 meV at 2.5 keV photon energy. The measurements were performed at close to normal incidence of the X-ray beam with polarization vector parallel to the sample surface. To avoid radiation damage to the samples, these were continuously moved during the measurements and filters were used, when necessary, to reduce the intensity of the X-ray beam.

The PT sample consists of a blend of polythiophene powder and graphite powder purchased from Sigma Aldrich. Use of such a blend served to tackle the space-charge build-up, which can severely alter the energy distribution of Auger lines [93]. Equal amounts of polythiophene and graphite powders were ground together until a homogeneous mixture was obtained. The blend was deposited on carbon tape, covering the entire surface, and then fixed on a metal sample-holder. Additional carbon tape was fixed along the perimeter of the sample, increasing electric connectivity between the sample surface and metallic sample-holder.

The P3HT film was prepared by spin coating the 0.5 wt% solution of regio-regular P3HT powder (Sigma Aldrich) in CHCl_3 , onto an indium-tin-oxide (ITO) substrate at ~ 2000 RPM. The resulting film was placed on a metal sample holder and secured with carbon tape, also serving as an electrical conductor. More details on sample characterization can be found in the next subsection.

The presence of a good electric contact between the samples and the spectrometer in our experiment results in a common Fermi level (FL). This allows referencing the kinetic energy of electrons emitted from the samples with respect to the FL by adding the spectrometer work function ϕ_{SP} to the measured electron kinetic energy. Our calibration on the Au $4f_{7/2}$ photoelectron line provides $\phi_{SP}=4.9$ eV. The incident photon energy was calibrated by using S K -edge X-ray absorption spectra of PT powder from Ref. [52], and P3HT films from Ref. [148], where the absorption spectra were obtained by recording the drain current of the samples.

Resonant Auger S $KL_{2,3}L_{2,3}$ electron spectra were measured at photon energies ranging from 2470 eV to 2475 eV with a step of 0.1 eV. Such a fine photon energy step, along with high statistics, allowed presenting the data in the form of 2D maps, where the Auger electron spectra are shown as a function of both the Auger electron kinetic energy and the incident photon energy.

To extract information from the Auger spectra, these were fitted using the SPANCF fitting suite for Igor Pro [81]. For both polymers Voigt profiles were used, where both Lorentzian and Gaussian components were set as free parameters. Two Shirley backgrounds were used during the fit, to accurately account for the increased intensity at lower kinetic energies caused by inelastic scattering contribution.

Sample characterization

Depending on the procedure used for a P3HT film preparation, two orientations of the polymer chains on the substrate are possible [94]. In the edge-on orientation, the self-organized lamellar sheets are positioned perpendicular to the substrate, while in the face-on orientation, the lamellae are fixed parallel to the substrate.

Following procedures provided in literature [95], we have chosen the rotational spin-coating frequency of 2000 RPM and the CHCl_3 solution concentration of 5 mg/ml that lead to formation of a film with face-on orientation. Furthermore, our X-ray diffrac-

tion analysis of the film, using a Cu $K\alpha$ source in a symmetric $\theta/2\theta$ geometry, revealed a signature at 24° corresponding to inter-chain $\pi - \pi$ stacking, which indicates a face-on orientation of the film [96,97]. In addition, no sharp structures typical for an edge-on orientation were observed. The ~ 34 nm thickness of the P3HT film was determined using atomic force microscopy.

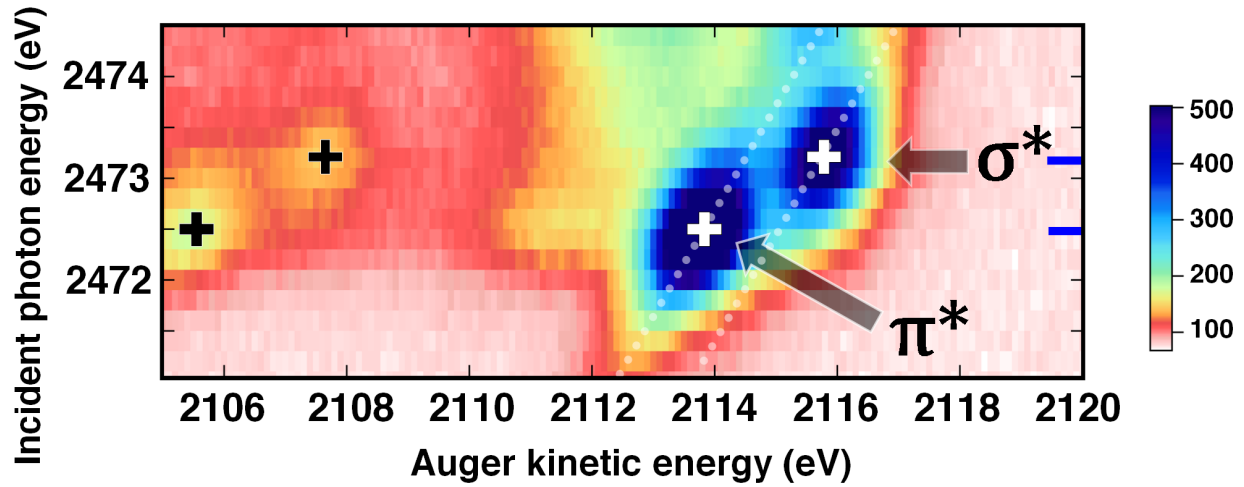


Figure 4.1: 2D maps of $S KL_{2,3}L_{2,3}$ Auger spectra recorded in P3HT film at grazing incidence. Transitions to the $2p^{-2}(^1S)\pi^*$ and $2p^{-2}(^1S)\sigma^*$ final states are indicated with black crosses. Transitions to the $2p^{-2}(^1D)\pi^*$ and $2p^{-2}(^1D)\sigma^*$ states, indicated with white crosses, are labeled as π^* and σ^* . Blue lines indicate the corresponding resonant photon energies. Diagonal dotted lines show dispersive behavior of resonant structures. The map is normalized to the background. The color-coded intensities are on a logarithmic scale.

The measurements presented in Fig. 4.4 were performed at normal incidence with the polarization of the incident X-ray beam parallel to the sample surface. Assuming a face-on orientation of the P3HT film, in this geometry one can expect a dominant excitation of the $S 1s^{-1}\sigma^*$ state. Indeed, this can be observed in Fig. 4.4. For comparison, Fig. 4.1 shows a 2D map of $S KL_{2,3}L_{2,3}$ Auger spectra for P3HT measured in grazing incidence geometry, where the X-ray beam polarization is perpendicular to the sample surface, leading to a primary excitation of the $S 1s^{-1}\pi^*$ state. Note, that a dominant excitation of the $S 1s^{-1}\pi^*$ state in the case of grazing incidence geometry and a resulting overlap of the strong resonant $2p^{-2}\pi^*$ feature with a weak low-energy peak, prevents us from a reliable fitting analysis in the whole photon energy range of the 2D map and therefore, does not

allow revealing a possible CT process in this geometry.

A strong angular dependence observed for the P3HT sample, demonstrating dominant excitation of the $S\ 1s^{-1}\sigma^*$ state for normal incidence, and the $S\ 1s^{-1}\pi^*$ state for grazing incidence geometry, further corroborates the face-on orientation of the P3HT conjugate plane.

Note that our measurements did not reveal angular dependence for the PT powder sample, which is consistent with the isotropic morphology of the powdered polymer. Similarly, measurements (not shown here) of a PT film, prepared using a potentiostatic electrochemical deposition technique, lack angular dependence. This points at a poor organization of the PT film structure, likely related to the imperfect deposition conditions. Therefore, these measurements were excluded from the data analysis.

4.3 Theory

4.3.1 Core-hole clock spectroscopy

The principle of the CHCS method, that we apply to reveal the CT effect, is illustrated in Fig. 4.2 showing the major excitation and decay events occurring in $S\ KL_{2,3}L_{2,3}$ Auger process. If the incident X-ray photon energy $\hbar\omega$ exceeds the $S\ 1s$ ionization threshold, a $1s$ photoelectron (PE) is ejected into the continuum, followed by electron relaxation in the form of normal Auger decay, where one $2p$ electron fills the $S\ 1s$ vacancy, while another $2p$ electron is ejected as an Auger electron (AE). In this case, the final state is di-cationic with two holes (2h) in the $2p$ shell and the Auger electron energy is independent of the incident photon energy.

If the photon energy is insufficient for photo-ionization, a core electron can be resonantly promoted to one of the unoccupied molecular orbitals (MO). In the event of delocalization of the promoted electron to the surrounding environment, the subsequent

relaxation, designated as a CT channel, is unaffected by the delocalized electron, and hence the process is similar to that of normal Auger decay: the final state is also locally di-cationic, while the Auger electron energy is constant and equal to the energy of the normal Auger line.

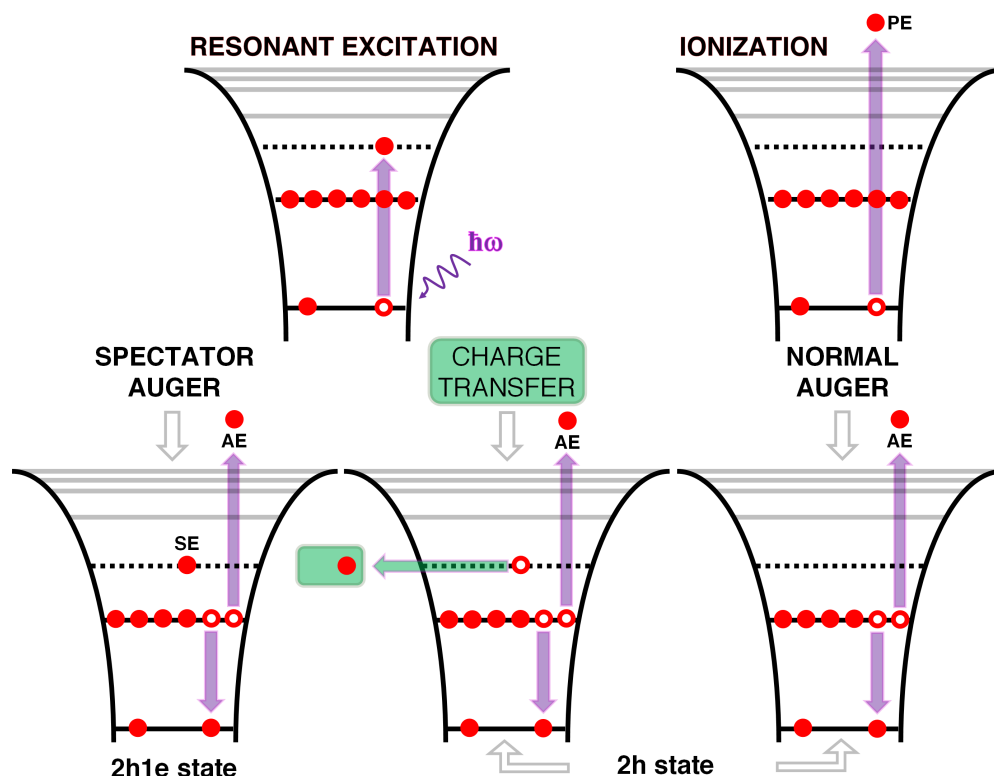


Figure 4.2: Schematic of excitation and decay events upon absorption of an X-ray photon. Ionization with emission of a photoelectron (PE) is followed by the normal Auger decay with emission of an Auger electron (AE). Resonant excitation leads to resonant spectator Auger decay, when the spectator electron (SE) remains localized on the excited atom, or, to a CT decay channel, occurring in the case of delocalization of the resonantly promoted electron to the environment. Green box represents destination environment of the delocalized electron. The spectator Auger decay leads to a mono-cationic final state (2h1e), whereas both the CT and the normal Auger decay channels lead to a di-cationic (2h) final state.

In the case where the promoted electron remains localized on the excited atom, one can talk about resonant Auger relaxation. In resonant Auger $S KL_{2,3}L_{2,3}$ process, the spectator Auger decay (the promoted spectator electron (SE) remains in the excited orbital) strongly dominates over the participator decay (the promoted electron participates in the relaxation process), therefore the latter process will be omitted in the following dis-

cussion. In the case of spectator Auger decay, the final state is mono-cationic ($2h1e$) with two holes in the $2p$ shell and one spectator electron. Here, under resonant Raman conditions, when the experimental resolution is smaller than the lifetime broadening of the core-excited state, and in absence of ultrafast nuclear dynamics in the molecule, a linear relation between the energy of the incident photon and the spectator Auger electron kinetic energy can be observed [149]. Due to the screening of the $2p$ holes by the spectator electron, the resulting spectator Auger kinetic energy is blueshifted with respect to the normal Auger line. The presence of this so-called spectator shift is essential, since it allows separating the spectator Auger channel and the CT channel directly at the resonant excitation photon energy.

The branching ratio between the localized spectator Auger and delocalized CT channels, provides an estimate of the CT rate upon core-excitation. To determine the CT timescale τ_{CT} , the following relation is generally considered valid [30,31,46]

$$\tau_{CT} = \tau_{CH} * \frac{I_{Spectator}}{I_{CT}}, \quad (4.1)$$

where $I_{Spectator}$ and I_{CT} correspond to the integrated intensity of a specific resonant spectator Auger channel and the corresponding CT channel, respectively. $\tau_{CH} = 1.1$ femtosecond corresponds to the core-hole lifetime of the S 1s vacancy [47].

4.3.2 Computational Methods

Kohn-Sham density functional theory (KS-DFT) [150, 151] simulations have been carried out employing the Perdew-Burke-Ernzerhof (PBE) [152] exchange-correlation functional supplemented with Grimme's D3 [153] dispersion correction. The simulations have been performed using the CP2K program, [154] under the Gaussian and plane-wave (GPW) approach. Valence electrons were treated explicitly, and norm-conserving Goedecker-

Teter-Hutter (GTH) pseudopotentials [155] were used to account for the interaction between the valence electrons and the atomic cores. We employed double-zeta valence plus polarization (DZVP) basis sets, and a cutoff of 1000 Ry for the auxiliary plane-wave basis set.

The simulations for P3HT were carried out with a regio-regular model adapted from Ref. [156], shown in Figure 4.3. According to the experimental conditions, the lamellar sheets are positioned in the XZ plane parallel to the sample surface. The model contains two layers of 2×2 units, corresponding to a simulation cell with size of $30.52 \times 15.02 \times 15.93 \text{ \AA}^3$, for which periodic boundary conditions have been applied to all three directions. In one unit, the polymer chains are laterally shifted in the XZ plane by 1.3 \AA with respect to each other, as Figure 4.3(b) shows. The stacking of polymer chains is then ABAB along the y direction. The calculated geometry of the system was fully relaxed until the maximum force component was smaller than $1.0 \times 10^{-4} \text{ Ha/Bohr}$. Electronic structure calculations were performed at 0 K temperature and at the Gamma point of the supercells.

Although the simulations for the measurements of PT powder could not be performed due to the lack of crystalline structure in the sample, we have explored theoretically a PT film constructed by removing the hydrocarbon side chains from the P3HT model, followed by full relaxation of the system's geometry.

To initialize the electronic structure in the $1s^{-1}\pi^*$ core-excited state, we made use of the Z+1 approximation, in which the potential of the core-excited sulfur atom is replaced by that of the fully relaxed chlorine atom. The additional electron behaves as an electron promoted to a π^* MO, which splits out from the π^* band after creation of the core hole. To address the $1s^{-1}\sigma^*$ excited state, we modified the initial occupation of the orbitals, by removing the electron from the π^* and occupying the higher-lying split-out σ^* MO localized at the excited ring.

Starting from electronic configurations in the Z+1 approximation corresponding

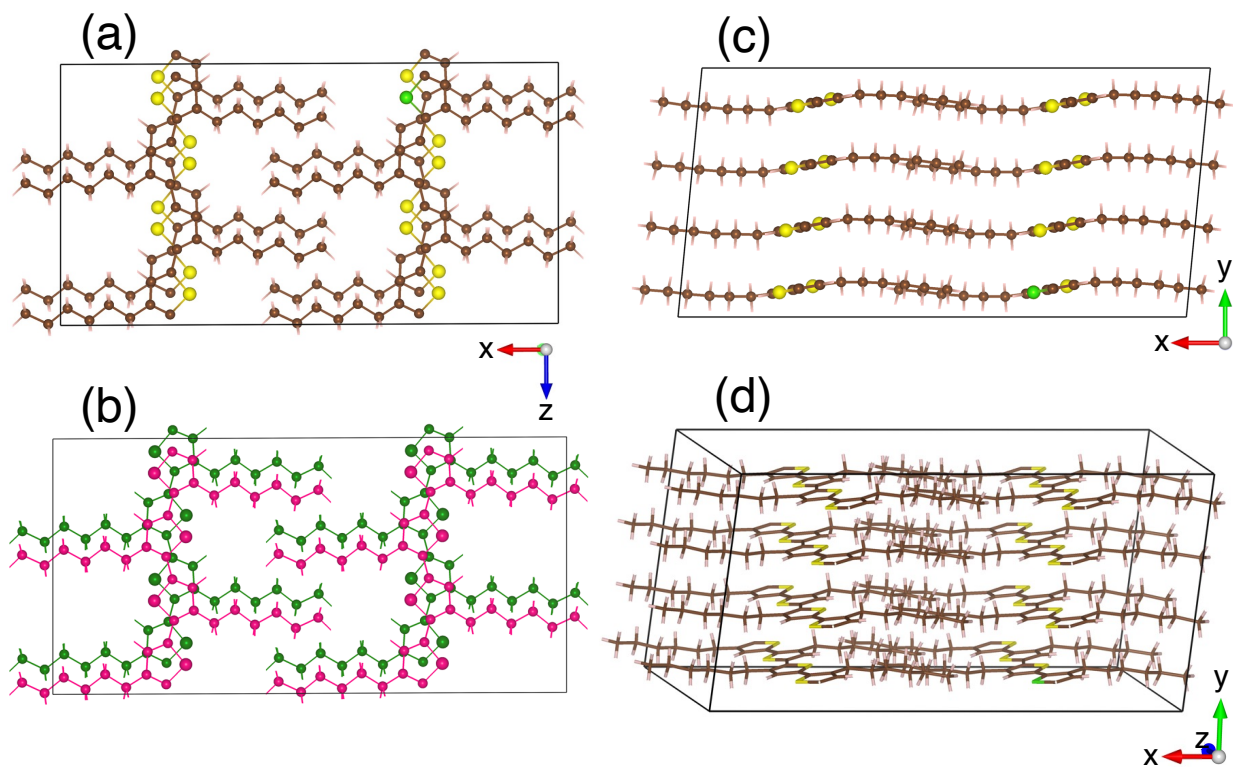


Figure 4.3: Ball and stick illustration of the employed P3HT simulation cell: (a-b) bottom, (c) side, and (d) diagonal views. The XZ plane is parallel to the sample surface. Color code: brown for carbon, yellow for sulfur, green for chlorine (Z+1 approximation), light pink for hydrogen. In panel (b), different polymer layers are depicted in pink and green to show the lateral displacement between the chains when stacked. All the structures' rendering were generated using the VESTA [157] software.

to $1s^{-1}\pi^*$ and $1s^{-1}\sigma^*$ core-excited states, electron dynamics were propagated using the RT-TDDFT [158] approach, in which the electronic wavefunctions are propagated in real-time and are not associated with energy levels. The nuclei were kept at the ground-state optimized coordinates throughout the entire propagation. By means of RT-TDDFT, we are able to address the dynamical rearrangement of the electronic charge, which is taking place within a few femtoseconds upon the formation of the S 1s core hole. Hence, the electronic wavefunctions of the $1s^{-1}\pi^*$ and $1s^{-1}\sigma^*$ states were propagated for 20 femtoseconds, using a time step of 0.5 attoseconds. The evolution of the electronic charge distribution has been monitored by plotting its running changes at time intervals of 5 attoseconds. Moreover, we applied the Bader population analysis to the time dependent charge density [159], to reveal the regions of charge accumulation and charge depletion during the relaxation.

4.4 Results and Discussion

4.4.1 Experimental data analysis

Experimental resonant Auger S $KL_{2,3}L_{2,3}$ spectra for P3HT thin film and PT powder are shown in Fig. 4.4 as 2D maps, where the resonant Auger electron spectra are plotted as a function of both the electron kinetic energy and incident photon energy. The logarithmic color scale represents intensity normalized to the background.

The most intense features in the maps (indicated with white crosses) correspond to the spectator Auger transitions from the first two core-excited states $1s^{-1}\pi_{C-C}^*$ and $1s^{-1}\sigma_{S-C}^*$ to the $2p^{-2}(^1D)\pi_{C-C}^*$ and $2p^{-2}(^1D)\sigma_{S-C}^*$ final states, respectively (labeled as π^* and σ^*). The attribution of the states is based on earlier investigations in thiophene [138]. The white dotted diagonal lines highlight the dependence of the resonant Auger kinetic energy on the photon energy, typically observed in Raman conditions. Horizontal blue lines with adjacent labels (A-D) indicate the corresponding resonant photon energies. The

features indicated with black crosses correspond to the transitions to the $2p^{-2}(^1S)\pi_{C-C}^*$ and $2p^{-2}(^1S)\sigma_{S-C}^*$ final states. The 3P multiplet structures are forbidden due to angular momentum and parity conservation rules and are absent in the figure due to their low intensity.

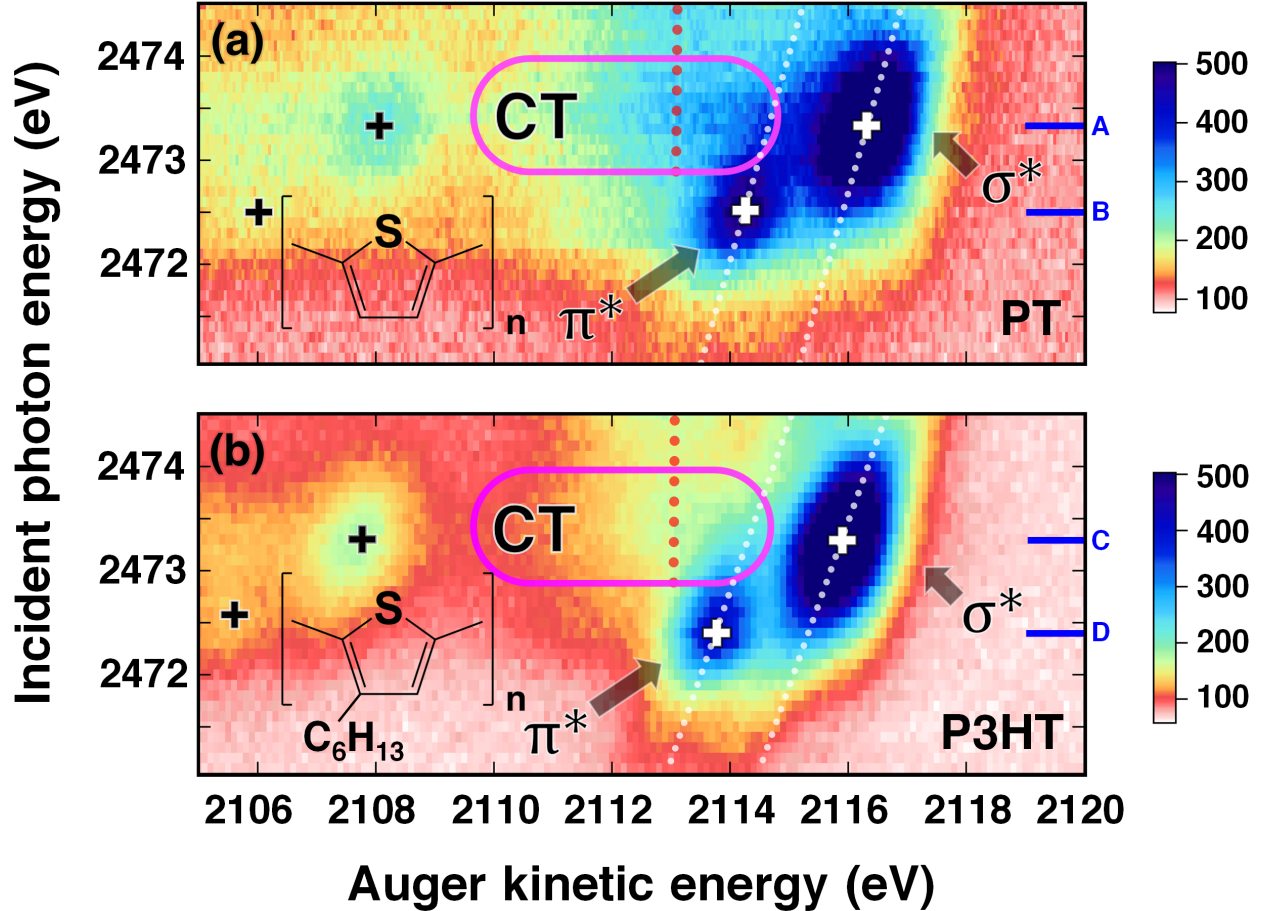


Figure 4.4: 2D maps of S $KL_{2,3}L_{2,3}$ Auger spectra recorded in PT powder (a) and P3HT thin film (b). Transitions to the $2p^{-2}(^1S)\pi_{C-C}^*$ and $2p^{-2}(^1S)\sigma_{S-C}^*$ final states are indicated with black crosses. Transitions to the $2p^{-2}(^1D)\pi_{C-C}^*$ and $2p^{-2}(^1D)\sigma_{S-C}^*$ states, indicated with white crosses, are labeled as π^* and σ^* . Blue lines and adjacent labels (A-D), indicate the corresponding resonant photon energies. Diagonal dotted lines show dispersive behavior of resonant structures. Purple stadium shapes indicate the region where the CT feature is most prominent. Vertical dotted red lines indicate the kinetic energy of the CT channel in the Auger electron spectra. The maps are normalized to the background. The color-coded intensities are on a logarithmic scale.

Both 2D maps contain a feature on the low-energy side of the $2p^{-2}(^1D)\sigma^*$ line, which is marked with purple stadium shapes and labeled CT. The vertical dotted red

lines highlight the constant kinetic energy of the CT feature. At the top of the maps, at the photon energies above 2474 eV, one can see contributions of the Auger lines corresponding to the excitation to high-energy delocalized states. Upon further increase of the photon energy beyond the ionization threshold located at ~ 2478 eV, these features evolve into normal Auger lines [12].

A qualitatively similar manifestation of the CT channel can be observed in both polymers in Fig. 4.4, which likely indicates the similarity of the CT mechanism in the powder and the thin film polymer forms. This goes in contrast to the conclusions of Ref. [52], where the absence of CT in PT powder was probably due to insufficient statistics of the measurements.

Remarkably, in both polymers the CT feature is most intense at the photon energies around ~ 2473.5 eV, i.e. close to the resonant excitation energy of the $1s^{-1}\sigma^*$ state. As introduced above, the blue shift of the spectator Auger electron kinetic energy relative to the normal Auger line allows us to separate the delocalized CT channel from the localized resonant channel at the resonant photon energy. Indeed, at the photon energy of 2473.3 eV, the resonant Auger electrons resulting from the spectator Auger transition to the $2p^{-2}(^1D)\sigma^*$ state have kinetic energy of around 2116 eV. The CT channel, instead, is observed at the kinetic energy around 2113 eV (red dotted line). The 3 eV difference represents the spectator shift caused by the screening of the $1s$ and $2p$ core holes by the spectator electron in the σ^* MO.

The spectator shift reflects the efficiency of screening of the $1s$ and $2p$ core holes by the spectator electron and therefore depends on the energy of the core-excited state with respect to the ground state. Generally, it takes the largest value for the resonant excitation to the lowest unoccupied MO and gradually decreases for higher-lying orbitals converging to zero at the ionization threshold. On the contrary, in our case, the spectator shift of the $2p^{-2}\sigma^*$ line is larger than that of the $2p^{-2}\pi^*$ line. Indeed, the spectator shift corresponding to the $2p^{-2}(^1D)\pi^*$ line, is less than 1 eV at the resonant excitation photon

energy (2472.5 eV) of the $1s^{-1}\pi^*$ state.

This counter-intuitive behavior has been recently observed in gas-phase thiophene [160]. It was demonstrated that in the process of core-excitation and Auger decay, the energy order of the first two core-excited states and the corresponding final states reverses due to the destabilization of the conjugated π -system in the aromatic molecules. The presence of the same effect in gas-phase thiophene and solid-state thiophene-based polymers points at the general nature of the observed phenomenon for conjugated systems.

Using 2D maps as a guide, we can trace the spectator Auger and the CT channels as a function of photon energy with the help of the fitting procedure described in the experimental section. Fig. 4.5 shows least-squares fit analyses of the spectra at the resonant photon energies indicated in Fig. 4.4 by labels A-D and horizontal blue lines.

For both samples, at $\hbar\omega = 2473.3$ eV (Fig. 4.5, panels (a) and (c)) corresponding to the resonant excitation photon energy of the $1s^{-1}\sigma^*$ state, the spectra are dominated by the resonant spectator Auger transition to the $2p^{-2}\sigma^*$ final state at a kinetic energy ~ 2116 eV (magenta). The shoulder on the low-energy side of the dominant line contains the contributions from the resonant spectator transition to the $2p^{-2}\pi^*$ final state (purple) and the CT channel at a kinetic energy ~ 2113 eV (green).

Around $\hbar\omega = 2472.5$ eV (Fig. 4.5, panels (b) and (d)), corresponding to the resonant excitation photon energy of the $1s^{-1}\pi^*$ state, the $2p^{-2}\pi^*$ line at a kinetic energy ~ 2114 eV (purple) is predominant, accompanied by a less intense $2p^{-2}\sigma^*$ line to the higher kinetic energy side (magenta) and a weak shoulder to the low-energy side at a kinetic energy of ~ 2112 eV (orange).

The reason for using different color coding for the green and orange lines in Fig. 4.5 becomes clear when considering dispersion, or kinetic energy position of the spectral features of interest as a function of the incident photon energy presented in Fig. 4.6. It is

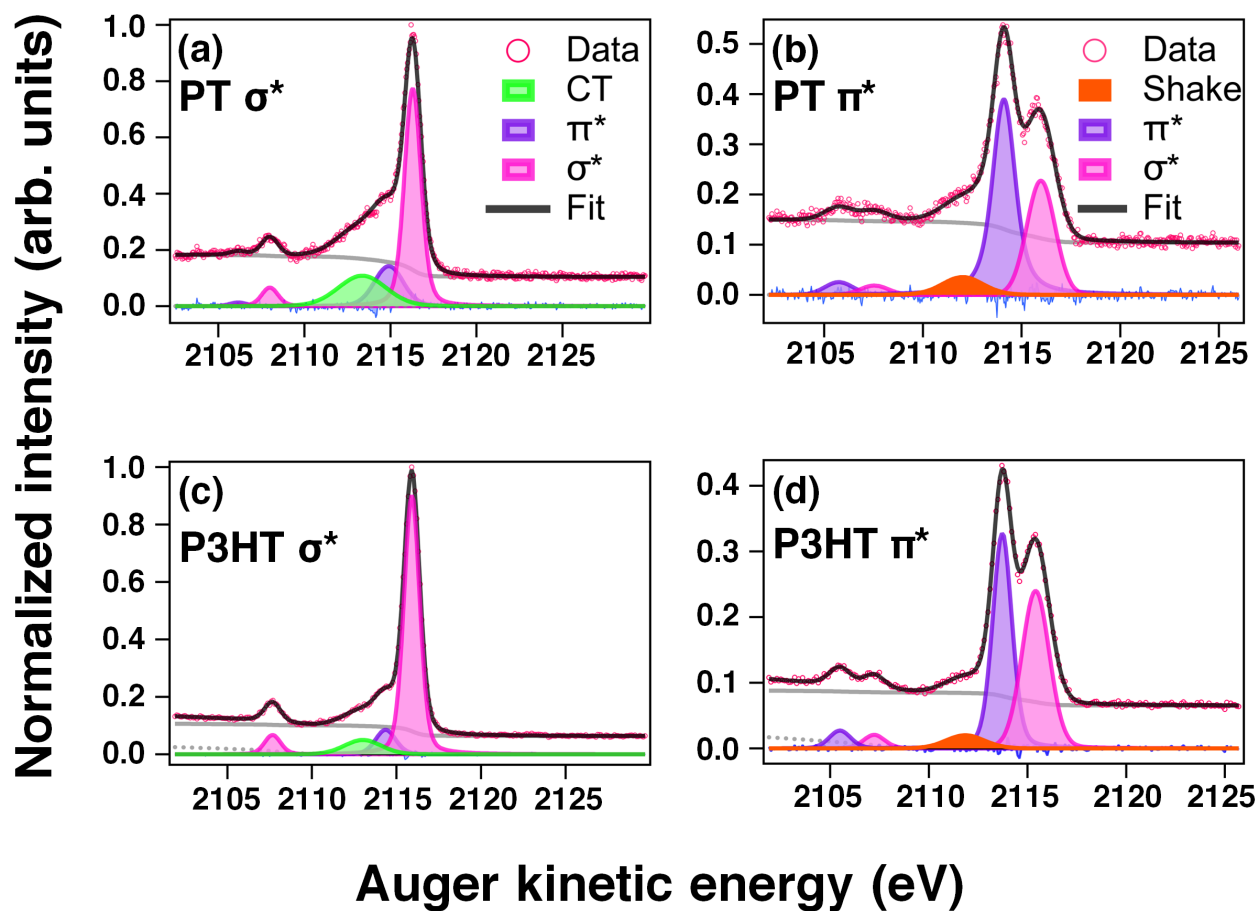


Figure 4.5: $S KL_{2,3}L_{2,3}$ Auger spectra of PT powder (a), (b) and P3HT thin film (c), (d) at resonant excitation energies of the $S 1s^{-1}\sigma^*$ (a), (c) and $S 1s^{-1}\pi^*$ (b), (d) states. The fitted lines correspond to the resonant spectator Auger transitions to the $2p^{-2}\sigma^*$ (magenta) $2p^{-2}\pi^*$ (purple) final states. Green and orange show the CT channel and a shake-up from an occupied band to an unoccupied MO, respectively.

readily apparent that both spectator channels follow a dispersive energy trend in PT (Fig. 4.6(a)) and P3HT (Fig. 4.6(b)).

In contrast to the dispersive resonant spectator channels, the kinetic energy of the Auger electrons ejected as a result of electron delocalization is expected to be independent of the incident photon energy. We use this property as a fingerprint to identify the origin of the peaks observed in the spectra on the low-energy side of the resonant spectator features. In PT and P3HT, at $\hbar\omega \geq 2473$ eV, close to the resonant excitation energy of the $S\ 1s^{-1}\sigma^*$ state, the position of the low-energy peak stays constant, which is the hallmark behavior of electron delocalization. Therefore, we attribute this peak to CT corresponding to electron delocalization from the resonantly excited $1s^{-1}\sigma^*$ state.

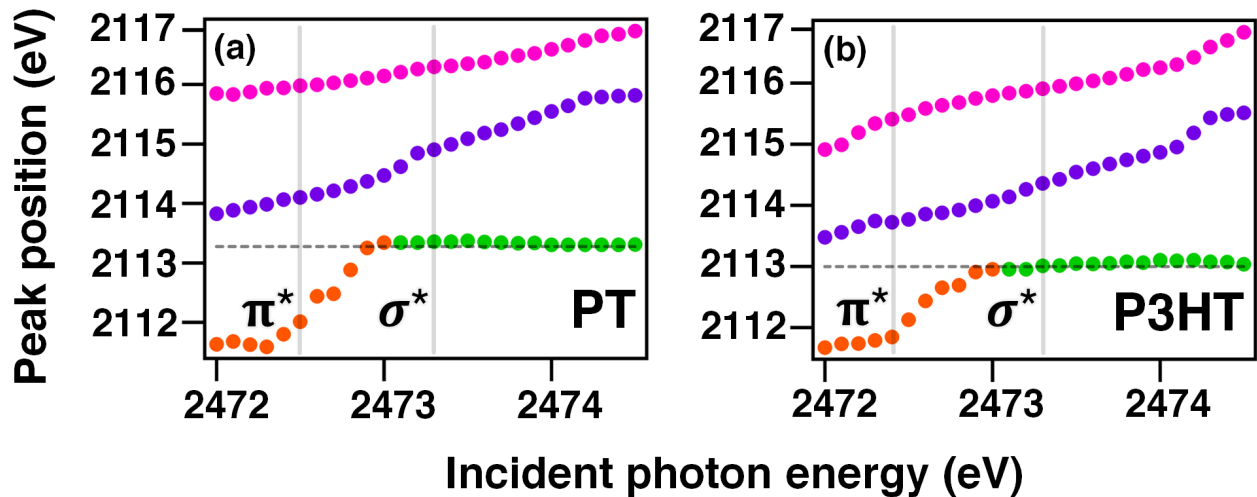


Figure 4.6: Kinetic energy position of Auger electron lines in PT powder (a) and P3HT thin film (b) as a function of photon energy. Grey vertical lines indicate the resonant excitation photon energies for the $1s^{-1}\pi^*$ and $1s^{-1}\sigma^*$ states. Resonant spectator channels $2p^{-2}\sigma^*$ (magenta) and $2p^{-2}\pi^*$ (purple) show a quasi-linear photon energy dependence. Dashed horizontal line highlights the constant kinetic energy of the CT channel (green). Dispersive low-energy peak observed at the photon energies close to the resonant excitation of the $1s^{-1}\pi^*$ state (orange) is attributed to a shake-up process. The systematic error from the fitting procedure is within the size of the marker.

At photon energies $\hbar\omega \leq 2473$ eV, close to the excitation energy of the $S\ 1s^{-1}\pi^*$ resonant state, the kinetic energy of the low-energy peak strongly depends on the photon energy. At these photon energies the intense resonant $2p^{-2}\pi^*$ line strongly overlaps with the weak low-energy peak (see Fig. 4.5, panels (b) and (d)), which reduces fitting accu-

racy. Nevertheless, a clear dependence of the peak kinetic energy on the photon energy, eliminates its possible attribution to the CT process. Its origin may be attributed to shake-up of an electron from an occupied band to an unoccupied MO during the Auger decay as was previously observed in gas-phase systems [161].

According to Eq. (1), from the integrated intensities of the $2p^{-2}\sigma^*$ lines and of the CT lines, resulting from the fits in Fig. 4.5 (a) and (c), we can estimate the CT time τ_{CT} at the resonant excitation energy of the S $1s^{-1}\sigma^*$ state. The obtained τ_{CT} values are ~ 3 femtoseconds and ~ 9 femtoseconds for PT powder and P3HT film, respectively. Note that $\tau_{CT} = 9$ femtoseconds obtained for P3HT film, is comparable with the values reported in earlier studies on PT and P3HT thin films [53, 139, 162]. A three times shorter CT time estimated for PT powder indicates a stronger coupling between the resonantly excited S $1s^{-1}\sigma^*$ state, the source orbital of the CT process, to the conduction band of the polymer, serving as the receiver for the delocalized electron.

4.4.2 Computational analysis

The ultrafast dynamics of the electronic structure induced by the creation of a core hole upon absorption of resonant or non-resonant X-ray radiation, can be simulated by RT-TDDFT. The initial electronic structure of the S $1s^{-1}\pi^*$ and $1s^{-1}\sigma^*$ core-excited states is constructed as described in the Computational methods section. It is worth mentioning that we assume the presence of the core hole only at one thiophene ring in the simulation box. This induces symmetry breaking and the localization of some low-lying empty states around the excited ring, which split out of the corresponding band. Under these conditions, the $1s^{-1}\pi^*$ and $1s^{-1}\sigma^*$ states, occupied by the excited electron, are easily identified as the most localized, but are not necessarily the lowest in energy. Such split-out states are also referred to as core-exciton states in the literature [31].

To illustrate the energy levels of the split-out states with respect to the unoccupied π^* and σ^* bands, Figure 4.7 shows the density of states (DOS) projected on the angular

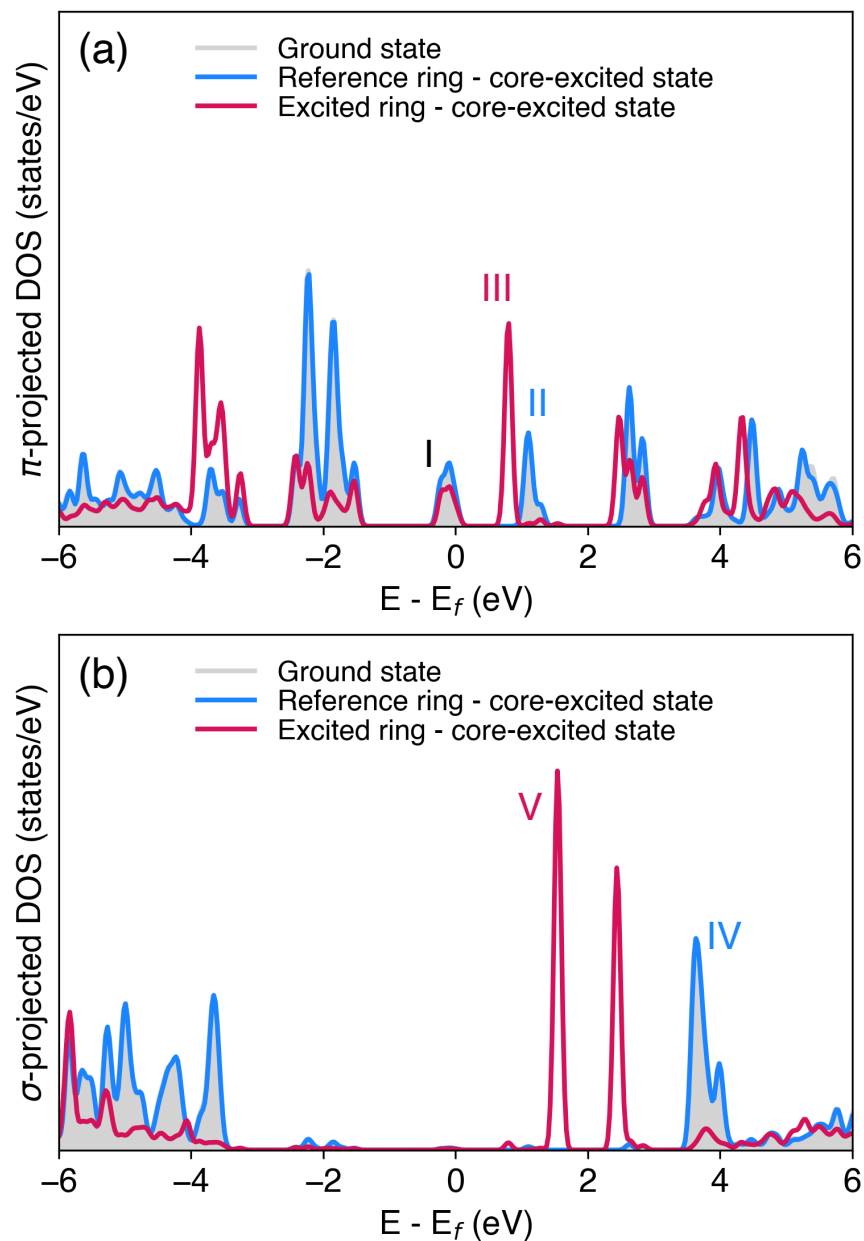


Figure 4.7: DOS computed for P3HT projected on the carbon and sulfur/chlorine atoms of the excited and reference rings, and on the angular momentum components (a) p_y (π -orbital character) and (b) $s+p_x+p_z$ (σ -orbital character). The energy of states is shown relative to the Fermi level. At the reference ring, the projected DOS in the ground state (gray area) and in a core-excited state (blue line) are nearly identical. The Roman numerals label the occupied π band (I), the first unoccupied π^* band (II) and the unoccupied σ^* band (IV). At the excited ring, the projected DOS in a core-excited state (red) contains the split-out π^* MO (III) and the split-out σ^* MO (V).

momentum components p_y (π -orbital character), and $s+p_x+p_z$ (σ -orbital character), and on the carbon and sulfur/chlorine atoms that compose the excited and a reference thiophene rings. The latter was chosen to be the most distant ring from the excited one. Here, we want to emphasize the energy level relaxation around the excited ring. In particular, when the excitation to the π^* band (II in Fig. 4.7 (a)) occurs, the energy of the split-out $1s^{-1}\pi^*$ state (III in Fig. 4.7 (a)) falls below any other unoccupied states. This is not the case for the excitation into the σ^* band (IV in Fig. 4.7 (b)), since despite the relaxation, the split-out $1s^{-1}\sigma^*$ state (V in Fig. 4.7 (b)) still remains above the unoccupied π^* band (II in Fig. 4.7 (a)). This implies a possibility of CT only from the S $1s^{-1}\sigma^*$ state.

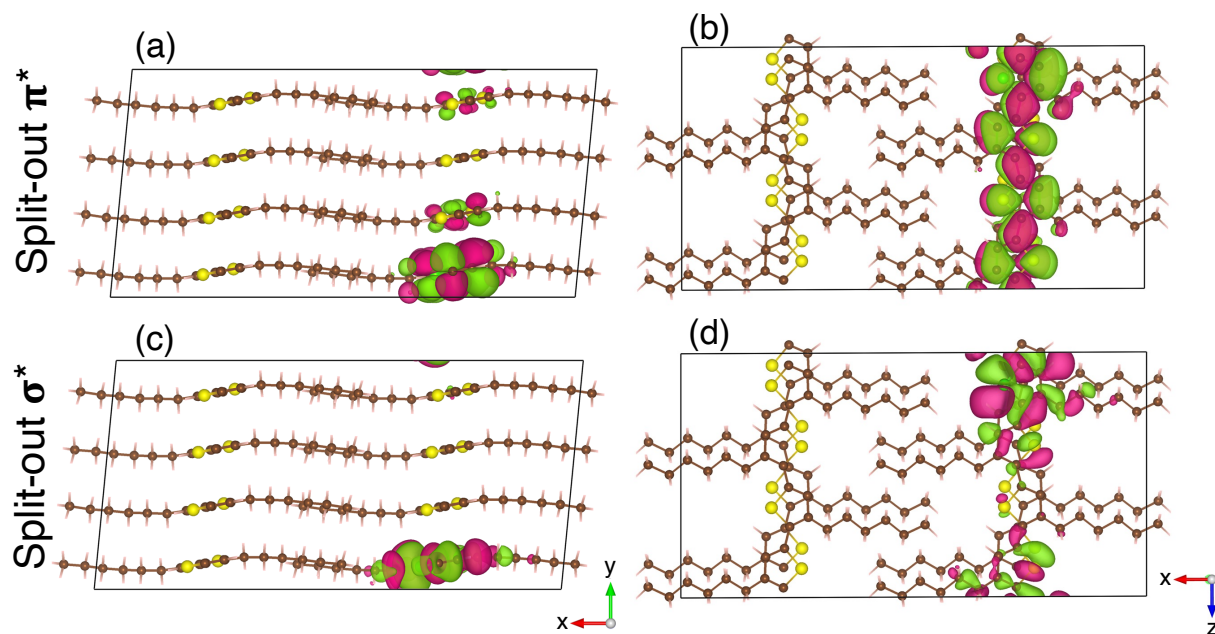


Figure 4.8: XY and XZ views of the spatial distribution of the split-out π^* (a), (b) and σ^* (c), (d) orbitals after creation of the $1s^{-1}\sigma^*$ state in P3HT film. The π^* orbital significantly extends along the polymer chain, whereas the σ^* orbital is spatially localized mainly on the excited thiophene ring. The red and green colored lobes depict the orbital amplitude.

The CT mechanism can be further inferred by considering the spatial distribution of the split-out π^* and σ^* orbitals upon creation of the $1s^{-1}\sigma^*$ core-hole state. The split-out π^* orbital (as well as the orbitals in the unoccupied π^* band) significantly extends along the polymer chain containing the excited thiophene ring, as shown in Figure 4.8 (a)

and (b), whereas the split-out σ^* orbital is localized on the excited thiophene ring only (Fig. 4.8 (c) and (d)). This spatial overlap between the σ^* orbital and the unoccupied π^* band favors the flow of electronic charge along the polymer chains.

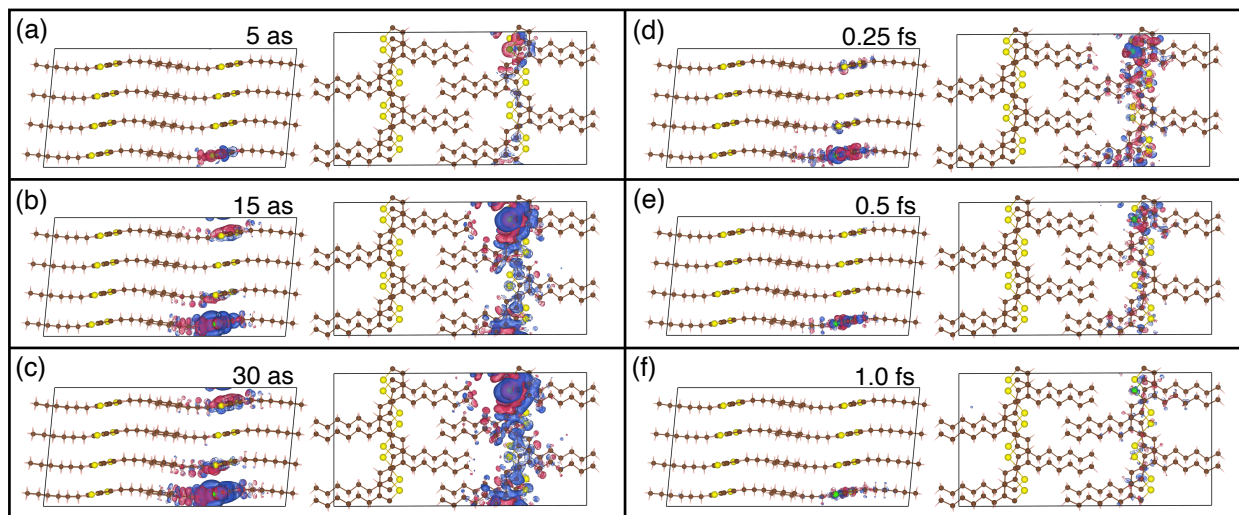


Figure 4.9: Electron density differences in P3HT film computed at time intervals of 5 attoseconds, at (a) 5 attoseconds, (b) 15 attoseconds, (c) 30 attoseconds, (d) 0.25 femtoseconds, (e) 0.5 femtoseconds, and (f) 1 femtosecond of simulation. The electronic dynamics is limited only to the stack of polymer chains containing the excited thiophene ring. Electron accumulation regions are shown in blue, whereas electron depletion regions are shown in red. The surfaces were plotted with an isovalue of $6.0 \times 10^{-5} a_0^{-3}$.

By running the real-time propagation of the electronic density for a few femtoseconds, it is possible to monitor whether and how the electronic distribution around the excited ring evolves. To illustrate the electron dynamics responsible for CT in P3HT film and estimate the timescale of this process, we have plotted the spatial electron density distributions every 5 attoseconds along the first few femtoseconds of propagation. Figure 4.9 (a)-(c) shows the electronic density differences computed at intervals of 5 as, at 5, 15, and 30 as of propagation of the $1s^{-1}\sigma^*$ state. We observe that, already on this timescale, a significant evolution of the electron density occurs in the stack of polymer chains containing the excited thiophene ring. The electron density differences computed at 0.25, 0.5, and 1 femtosecond, shown in Figure 4.9 (d)-(f), demonstrate that the dynamical electronic rearrangement slows down with time, reaching a final state within the first 0.5 femtoseconds of simulation.

One useful tool to extract quantitative information from the electronic distribution is the population analysis performed according to the Bader formalism [159]. In particular, we have calculated the total charge assigned to the excited ring, as well as the population on the neighboring rings along the chain and in the layers above and below the excited ring, as sketched in Fig. 4.10.

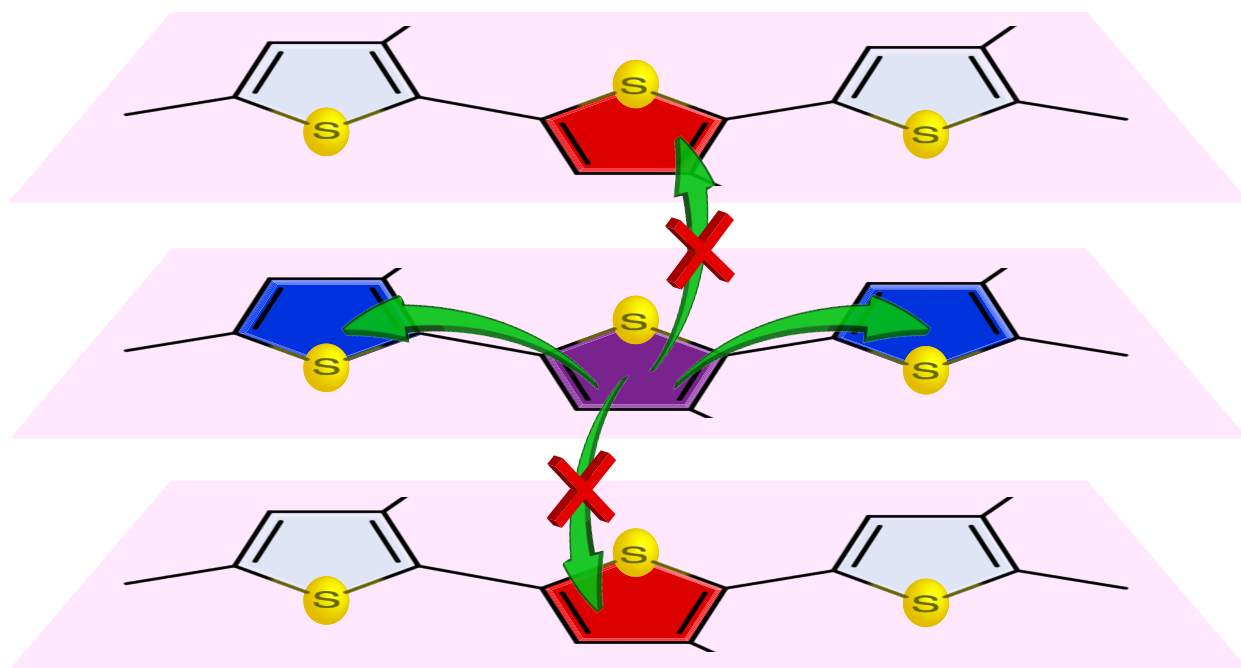


Figure 4.10: Sketch of the excited thiophene ring (purple) and its nearest neighbors along the chain (blue) and in the layers above and below (red) in P3HT film. The green arrows show that only the intra-chain CT is possible.

The variation of the computed populations Δq over the first 3 femtoseconds of the propagation of the $1s^{-1}\pi^*$ and $1s^{-1}\sigma^*$ state are shown in Fig. 4.11 (a) and (b), respectively, with positive (negative) values indicating electron accumulation (depletion). The Bader charge analysis indeed confirms that upon promotion of the core electron to the π^* band, the population of all the selected rings remains unchanged (Fig. 4.11 (a)).

For the $1s^{-1}\sigma^*$ state the situation is different. Upon promotion of the core-excited electron to the σ^* band and propagation of the corresponding electronic wavefunction, we indeed reveal a propensity for charge transfer. The populations of the excited ring

(purple) and of the adjacent rings in the same chain (blue) present a significant change at the very beginning of the propagation, which is then stabilized in less than a femtosecond (Fig. 4.11 (b)). About 0.40 electrons are transferred from the excited ring to the neighbors along the same polymer chain. The variation of population on the rings in the layers above and below the excited ring (red) is negligible.

The timescale of electron delocalization on the order of 1 femtosecond is in agreement with the qualitative analysis provided by the electronic density differences presented in Figure 4.9, and provides an estimate of CT time occurring along the polymer chain in the core-excited $1s^{-1}\sigma^*$ state. This ultrafast timescale compares favorably to the experimental value $\tau_{CT} = 9$ femtoseconds obtained for P3HT film using eq. (1). This variance might be related to the fact, that the simulations cannot fully account for such experimental parameters as possible defects in the crystalline structure of the P3HT film and thermal effects. A possible effect of nuclear motion has been ruled out by the Ehrenfest molecular dynamics simulations, as shown in the following subsection.

Note that in simulations employing real electromagnetic pulses to tackle electronic excitation processes, oscillations in the Bader charges are understood as an effect of the coherent superposition of excited states [163]. In this study, however, the beating pattern present in Figure 4.11 (b) should be rather interpreted as an artifact of the method chosen to create the core-excited state.

Similar results were also obtained for a PT film. The Bader charge analysis performed for the first 2 femtoseconds of real-time propagation, shows no change in population in the selected thiophene rings for the $1s^{-1}\pi^*$ state. On the other hand, for $1s^{-1}\sigma^*$ state, exchange of population can be observed mainly between the excited ring and the adjacent rings along the chain, as shown in Fig. 4.12. The similarity of the results obtained for P3HT and PT show that the hydrocarbon side chains present in P3HT do not appear to modify the mechanism behind the CT processes for this type of polymer films.

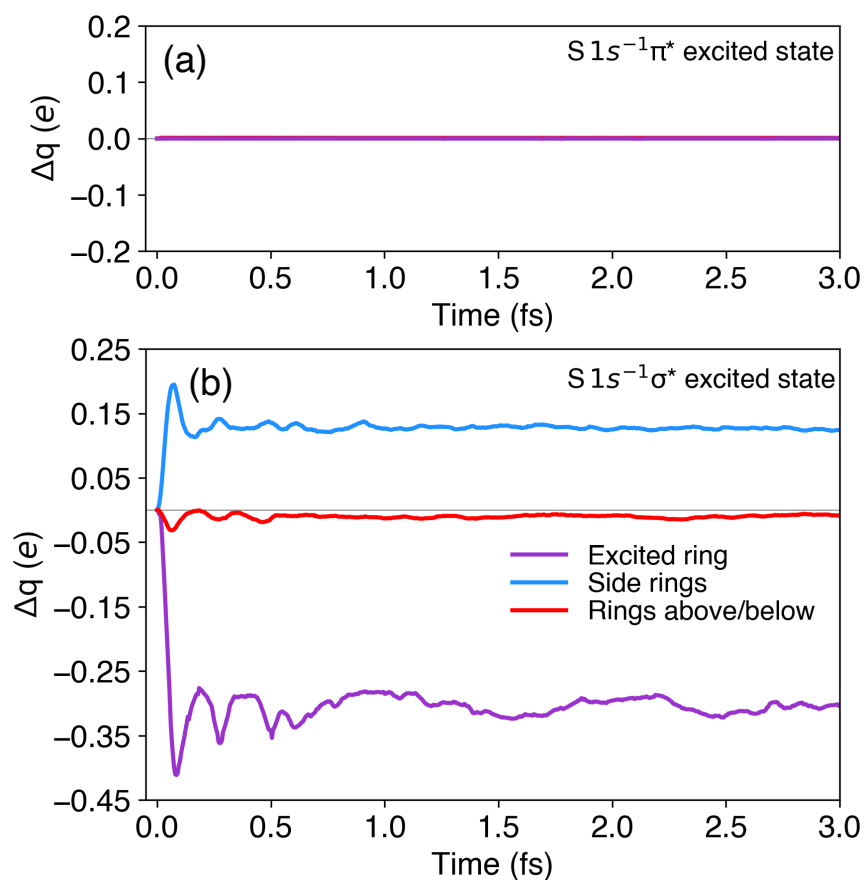


Figure 4.11: Bader charge analysis of the selected rings in P3HT for the first 3 femtoseconds of propagation in the core-excited states (a) $1s^{-1}\pi^*$ and (b) $1s^{-1}\sigma^*$. The gray line denotes $\Delta q = 0$. Negative (positive) values indicate electron depletion (accumulation).

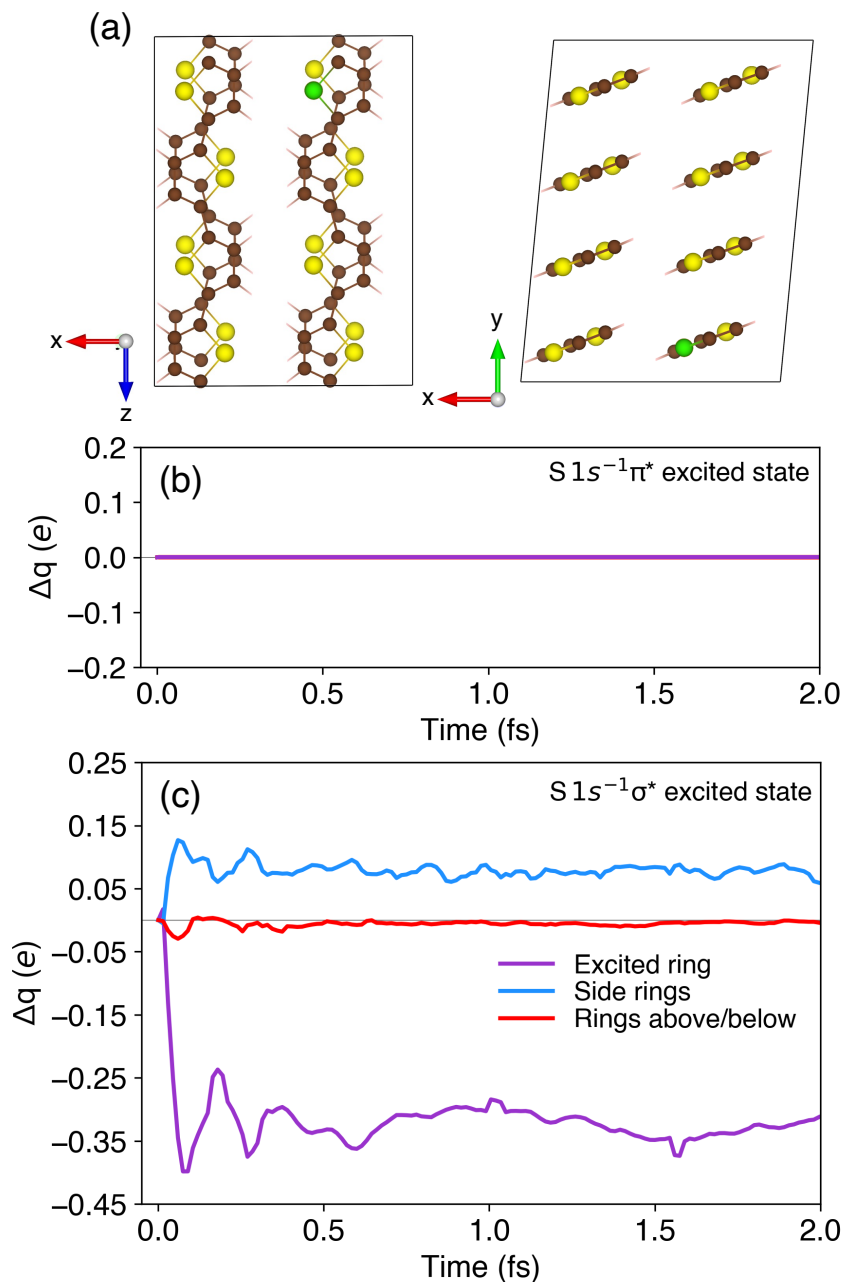


Figure 4.12: (a) Ball and stick representation of PT simulation cell employed in the RT-TDDFT simulations. Color code: brown for carbon, yellow for sulfur, green for chlorine (Z+1 approximation), light pink for hydrogen. (b) and (c) Bader charge analysis in $S 1s^{-1}\pi^*$ and $S 1s^{-1}\sigma^*$ core-excited states for the first 2 femtoseconds of simulation considering the excited thiophene ring and its nearest neighbors. The gray line denotes $\Delta q=0$. Negative (positive) values indicate electron depletion (accumulation).

Ehrenfest molecular dynamics in P3HT

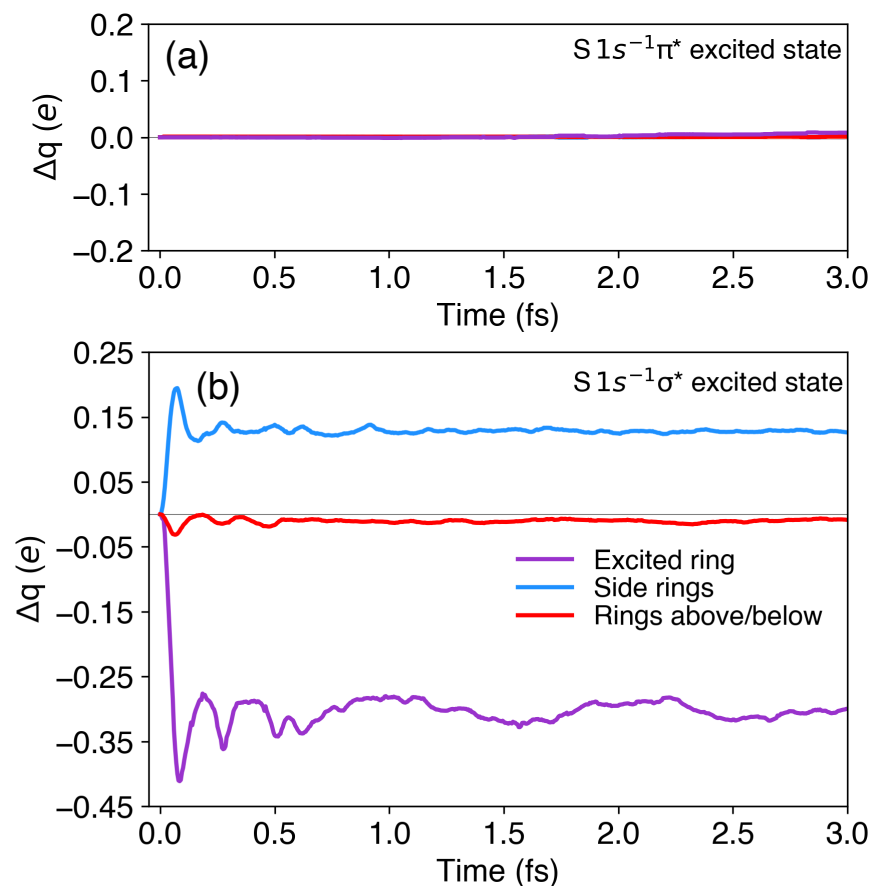


Figure 4.13: Bader charge analysis in P3HT using EMD formalism for the first 3 femtoseconds of simulation considering only the excited thiophene ring and its nearest neighbors for (a) $S 1s^{-1}\pi^*$ and (b) $S 1s^{-1}\sigma^*$ states. The gray line denotes $\Delta q=0$. Negative (positive) values indicate electron depletion (accumulation).

RT-TDDFT simulations can be compared to the Ehrenfest molecular dynamics (EMD) formalism [147,164]. In this case, the electronic wavefunction evolution is coupled to the nuclear motion in a mean-field approach, obtained by averaging over all quantum mechanical states. Bader charge analysis performed for P3HT using EMD for the first 3 femtoseconds of propagation (see Fig. 4.13), shows very similar results to RT-TDDFT simulations presented in Fig. 4.11. Therefore, the choice of neglecting the nuclear motion in the RT-TDDFT approach does not seem to affect the CT process taking place within the first femtoseconds after these specific core-excitations.

4.5 Conclusion

Our joint experimental and theoretical study has demonstrated the presence of ultrafast CT in organic conjugated thiophene-based polymers induced by resonant hard X-ray excitation at the sulfur K-edge. Comparing the experimental evidence of CT in polymer powders and thin films and following the results of real-time propagation TDDFT simulations, we have established that intra-chain electron delocalization is the dominant mechanism of CT, whereas inter-chain electron delocalization is negligible in the studied systems. CT along the polymer chain occurs on the low-femtosecond timescale.

Furthermore, we have shown that intra-chain electron delocalization can be exclusively induced upon resonant excitation of S $1s^{-1}\sigma^*$ state, whereas resonant excitation of the S $1s^{-1}\pi^*$ state does not lead to electron delocalization. Therefore, our approach demonstrates a capacity to not only initialize and monitor ultrafast electron dynamics in extended systems by resonant element-specific core-shell excitation, but also provides a control over electron delocalization by a selective excitation of a specific resonance in the excited atom.

This opens perspectives for the forthcoming studies on intra-molecular conductivity in organic molecules including technologically and biologically relevant systems. A striking resemblance between the polymeric structures containing π -stacked arrays and the DNA double-helical structure with π -stacked arrays of bases implies a manifestation of common mechanisms responsible for electric conduction in these systems. Thus, further investigation of CT in biological samples can provide a better understanding of the mechanisms behind molecular damage induced by X-ray radiation.

The insights into the CT mechanisms in complex systems provided by the CHCS approach owing to its site-specific nature, augmented by the high-level computational analysis, can be taken further towards the field of time-resolved attosecond X-ray spectroscopy promising to bring to light essentially new phenomena in the upcoming years.

Chapter 5

Charge transfer in aqueous L-cysteine

5.1 Introduction

Proteins are essential multifaceted macromolecules present in living organisms, accomplishing vital functions in all aspects of biological processes. Among the many tasks carried by proteins are catalysis, molecular transport, providing structural support, and transmitting neural impulses along nerve cells [165]. Proteins are biopolymers whose monomeric units, or amino acids, constitute the building blocks of proteins. Among proteinogenic amino acids, two stand out due to the incorporation of a sulfur atom in their structure: L-methionine and L-cysteine. L-cysteine has a thiol functional group in a terminal position, compared to L-methionine, which has a methyl group attached to the sulfur. The terminal position of the thiol group confers it reactive properties: L-cysteine can be easily oxidized leading to dimer (cystine) formation, where two cysteine molecules bond through a sulfur bridge. Disulfide bridges impart mechanical stability to proteins, contributing to their three-dimensional structure [166–168]. In addition, L-cysteine has a significant impact on the redox-potential of the cellular environment, and is at the center of the catalytic site in thiol enzymes [169,170]. These, among many other functions, make L-cysteine a model for investigations of amino acids.

Comprehensive studies of amino acids have been carried out using a variety of spectroscopic techniques. Using near-edge X-ray absorption fine structure (NEXAFS) at the S *K*-edge, Jalilehvand et al., observed how the spectrum of L-methionine and L-cysteine, is substantially sensitive to the pH variations of aqueous solutions [92]. Combining S *K*-edge NEXAFS with theoretical tools such as transition-potential density functional theory (TP-DFT), allowed Risberg et al., to compile a library of experimental and theoretical spectra of a variety of sulfur-containing amino acids including L-cysteine in solid form and in aqueous solution at different pH values. In the study, agreement between theory and experiment was significantly improved by incorporation of a hydrogen-bonded water network to simulate hydration in an aqueous solution [58]. An experimental and theoretical effort performed by Sarangi et al., provided a picture of the role that

the coordinated water molecules play in solvated zwitterionic L-cysteine [57], using XAS and time dependent DFT (TD-DFT) simulations. Here it was proposed that the water molecules in the vicinity of the thiol group must first be stabilized in order to contribute as a resonance in the absorption spectrum, likely via hydrogen-bonded water molecules coordinated to the ammonium or carboxylate groups. In this case the water molecules part of the stabilization network will exchange with bulk water molecules, but at much a slower rate than that of the bulk exchange rate [171].

In the soft X-ray regime, a liquid-jet XPS study of L-cysteine in solution measured at several pH, by Carravetta et al., revealed how the chemical shifts of the C 1s, N 1s, and S 2p photolines are almost exclusively dependent on the protonation state of the thiol group [55]. Using XES at the O K-edge, N K-edge, and S L-edge of L-cysteine, Meyer et al., observed dramatic differences in the S $L_{2,3}$ RIXS map when the amino acid is present in zwitterionic form at pH 5 and fully deprotonated at pH 13. While soft X-ray spectroscopic techniques in solution provide an abundance of information about the structural and electronic properties of the molecular ensemble near the surface [172], to probe the bulk of the solution, higher electron kinetic energies are necessary, which are only feasible through hard X-rays.

In chemistry, the network formed by solvent molecules around a solute is key to thermodynamics, solubility, and interactions between solutes [173–176]. While in biochemistry, solvation dynamics of amino acids is crucial to understand structural and energy-related facets of protein-water interactions [177]. Hard X-rays allow us to probe the bulk of the solution, consequently providing a more complete picture of the solvation process and reaction dynamics.

Charge transfer (CT) is essential in biological systems [178], where the vast majority of CT processes occur in aqueous solution. They are indispensable in the flow of electrons taking place in respiration and photosynthesis [179–181]. Radiation damage undergone by biomolecules (e.g. DNA) occurs secondarily through radicals or ions cre-

ated as water is ionized [54], making CT a tool for damage recognition and repair [44,45]. As demonstrated by Céolin et al., and Miteva et al., charge transfer from solvent water molecules to the solute can be observed with XPS and Auger spectroscopy [103,182]. In their study, Auger electron spectra were recorded of a solution of KCl, and it was observed that electrons from the coordinated water molecules were transferred to the K^+ cation. For the solvated Cl^- anion, no CT was observed, likely due to large distance between anion and water molecules, and screening of the Cl^- electron on the Coulomb interaction between vacancies in the anion and vicinal water molecules, possibly hindering the electron transfer process.

The CT process may occur concomitantly upon core-hole creation in ligand-coordinated systems. In solvated clusters, CT has been observed in the form of satellites in XPS spectra, where the energy and intensity of the latter is sensitive to geometrical factors, as well as the type and number of solvent molecules [183–187]. The lifetime of the X-ray induced core-holes can serve as a reference clock through the CHCS method [30,31,43], providing an estimate of the timescales of physical processes, such as CT, occurring during Auger decay.

Considering the above discussed, investigating the electronic structure and dynamical processes occurring in solvated systems is of paramount interest. With this in mind, the aim of this study is to explore how the CT process depends on protonation state of solvated L-cysteine. By employing the CHCS method, our experimental results reveal that upon resonant excitation at the S *K*-edge, CT is effected, and observed at pH 12. Moreover, upon core-ionization, a hint of CT is observed to occur in L-cysteine at all pH values.

Theoretical calculations, using TP-DFT and molecular dynamics (MD) simulations, provide a preliminary picture which indicates CT upon core-ionization. Furthermore, theoretical analysis indicates that the hydration shell around the sulfur atom likely plays an important role in the CT process.

5.2 Experiment

The measurements were performed at the SOLEIL French national synchrotron facility on the high-resolution station for hard x-ray photoemission spectroscopy HAXPES [69] located at the GALAXIES beamline [67]. Linearly polarized light was provided by a U20 undulator followed by a Si(111) double-crystal monochromator. Emitted electrons were recorded by a EW4000 Scienta hemispherical analyzer, whose lens axis was parallel to the polarization vector of the beam. A 200 eV pass energy, and a 0.3 mm width curved slit were used during recording. The spectrometer resolution was determined at ~ 180 meV while the beamline photon bandwidth δE was ~ 225 meV at 2.5 keV, and ~ 380 meV at 3.5 keV photon energy.

Experiments were carried out on a setup dedicated to liquid phase measurements [67, 69]. The solution is injected via a HPLC pump and a 30 μm glass capillary aligned to a catcher where the waste is extracted from the vacuum chamber. Both capillary and catcher are located in a differentially pumped tube. The liquid jet, flowing at ~ 1 mL / min, is perpendicular to the X-ray propagation axis and to the spectrometer lens axis. L-cysteine BioReagent, was purchased from Sigma-Aldrich, and dissolved in ultrapure MilliporeTM water to a concentration of 0.5 M. This concentration was a compromise between good signal-to-noise ratio and avoiding concentration effects, as L-cysteine oxidizes and forms disulfide bridge bonds to form cystine, which is poorly soluble in water, leading to production of a white precipitate. The pH was adjusted with a Mettler Toledo pH/Ion meter (accuracy of ± 0.002) by adding HCl or NaOH to the filtered solutions until final pH values were obtained corresponding to 1.16, 5.17, 9.56, and 12.6.

For the 2D maps presented in Fig. 5.5, S *KLL* Auger spectra of aqueous L-cysteine were recorded at incident photon energies ranging from ~ 2466 - 2484 eV, with a photon energy step of 200 meV, covering the resonant region around the S *K*-edge. In addition, several spectra were measured at photon energies covering up to ~ 1 keV above absorption edge. The incident photon energy was calibrated by using S *K*-edge absorption spec-

tra of solvated L-cysteine measured at pH values closely matching those presented in this study from Ref. [58], measured in fluorescence yield mode. In condensed phase samples, the kinetic energy of the Auger and photoelectrons recorded by the analyzer is modified by the spectrometer work function ϕ_{SP} [86]. We have used the Au $4f_{7/2}$ photo line to obtain $\phi_{SP} = 4.90(1)$ eV. In all spectra presented, the electron kinetic energies referenced to the FL are shifted by the latter amount toward higher values with respect to the kinetic energies measured by the spectrometer. This procedure was carried out as both spectrometer and liquid jet were grounded, and the concentration of ions in solution was assumed sufficient to make it conductive. While a more accurate and robust calibration approach is highly desirable [87, 188], it was not feasible during the limited time of the experiment.

It was observed that for a few Auger and photoelectron spectra, a shift in kinetic energy was present. The injection chain was cleaned with deionized water between measurements, and while the samples had been prepared immediately prior to measuring, it is possible that residue began nucleating on the surface of the capillary/catcher, possibly leading to electrokinetic charging effects manifested as shifts in Auger kinetic energy [87, 189–191]. This effect was only observed in measurements of individual spectra, and not on the 2D maps. In the following, individual Auger spectra are presented on a relative scale, indicated on respective Figs.

To extract information from the Auger spectra, the SPANCF fitting suite for Igor Pro [81] was employed. For all spectra, Voigt profiles were used, where both Lorentzian and Gaussian components were set as free parameters. Where necessary, two Shirley backgrounds were used during the fit, to accurately account for the increased intensity at lower kinetic energies caused by inelastically scattered electrons.

5.3 Theory

5.3.1 Core-hole clock spectroscopy

The principle of the CHCS method, utilized to interpret CT upon core-excitation (Section 5.4), is outlined in detail in Chapter 1. In principle, the branching ratio between the localized spectator Auger and delocalized CT channels, provides an estimate of the CT rate upon core-excitation. To determine the timescale of CT (τ_{CT}), the following relation can be employed [30,31,46]

$$\tau_{CT} = \tau_{CH} * \frac{I_{Spectator}}{I_{CT}}, \quad (5.1)$$

where $I_{Spectator}$ and I_{CT} correspond to the integrated intensity of a specific resonant spectator Auger channel and the CT channel, respectively, and $\tau_{CH} = 1.1$ fs is the S 1s core-hole lifetime [47].

5.3.2 Computational methods

X-ray absorption spectroscopy (XAS) calculations were carried out using the CP2K program [154]. Electronic transitions were described by TP-DFT using the BLYP exchange-correlation functional [192, 193] with Grimme’s D3 dispersion correction [153]. Simulations were performed under the Gaussian and Augmented and plane-wave (GAPW) approach [194]. A 6-311++G2d2p Pople style basis set was employed for all atom types with a cutoff of 300 Ry for the auxiliary plane-wave basis set.

These XAS calculations were used to simulate a core-excited state (CES) in which an electron is promoted to an unoccupied molecular orbital using a half core-hole potential approach (HCH). The HCH approximation (standard TP-DFT [195]) has been used successfully to simulate X-ray scattering in liquid water [196], and XAS spectra of surface

and bulk ice [197]. Core-ionized states (CIS) were calculated using the same approach, where the mono-cationic state is simulated by changing the charge of the simulated system. Both core-excited and core-ionized simulations were performed using the Z+1 approximation, in which the potential of the core-excited or core-ionized sulfur atom is replaced by that of the fully relaxed chlorine atom.



Figure 5.1: Ball-and-stick illustration of optimized L-cysteine structure with two water molecules coordinated to the thiol group. Sulfur atom in yellow, oxygen atoms in red, hydrogen atoms in white, nitrogen atom in blue, and carbon atoms in black.

The model used for ground state (GS) XAS calculations was based on Ref. [57]. Both CES and CIS calculations were performed upon the GS model, in which the thiol group of zwitterionic L-cysteine is coordinated to two water molecules. The GS model was subsequently optimized under the Gaussian plane-wave method (GPW) [198] using Goedecker – Teter – Hutter (GTH) pseudopotentials [155], and triple-zeta valence plus polarization (TZVP) basis sets, with a cutoff of 300 Ry for the auxiliary plane-wave basis set. The resulting optimized model is presented in Fig. 5.1.

Both classical molecular dynamics (MD) and ab initio molecular dynamics (AIMD) simulations were performed on solvated L-cysteine with a network of 100 water molecules. These simulations were carried out to assess the importance of the solvation network around the core-excited / core-ionized sulfur atom. Analysis of the pair distribution function $g(r)$ allows for the determination of the number of solvation shells that play an active role in the water network coordinated to the sulfur atom and

functional groups.

MD simulations were performed for the solvated supercell of zwitterionic L-cysteine with 100 water molecules in periodic boundary conditions using CP2K. Two separate simulations were performed using the canonical (NVT) and isothermal-isobaric (NpT) ensembles at ambient conditions with a four chain Nosé-Hoover thermostat and a coupling time constant of 20 fs [199]. This procedure was carried out to ensure preservation of the system cell parameters [200]. MD simulations were performed on a simulation cell of volume 14.7246 \AA^3 , for 1 ns with a 0.5 fs step, where the system was deemed to have reached equilibrium.

AIMD simulations for the equilibrated solvated supercell were performed using CP2K. Simulations in the microcanonical (NVE) ensemble were performed at ambient conditions, for 6 picoseconds with a 0.5 femtoseconds step, using a simulation cell of volume 14.7246 \AA^3 . Forces for the dynamics were obtained using DFT-based electronic structure calculations, with the BLYP exchange-correlation functional and Grimme's D3 van der Waals correction. The GPW method was used with a cutoff of 500 Ry in combination with GTH pseudopotentials. Employed basis sets used were TZVP-MOLOPT-GTH for all atoms.

5.4 Results and Discussion

Experimental X-ray absorption-like partial electron yield (PEY) spectra for sulfur *K*-edge are presented in Fig. 5.2. Spectra were obtained by integrating the intensity of the 2D maps over the Auger kinetic energy. At all pH values measured, the PEY spectra are in good agreement with XAS spectra obtained by Risberg et al. in Ref. [58].

XAS spectra obtained by Risberg et al., are presented in Fig. 5.3, where L-cysteine solutions were measured at different pH values. Here, we present spectra from their experiment at pH 0 (a), 4.94 (b), 9.4 (c), and 13 (d). These pH values are close to those of

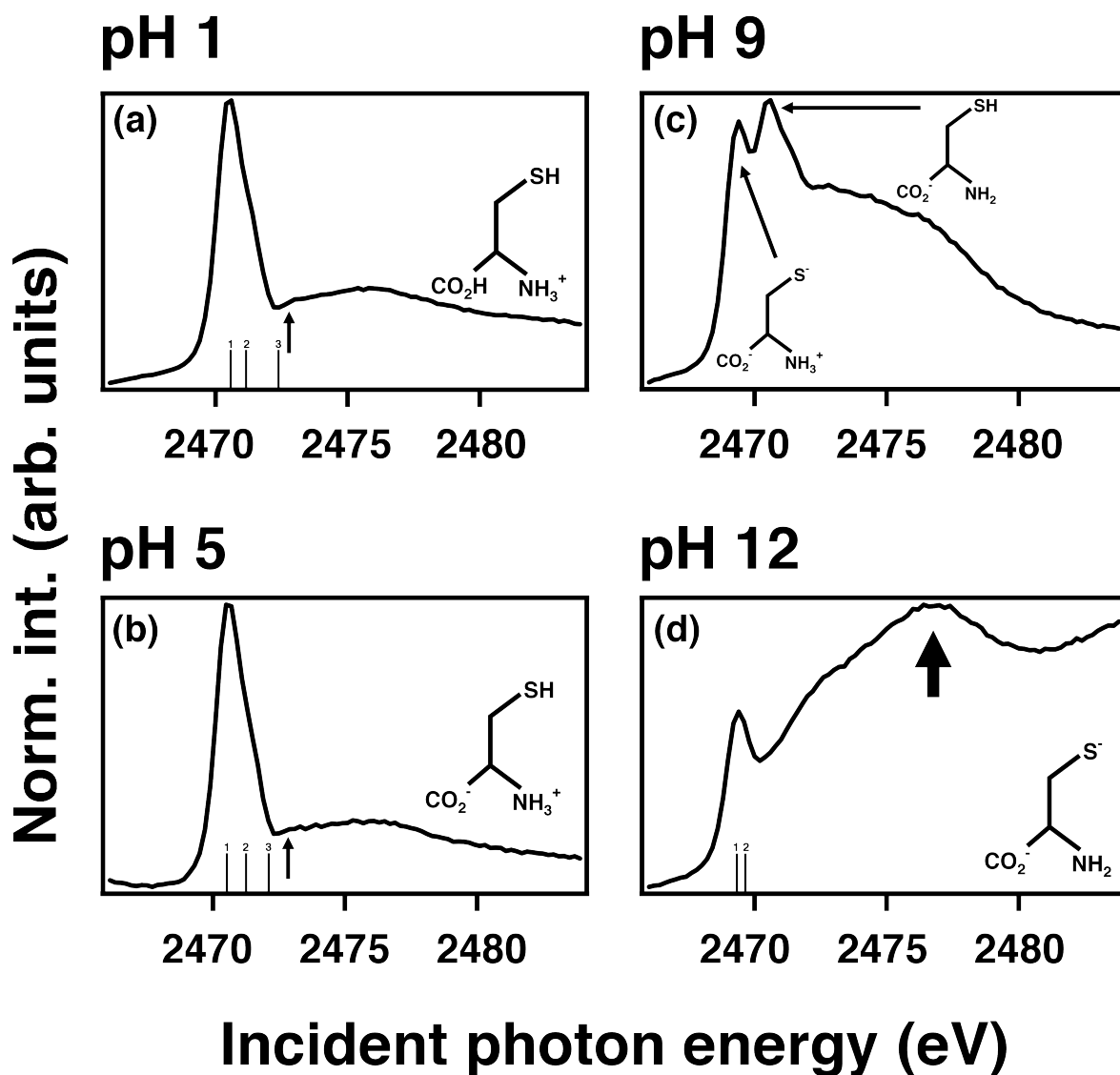


Figure 5.2: PEY spectra of L-cysteine at pH 1 (a), pH 5 (b), pH 9 (c), pH 12 (d). Schematic structure in each panel corresponds to the protonated states at each pH: (a) pH 1, fully protonated; (b) pH 5, zwitterionic; (c) pH 9, mixture of two isomeric forms; (d) pH 12, fully deprotonated. Short arrows in (a) and (b) indicate a shoulder present at both pH 1 and pH 5. In (c) at pH 9, long arrows indicate the resonant peaks originating from each fractional component of the mixture. In (d) at pH 12, thick arrow indicates shape resonance-like feature. Transitions in (a), (b), and (d), from Table 5.2, and same as in Fig. 5.3, as calculated by Risberg et al.

the aqueous solutions measured in our experiment, where L-cysteine was measured at pH values 1.16, 5.17, 9.56, and 12.6. In the following, these pH values will be referred to as 1, 5, 9, and 12, for simplicity. In Table 5.1 is presented a summary of the pH values at which XAS spectra were obtained by Risberg et al., and those pertaining to this experiment. In Table 5.2 are presented the transitions calculated by Risberg et al., their character, and calculated photon energies when L-cysteine is fully protonated (pH 0), in zwitterionic form (pH 4.94), and fully deprotonated (pH 13). Calculated transitions are also presented in Fig. 5.3.

Table 5.1: pH values at which Auger spectra in this work were measured, and pH values at which XAS spectra were obtained from Risberg et al. [58].

pH this work	pH this work simplified	pH Risberg et al.
1.16	1	0
5.17	5	4.94
9.56	9	9.4
12.6	12	13

Table 5.2: Assigned transitions, character and corresponding incident photon energies from XAS calculations. Ref. [58].

Transition	pH 0		pH 4.94		pH 13	
	Character	Energy (eV)	Character	Energy (eV)	Character	Energy (eV)
1	$\sigma_{(S-H)}^*$	2470.6	$\sigma_{(S-H)}^*$	2470.5	$\sigma_{(S-C)}^* CT$	2469.3
	$\sigma_{(S-C)}^*$					
2	$\pi_{(COOH)}^*$	2471.2	$\sigma_{(S-C)}^*$	2471.3	$\sigma_{(S-C)}^* CT$	2469.6
	$\sigma_{(S-C)}^*$					
	$\sigma_{(S-H)}^*$					
3	$\sigma_{(S-C)}^*$	2472.4	$\sigma_{(S-H)}^*$	2472.1	Not available	
	$\pi_{(COOH)}^*$		$\sigma_{(O-H)}^*$			

As seen in Table 5.2, at pH 0 and 4.94, according to the assignment by Risberg et al., the XAS contains three main transitions. The first one has strong $\sigma_{(S-H)}^*$ character for both pH 0 and 4.94. At pH 0, however, this transition also has a weak $\sigma_{(S-C)}^*$ contribution.

At pH 0, the second transition has $\sigma_{(S-C)}^*$, $\sigma_{(S-H)}^*$, and $\pi_{(COOH)}^*$ character. The latter character is due to contributions from a delocalized orbital. This appears to be a solvation effect upon hydration of the molecule, not present in their calculations of

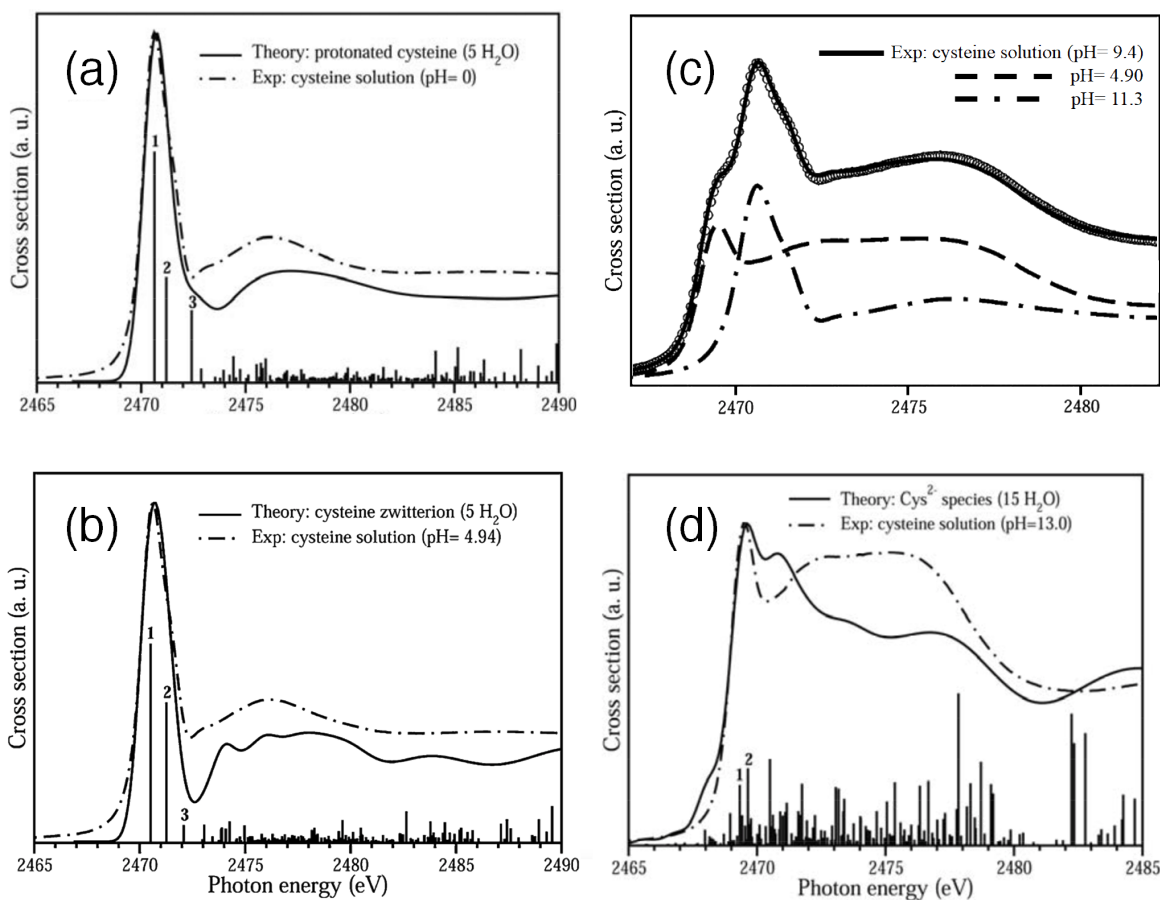


Figure 5.3: XAS spectra of L-cysteine obtained by Risberg et al., at pH 0 (a), pH 4.94 (b), pH 9.4 (c), pH 13 (d). No calculations are available for (b), the circles correspond to a linear combination of two experimental spectra at pH 4.90 and 11.3, where the contribution of the thiolate form corresponds to 59%. Adapted from Ref. [58].

gas-phase L-cysteine. Upon hydration, hydrogen bonds to the carboxyl group have an electron-withdrawing effect leading to redistribution of electron density. This hydrogen bonding effect is not present in the second transition at pH 4.94, which is purely of $\sigma_{(S-C)}^*$ character. One possible reason for the different character of the transition at different pH is due to the lack of electron-withdrawing effect at pH 5.

At both pH 0 and pH 4.94, a third transition was calculated. For pH 0, it has $\sigma_{(S-C)}^*$ and partial $\pi_{(COOH)}^*$ character. For pH 4.94, this third transition has $\sigma_{(S-H)}^*$ character with considerable $\sigma_{(O-H)}^*$ character, originating from the hydrogen bonding to the thiol group from water molecules. The difference of character possibly originates from the carboxyl group, which in the protonated state has two closely coordinated water molecules, while in the zwitterionic state there is only one closely coordinated water molecule, as shown in Fig. 5.4.

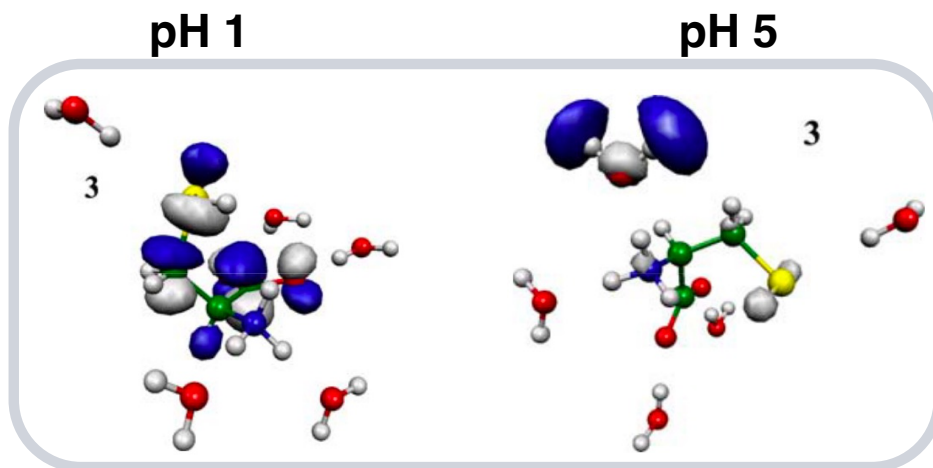


Figure 5.4: Electron density contours of the MOs corresponding to transition 3, as assigned by Risberg et al. in Table 5.2. pH 1 and pH 5 correspond to pH 0 and pH 4.94 in Ref. [58].

At pH 9.4 theoretical calculations are not available. However, at this pH value a linear combination procedure carried out on XAS spectra of the zwitterionic and thiolate forms of L-cysteine, which is in good agreement with the fractional components shown in the titration curve obtained by Dixon et al. [201]

At pH 13, calculations indicate the presence of two transitions, both of which have $\sigma_{(S-C)}^*$ and CT character towards the water molecules in the surroundings. Interestingly, the second transition only appears in their solvated model of L-cysteine (which includes 15 coordinated water molecules, compared to 5 water molecules at pH 0 and 4.94), and is absent in their gas phase model calculations [58].

In our PEY spectra, presented in Fig.5.2, one can recognize all main features obtained by Risberg et al., shown in Fig. 5.3. In Fig.5.2 (a, b), at pH 1 and 5, respectively, the PEY spectra are remarkably similar, both displaying an intense peak at ~ 2470.6 eV. Based on the titration curves for cysteine in aqueous solution from Dixon et al., in Ref. [201], at pH 1, L-cysteine is fully protonated, while at pH 5, the carboxyl group is deprotonated leading to the zwitterionic form of the amino acid. At both pH 1 and 5, the thiol group remains protonated. In Fig. 5.2, at pH 1 (a) and 5 (b), at a photon energy of ~ 2472.8 eV, a feature is present, indicated by a short arrow, which corresponds to transition 3 in Table 5.2. At pH 9 (c), two long arrows indicate the different forms of L-cysteine present at this pH, where a mix of two isomeric forms coexist in solution, corresponding to $S^-CH_2CH(NH_3^+)COO^-$, and $HSCH_2CH(NH_2)COO^-$. At pH 9, ours contain a distinct double-peak structure at ~ 2469.4 eV, and ~ 2470.6 eV, which is not resolved in the spectra by Risberg et al., measured at pH 9.4. This likely has an origin in the lifetime broadening of core-excited states, restricting the spectral resolution in XAS experiments. This restriction may be bypassed in PEY measurements obtained with Auger spectroscopy [202]. A fitting procedure performed in our PEY spectra yields a predominant thiolate contribution of 60% at pH 9, in agreement with the linear combination procedure of Risberg.

At pH 12, a broad feature, indicated by a thick arrow, can be observed within the ~ 2473 - 2480 eV photon energy range, feature which can also be seen in the spectra measured by Risberg et al., shown in Fig. 5.3 at pH 13 (d). Such a broad peak appears to be a recurring feature in *K*- and *L*-edge XAS spectra of negatively charged sulfur-containing compounds [92, 203]. The broad features become less prominent when the sulfur-containing system becomes more oxidized. When the photoelectron undergoes

multiple scattering within the first and second shell of the surrounding atoms, the absorption spectrum may display complex structural features known as shape resonances [204]. One possible explanation for the origin of the shape resonance in our spectra is the multiple scattering of the photoelectron from the proximate water molecules part of the solvation shells around L-cysteine, as explained in Section 5.5.

Experimental resonant Auger S *KLL* spectra for L-cysteine measured at pH 1, 5, 9, and 12, are shown in Fig. 5.5 as 2D maps, where resonant Auger electron spectra are plotted both as a function of the incident photon energy and the electron kinetic energy. The logarithmic color scale represents intensity of the maps normalized to the background.

At the incident photon energy of ~ 2470.6 eV, the 2D maps for pH 1 (a) and pH 5 (b) contain spectator Auger transitions from the core-excited $1s^{-1}V$ to $2p^{-2}(^1S)V$ (white cross) and $2p^{-2}(^1D)V$ (black cross) final states, where V corresponds to the molecular orbital containing spectator electron. The white dotted diagonal lines highlight the dependence of the resonant Auger kinetic energy on the incident photon energy, behavior which is typically observed in Raman conditions. The 3P multiplet structures are forbidden due to angular momentum and parity conservation rules and are absent in the 2D maps due to low intensity.

It is not possible to resolve the individual calculated transitions, numbered 1 and 2 in Table 5.2 within the resonant structures indicated by the black and white crosses in our resonant Auger spectra at either pH 1, and pH 5. However, it is visible that the resonant structures are quite complex and contain an overlap of more than one transition. At slightly higher photon energies, at ~ 2472.8 eV, there is a resonant structure indicated by an orange cross, present at both pH 1 (a) and 5 (b). This corresponds to a transition from the core-excited $1s^{-1}V$ to $2p^{-2}(^1D)V$ final state, where V is the molecular orbital assigned in Table 5.2 for the absorption transition number 3. It can be observed that at pH 1, the Auger kinetic energy of the spectral features are blueshifted by ~ 3 eV with respect to those observed at pH 5. A possible explanation for this lies in the experimental

conditions (namely the instability of the liquid-jet), which may have changed during the course of the experiment, subsequently leading to unexpected shifts in the kinetic energy of the Auger electron lines.

At pH 9 in Fig. 5.5 (c), the 2D map is quite feature-rich and contains resonant structures indicated with black and white crosses. It is possible to attribute most of the features to a mixture of two isomeric forms coexisting in the aqueous solution of L-cysteine, corresponding to $S^-CH_2CH(NH_3^+)COO^-$, and $HSCH_2CH(NH_2)COO^-$, as with the case of XAS spectra. It may be observed that while the kinetic energies of the spectral features in the thiolate ($S^-CH_2CH(NH_3^+)COO^-$) form are roughly similar to those found at pH 12, those of the thiol ($HSCH_2CH(NH_2)COO^-$) form, are close to the kinetic energies of the spectral features of the fully protonated form at pH 1. As previously mentioned, this likely has a root in the -at times- unstable experimental conditions, possibly causing a shift of the Auger electron lines.

At pH 12, when the fully deprotonated form dominates, two resonant structures can be observed, around the photon energy of ~ 2469.4 eV, corresponding to transitions 1 or 2 in Table 5.2, and to spectator Auger transitions from the core-excited $1s^{-1}V$ to $2p^{-2}(^1S)V$ (white cross) and $2p^{-2}(^1D)V$ (black cross) final states. At this pH, the molecular orbitals V occupied by the spectator electron have the same mixed CT character as indicated in Table 5.2. Another, weaker, resonant feature can be seen at slightly higher photon energy at ~ 2470.7 eV, indicated by an orange cross, which is present in the calculated spectrum shown in Fig. 5.3 (d), but has not been assigned. It is not unlikely that this resonant structure has a similar delocalized character as those found at pH 1 and 5: it is energetically close to the NA line, as shown in Fig. 5.5 (d), as with the case of pH 1 and pH 5, (a) and (b), respectively. The latter would consequently render this feature as being independent of pH, and perhaps contributing to the CT process observed. Encircled within red dotted line is a feature attributed to resonant electron delocalization, which will be discussed in the next subsection.

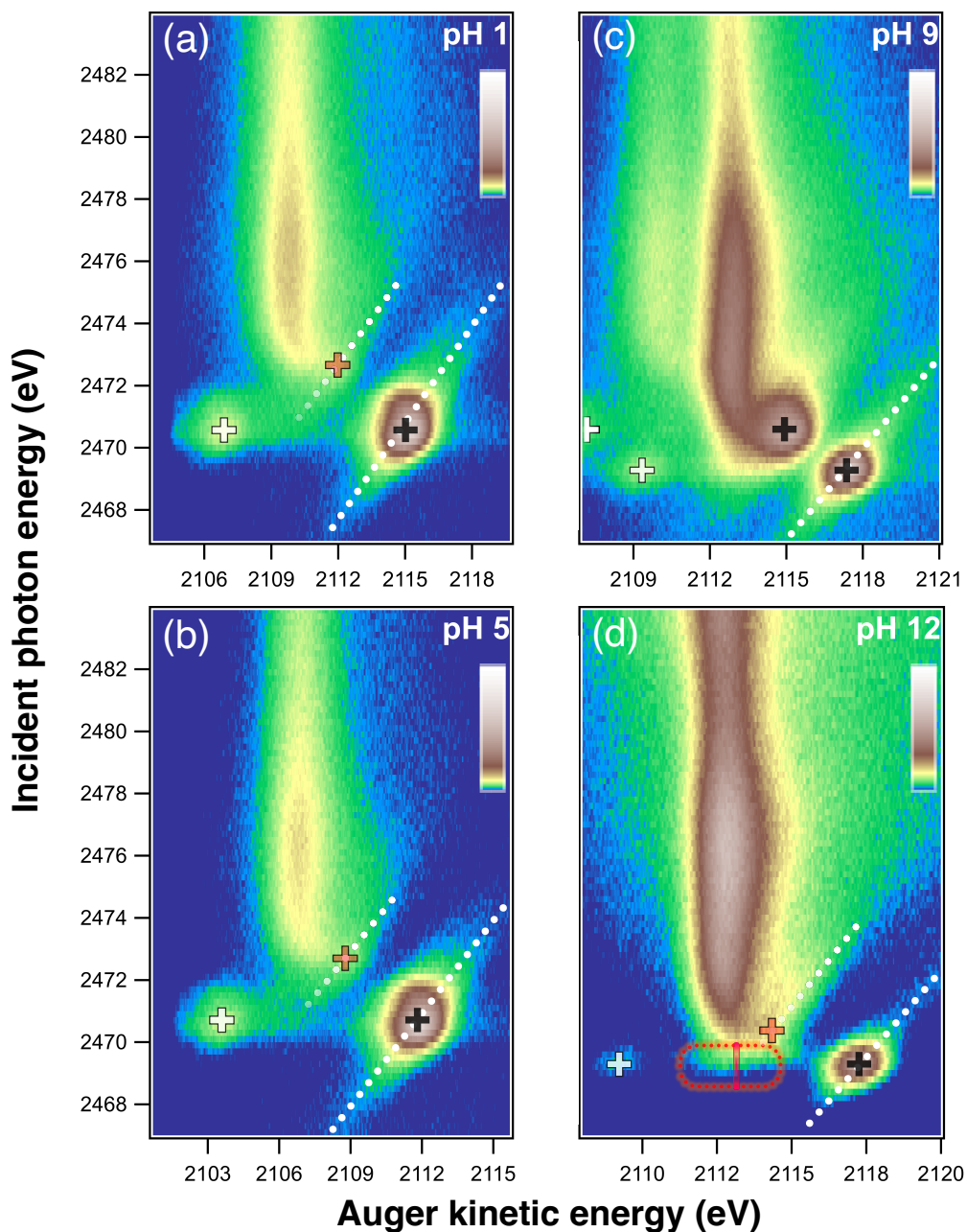


Figure 5.5: 2D maps of S $KL_{2,3}L_{2,3}$ Auger spectra recorded in aqueous L-cysteine at pH 1 (a), 5 (b), 9 (c), 12 (d). The maps are normalized to the background. The color-coded intensities are on a logarithmic scale. Diagonal dotted lines show dispersive behavior of resonant structures. Black/orange and white crosses indicate transitions to $2p^{-2}(^1D)V$ and $2p^{-2}(^1S)V$ final states, respectively, where V is the molecular orbital occupied by the spectator electron and assigned in Table 5.2. Dotted line stadium shape indicates region where CT is prominent. Vertical red line within dotted line highlighting constant kinetic energy of the CT channel.

5.4.1 Resonant electron delocalization

At pH 9, Fig. 5.5 (c), the features in the 2D map are a mixture of the zwitterionic at pH 5, and the fully deprotonated form at pH 12. The fully protonated form at pH 1 and zwitterionic form at pH 5, have strikingly similar features, as shown in Fig. 5.5 (a) and (b), respectively. Qualitative analysis will therefore be focused on the zwitterionic and fully deprotonated forms of L-cysteine, at pH 5 and 12, respectively.

At pH 12 in Fig. 5.5 (d), at photon energy around ~ 2469.4 eV one can observe two resonant structures at kinetic energies around ~ 2117.3 eV and ~ 2109.2 eV, corresponding to spectator Auger transitions to $2p^{-2}(^1D)\sigma_{(S-C)}^*$ and $2p^{-2}(^1S)\sigma_{(S-C)}^*$ final states, labeled with black and white crosses, respectively. Furthermore, at a kinetic energy ~ 2112.8 eV, we observe an additional feature highlighted within a red dashed stadium shape in Fig. 5.5 (d). The kinetic energy of this spectral line (highlighted by the red vertical line), is close to that of the normal Auger line measured far above the absorption edge. Thus, we tentatively attribute it to electron delocalization from $1s^{-1}\sigma_{(S-C)}^*$ state and refer to as CT channel in the following.

Note that the resonant spectator channels exhibit quasi-linear dispersion of the kinetic energy as a function of the incident photon energy, as the experimental conditions are in compliance with Auger Resonant Raman conditions. The dispersion of the resonant structure indicated by the orange cross in Fig. 5.5 (d), extends down to a photon energy ~ 2469.4 eV where it can overlap with the CT channel.

At pH 5 in Fig. 5.5 (b), at the excitation energy of ~ 2470.6 eV the resonant structures are marked with white and black crosses, there is no indicative of any additional peaks. A comparison of the resonant Auger spectra at pH 5 and pH 12, at their respective excitation energies is presented in Fig. 5.6. It is evident that there is no indication of electron delocalization at pH 5, nor is there a trace of the tail of the resonance corresponding to the orange cross. The latter is due to the photon energy separation between the resonances, which is approximately twice as large at pH 5 compared to pH 12. In contrast, at

pH 12, the broad structure to the left of the dominant resonant Raman channel contains contributions from both the CT channel (Fig. 5.6, red fitted peak) and the lower photon energy tail of the spectator resonant Auger line corresponding to the orange cross (Fig. 5.6, blue fitted peak).

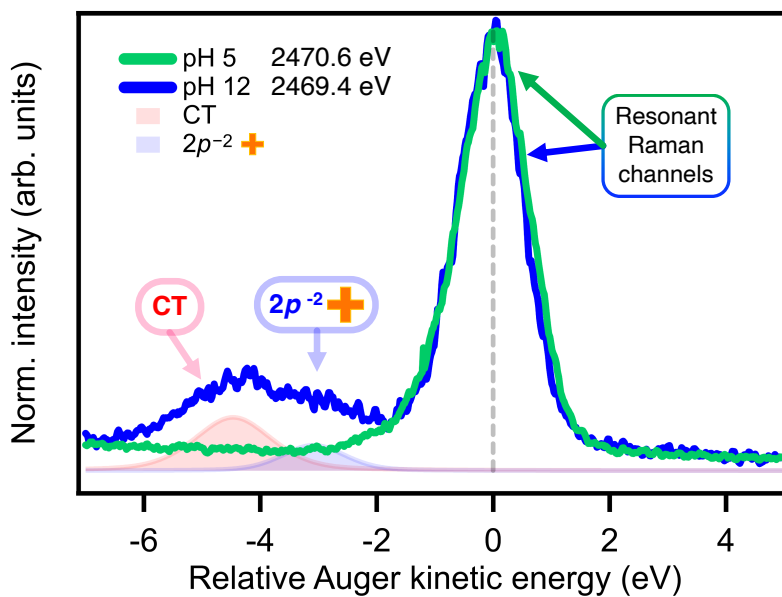


Figure 5.6: $S KL_{2,3}L_{2,3}$ Auger spectra recorded at the top of the absorption resonance at pH 5 and pH 12, at corresponding incident photon energies. At pH 12, the resonant Raman channel (blue arrow) corresponds to the resonant structure indicated by a black cross in Fig. 5.5 (d) (transition 1 or 2 of $\sigma_{(S-C)}^*CT$ character, in Table 5.2). At pH 5 the resonant Raman channel (green arrow), corresponds to the resonant structure indicated by a black cross in Fig. 5.5 (b) (transition 1 or 2 in Table 5.2). Red CT label, red translucent peak indicate CT channel. Blue $2p^{-2}$ orange cross label, blue translucent peak, orange cross indicate a dispersive lower photon energy tail originating from resonant structure marked with an orange cross in Fig. 5.5 (d) (transition present in calculated spectrum but unassigned by Risberg et al.). Auger kinetic energies relative to the maximum intensity of the dominant resonant Raman channel.

As explained in Chapter 1, and as presented in Chapter 4, it is possible to identify the CT channel by plotting the dispersion of the peak position of the resonant and CT channels as a function of the incident photon energy. The kinetic energy of the CT channel will display a constant trend, being independent of the photon energy, while resonant channels will exhibit a quasi-linear dispersion. In Fig. 5.7 is presented the kinetic energy of the resonant spectator and CT channels as a function of the incident photon energy. It is evident that the kinetic energy of the CT channel shows no dependence on the photon

energy, behavior which is characteristic of electron delocalization, contrary to the case of the resonant Raman channels, which display a dispersive behavior as a function of photon energy. We therefore tentatively attribute the feature in Fig. 5.6, at pH 12 to electron delocalization from the resonantly excited $1s^{-1}\sigma_{(S-C)}^*$ CT state to the solvent, based on our experimental observations and calculations by Risberg et al.

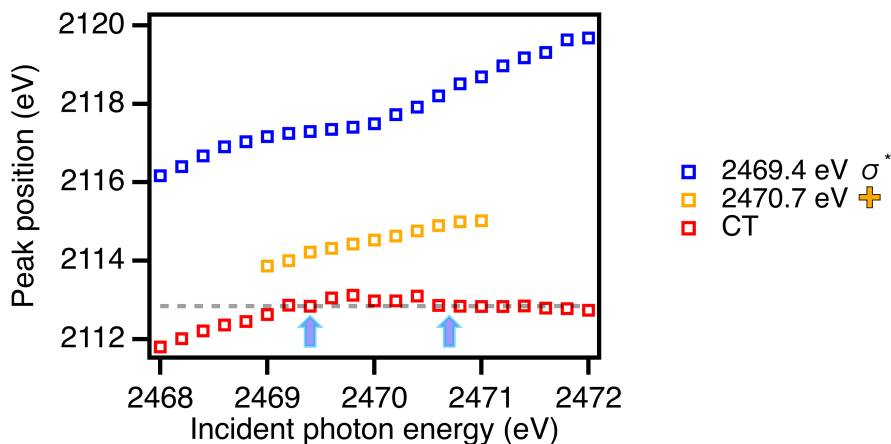


Figure 5.7: Kinetic energy position of Auger electron lines recorded at pH 12 as a function of photon energy. Blue arrows indicate the resonant excitation photon energy of the resonant structures at ~ 2469.4 eV (blue), and ~ 2470.7 eV (orange). Resonant spectator channels in blue and orange show a quasi-linear photon energy dependence. Dashed horizontal line highlights the constant kinetic energy of the CT channel in red. The systematic error from the fitting procedure is within the size of the marker. Low statistics at lower incident photon energies and overlap of features close and above the resonant spectator channel at ~ 2470.7 eV (orange) impeded a reliable fitting procedure.

Using the CHCS method, we employed Eq. 5.3.1 to obtain an estimate of the electron delocalization time. With the CHCS method, τ_{CT} can be calculated from the core-hole lifetime and the ratio of the integrated intensities of the spectator Auger channel and the CT channel, yielding $\tau_{CT} \approx 6.3$ femtoseconds, at the resonant excitation energy of the dominant $\sigma_{(S-C)}^*$ state at ~ 2469.4 eV (indicated with a black cross), and $\tau_{CT} \approx 1.0$ femtoseconds, at the resonant excitation energy of the weaker state at ~ 2470.7 eV indicated with an orange cross. As mentioned in the previous section, this resonant structure is very possibly independent of the pH of the solution, and it may in turn be related to solvation itself, likely contributing to the CT process observed in L-cysteine.

5.4.2 CT above the ionization threshold

As observed by Miteva et al., in Auger spectra above the IP, CT from solvent to solute may be manifested as a broad structure to the lower kinetic energy side of the NA line (1D_2) [103]. In our measurements for all pH values, at incident photon energies ~ 50 eV $- 1$ keV above threshold, a similar feature is visible to the lower kinetic energy side of the NA line. A qualitative assessment of the feature is presented in Fig. 5.8, where a peak was fitted at approx. -1.5 eV of the 1D_2 line at pH 12, highlighting the lineshape similarity of the CT shoulder at all pH values.

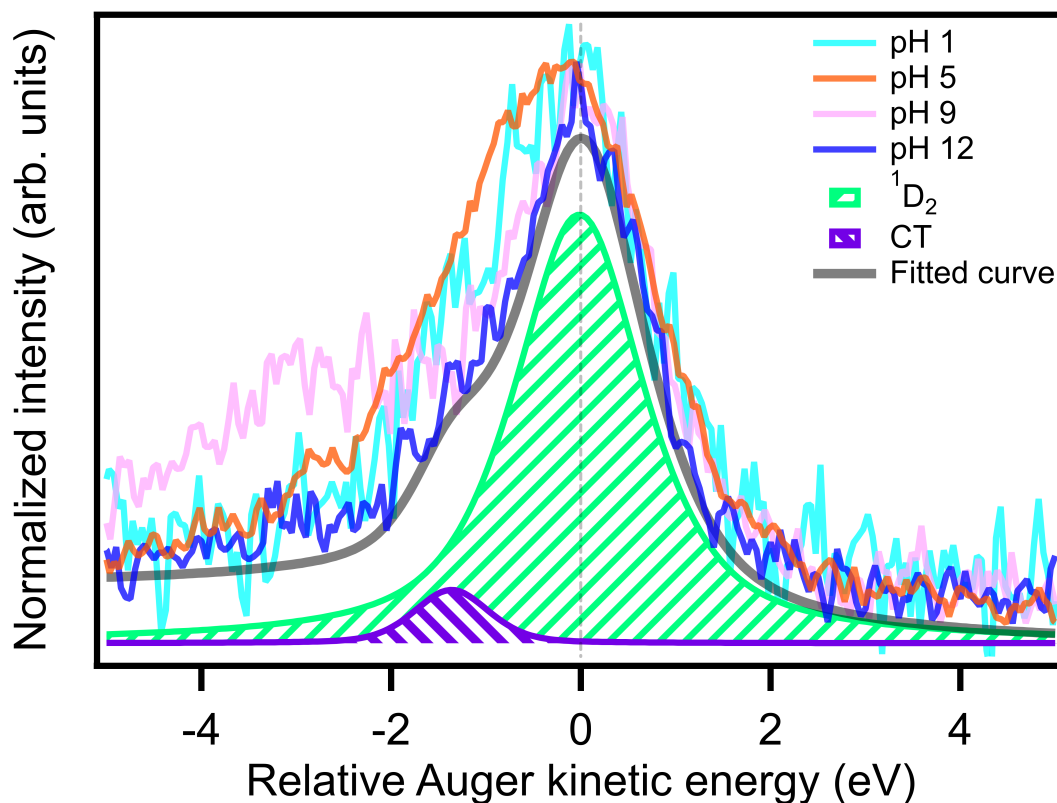


Figure 5.8: S $KL_{2,3}L_{2,3}$ Auger spectra recorded pH 1, 5, 9, 12 measured at ~ 1 keV above the S 1s absorption edge. Fitted peaks correspond to a fit performed at pH 12 to qualitatively highlight the shoulder attributed to CT present at all pH values. Auger kinetic energies relative to the maximum intensity of the 1D_2 NA line. Shoulder at pH 9 at approx. -3 eV of the main 1D_2 line corresponds to the NA line of the zwitterionic fractional component present at this pH.

In the following, the discussion will be focused on features appearing in Auger

spectra at pH 5. In Fig 5.9, are presented selected Auger spectra measured in a range between 1 eV and 1 keV above the S 1s absorption edge. The CT feature, which is independent of the incident photon energy and has therefore a constant kinetic energy, is visible between 45 eV and 1 keV above the absorption edge, highlighted by a green box. Between 20 eV and 45 eV above threshold, highlighted in the blue box, the CT feature disappears (at 45 eV above threshold) from the lower kinetic energy side of the NA line while a new feature emerges, at the higher kinetic energy side of the NA line (at 20 eV above threshold). This new feature can be observed from 20 eV down to 1 eV above the edge, highlighted in the pink box, has a constant kinetic energy. While PCI is present, it was not possible to estimate the PCI shift, as we have no accurate kinetic energy calibration between measurements. The feature is not attributed to the latter phenomenon, as the new feature (in the pink box) is manifested as an energetically separate structure and not as an asymmetry of the NA line. Interestingly, this new feature is only visible at pH 1 and 5, when L-cysteine is fully protonated, and in zwitterionic form, respectively. In both cases the proton remains bonded to the sulfur atom, while upon deprotonation the new feature is not observed.

At this stage, we have no explanation for the pH-dependent behavior of the feature to the higher kinetic energy side of the NA line (pink box). It likely has an origin in the protonation state of the thiol group, and is perhaps related to the electron delocalization feature observed only when the thiolate group dominates the titration curve of L-cysteine. Additionally, while the CT from solvent to solute observed by Miteva et al., occurs directly above the K 1s ionization energy, in our observations, the spectral feature related to CT appears only above ~ 45 eV, hinting at a different mechanism. As shown by Püttner et al., in gaseous argon, several types of Auger transitions can be distinguished, some of which are only possible only with incident photon energies that are high enough to form the corresponding initial state [161]. It is likely, therefore, that one (or more) of these mechanisms of Auger decay enables CT between the surrounding water molecules and L-cysteine.

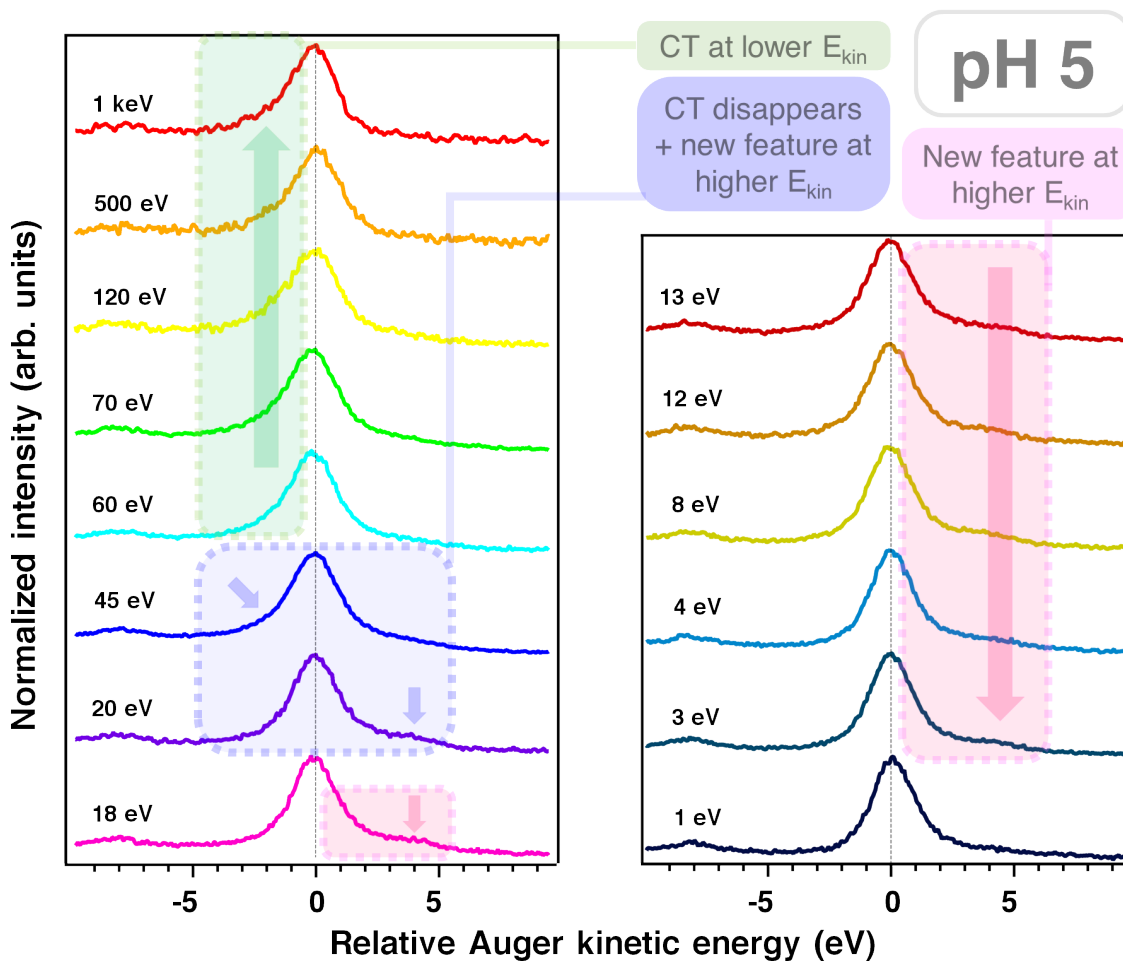


Figure 5.9: S $KL_{2,3}L_{2,3}$ Auger spectra recorded at pH 5 at photon energies ranging from 1 keV to 1 eV above the S $1s$ ionization threshold (~ 2476.3 eV for L-cysteine at pH 5.1 from Ref. [57]). Translucent boxes highlight features discussed in main text. Auger kinetic energies relative to the maximum intensity of the 1D_2 NA line.

5.5 Computational analysis

A basic picture of the CT process upon core-ionization can be obtained by TP-DFT XAS simulations. Electron density plots were obtained for GS, CES, and CIS, where the latter two were calculated using the Z+1 approximation. By plotting the difference between two electron densities, it is possible to obtain a preliminary snapshot of the electron distribution upon ionization without resorting to more computationally expensive methods.

In Fig. 5.10 is presented an electron density difference plot in which the CES electron density isosurface volume was subtracted from that of the CIS, providing a qualitative view of the electron distribution upon core ionization. As observed in the figure, there is electron density on the oxygen atom of the water molecule anchored nearest to the thiol group. This electron density is only observed in the core-ionization calculated electron density and not in the core-excited case. However, in the latter case, the calculations allowed only to promote an electron to the lowest unoccupied molecular orbital, therefore it cannot be ruled out that core-excitation to molecular orbitals at higher photon energies may allow electron density to be distributed from a water molecule to the sulfur atom.

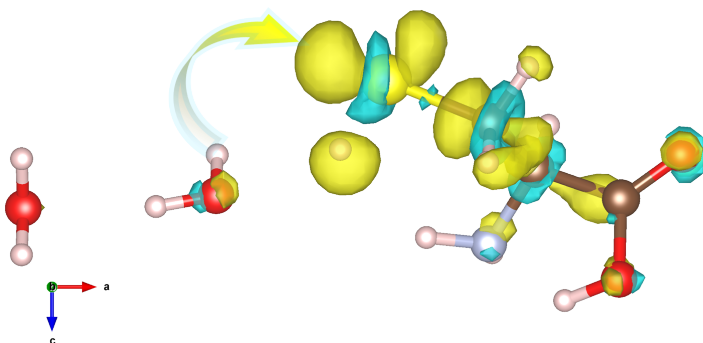


Figure 5.10: Electron density difference plot of zwitterionic L-cysteine between CES and CIS. Arrow indicates increase of electron density upon core-ionization in the oxygen atom being redistributed to the sulfur atom.

Through AIMD simulations it is possible to extract information about dynamics and electronic structure in extended supercells, particularly in terms of hydrogen

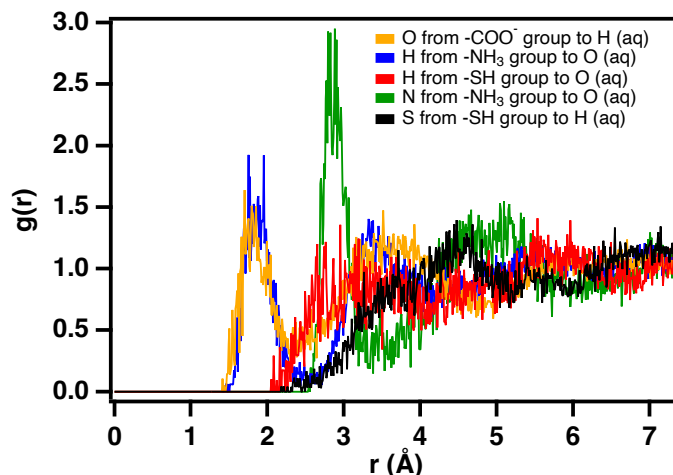


Figure 5.11: Radial distribution functions of atoms present in functional groups of L-cysteine to atoms in water (aq) molecules, obtained from AIMD simulations.

bonding. In Fig. 5.11 are compared the radial distribution function $g(r)$ of atoms in the functional groups in solvated zwitterionic L-cysteine coordinated to atoms in the water molecules part of the solvation cage. The $g(r)$ were obtained from AIMD simulations of zwitterionic L-cysteine in the GS. In the figure, the first coordination shells observed correspond to $\text{H}(\text{NH}_3) \cdots \text{O}(\text{H}_2\text{O})$ and $\text{O}(\text{COO}^-) \cdots \text{H}(\text{H}_2\text{O})$, at ~ 1.9 Å. At ~ 2.9 Å, the first coordination shell of $\text{N}(\text{NH}_3) \cdots \text{O}(\text{H}_2\text{O})$ is observed. The first shell of $\text{S}(\text{SH}) \cdots \text{H}(\text{H}_2\text{O})$ is found at ~ 3.7 Å while a second can be observed at ~ 4.5 Å. For $\text{H}(\text{SH}) \cdots \text{O}(\text{H}_2\text{O})$, a broad shell is located between $\sim 2.8 - 3.3$ Å.

From the $g(r)$ in Fig. 5.11, it can be observed that both carboxylate and ammonium groups are closely anchored to water molecules via hydrogen bonds. The nitrogen atom is observed at a larger distance compared to the hydrogens in the charged ammonium group, due to the trigonal pyramidal geometry causing the hydrogen atoms to project outwardly. The thiol group displays an interesting behavior in that both first discernible shells of both sulfur and hydrogen, coordinated to hydrogen and oxygen atoms in water, respectively, are broad structures. This likely indicates that the thiol-water interaction while weak in nature, is stabilized by the hydrogen bonding network coordinated to the carboxylate and ammonium groups [205,206]. It is possible, therefore, that as suggested

by Sarangi et al. [57], the water molecules part of the stabilization network will exchange with bulk water molecules, but at much a slower rate than that of the bulk exchange rate, as shown in Fig. 5.12. The slow-paced exchange may contribute to back-scattering manifested as a broad structure in XAS spectra, particularly strong at high pH, when the amino acid is fully deprotonated. It can be rationalized that the thiolate form, with a negatively charged sulfur atom, can coordinate to hydrogen atoms in water molecules more closely due to their partial positive charge, increasing the stability of the water network directly attached to the negatively charged sulfur atom, leading to increased backscattering. The increased proximity of the water molecules to the sulfur atom upon deprotonation might also facilitate electron delocalization towards neighboring solvent molecules.

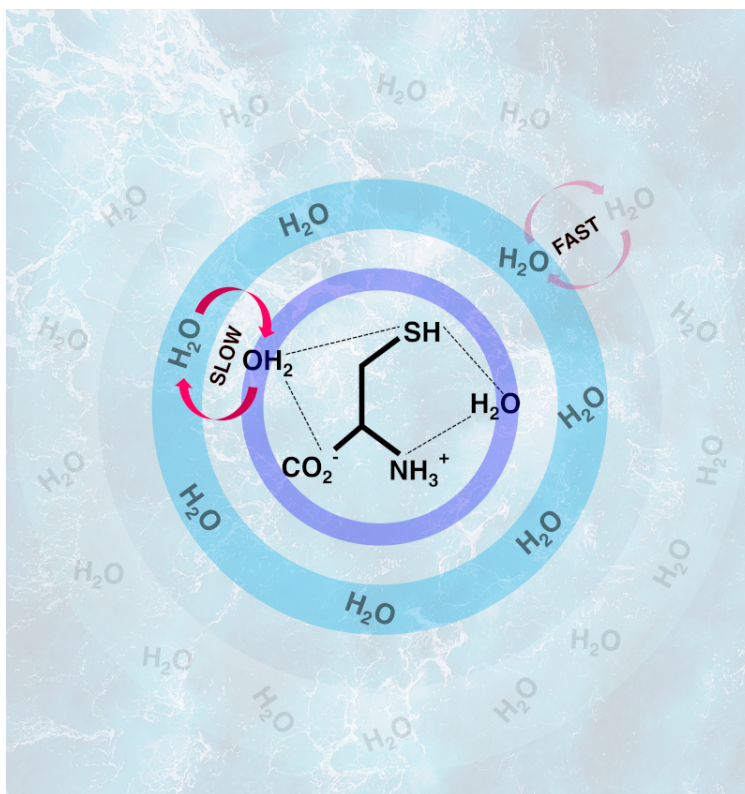


Figure 5.12: Cartoon of solvated zwitterionic L-cysteine. Purple shell indicates the water molecules part of the stabilization network. Blue and light blue shells indicate bulk solvation shells. Red arrows indicate water molecule exchange: slow between stabilization network and bulk, and fast between bulk water molecules. Dashed lines indicate hydrogen bonding.

5.6 Conclusion

Through this combined experimental and theoretical study we expect to establish the first step in the theory and interpretation of the presence of ultrafast CT in aqueous solution of L-cysteine, initiated by hard x-ray excitation at the sulfur *K*-edge. There are three main observations which indicate that the protonation state of the sulfur atom, dictated by pH, plays a vital role in the phenomena observed.

- CT was observed to occur in the resonant region only when L-cysteine is fully deprotonated at pH 12. While CT is absent in the fully protonated and zwitterionic forms. This likely has an origin in an increase of the density of water molecules in proximity to the negatively charged sulfur atom.
- Non-resonant CT was observed to occur above the ionization threshold at all pH.
- At photon energies approaching the threshold, a new feature emerges only at pH values when the thiol form dominates.

Theoretical efforts are being carried out by our collaborators Michael Odelius from Stockholm University (who hosted me during a five-week-long secondment, within the SMART-X framework), and Marcella Iannuzzi from the University of Zurich, both of whom were an integral part of the results presented in Chapter 4. The theory consists of a variety of approaches ranging from classical MD to ab initio methods. AIMD simulations with an extended water network at different pH values are under way. The purpose is to obtain a more complete picture by sampling the geometries of the different protonation forms, and ultimately carry out XPS / Auger calculations to obtain an interpretation of the CT features observed above and below threshold. AIMD combined with DFT simulations might assist in revealing the nature of the broad post-edge feature observed in (PEY) XAS at pH 12, which is likely related to increased backscattering caused by water exchange.

Initial theoretical calculations involving both DFT and MD methods have poten-

tially served as a stepping stone for future high level calculations, which may ultimately help elucidate the pH dependence of the CT process in the model amino acid L-cysteine.

This opens the door for explorations of charge dynamics in biologically relevant systems, and possibly increasingly complex systems. Thus, further studies of CT in biologically relevant samples can provide a wider understanding of the mechanisms behind charge transport in poly-peptides and proteins.

Chapter 6

Conclusion and perspectives

In this thesis, the formidable capabilities of the HAXPES technique have been exploited to carry out X-ray spectroscopy studies of biomolecules and organic polymers. Robust and well-established AES techniques have allowed for experiments in systems of increasing complexity. During my Ph.D., we measured systems encompassing all three fundamental phases of matter: from gas phase, to liquid phase and solid state. The aim was to investigate electron dynamics in these systems, which are of biological, environmental, and industrial relevance. Three main projects constitute the bulk of this thesis.

In the first project, described in Chapter 3, we demonstrated the presence of the PCI effect in sulfur $KL_{2,3}L_{2,3}$ Auger spectra, measured in gas phase thiophene and solid state organic polymers PT and P3HT. PCI is manifested as a distortion and blueshift of the normal Auger S $KL_{2,3}L_{2,3}$ spectrum upon S 1s ionization close to the ionization threshold. Our study shows that the PCI-induced shift of the Auger lines is stronger in solid state polymers than in the gas phase molecule. Modeling within the framework of the eikonal approximation provides satisfactory agreement with what was experimentally observed. In a solid medium two effects can influence the interaction between the photoelectron and the Auger electron. We have found that the more pronounced PCI effect observed in the polymers can be attributed to photoelectron scattering within the solid, which overcompensates the polarization screening of electron charges which leads to a decrease of the interaction. Our work demonstrated the general nature of the PCI effect occurring in different media.

In the second project, described in Chapter 4, we investigated ultrafast charge transfer (CT), resonantly induced by hard X-rays in organic thiophene-based π -conjugated polymers at the sulfur K -edge. A joint experimental and theoretical effort through combination of the CHCS method with real-time propagation TD-DFT calculations afforded us with an insight into the electron dynamics governing the CT process. The methodology employed allowed for the controlling of CT by selective excitation of a specific resonance in the sulfur atom with monochromatic X-rays. Our experimental and theoretical investigation indicates that the dominant CT mechanism occurring in

polymer in powder form and thin-films is that of electron delocalization along the polymer chain, taking place on the low-femtosecond timescale.

The third and last project focused on exploring the electron dynamics in an aqueous solution of L-cysteine, to investigate the CT process between solute and solvent, and in particular how the protonation state of the thiol group of the amino acid affected CT. Through the study we have observed ultrafast CT in an aqueous solution of L-cysteine, in the resonant region when L-cysteine is fully deprotonated. While CT is absent in the fully protonated and zwitterionic forms. Non-resonant CT was observed to occur at ~ 50 eV above the ionization threshold at all pH. Our observations indicate that the protonation state of the sulfur atom, dictated by the pH of the solution, plays a vital role in the phenomena observed. A preliminary theoretical effort using DFT and MD was the stepping stone for future high level calculations, which may ultimately help elucidate the pH dependence of the CT process in the model amino acid L-cysteine.

While this thesis represents a step forward, where we extended our investigations in the gas phase to the condensed phase, there remain diverse avenues of exploration. As regards PCI, it would be of great interest to find a suitable range of materials in which the interplay of electron scattering and dielectric screening can be probed in more detail. Furthermore, it would be interesting to study how the PCI effect is manifested in earth abundant metals and their oxide counterparts. Iron and cobalt are the target of many investigations which employ spectroscopic techniques, due to their attractive properties as photosensitizers or photocatalysts, compared to expensive and at times harmful complexes which employ e.g. osmium or iridium. Of particular interest is how the degree of crystallinity and size of the band gap would affect PCI. Currently, our model cannot take into consideration crystallinity, as such, exploring PCI in crystalline condensed phase materials with an expanded theoretical model, while a sizable undertaking, could lead to better understanding of PCI and its manifestation in electron spectra.

Concerning CT, furthering our investigations in polymers would be of great ap-

peal to the photovoltaics and condensed matter community in general. Here, probing CT in polymers with reduced interlayer distance could potentially lead to electron delocalization, due to the increased proximity of the π^* orbitals extending along the chains. As demonstrated by Garratt et al. through TR-XAS, exciton delocalization is significantly dependent of the distance between polymer chains, and therefore the interchain coupling strength [146]. Therefore, exploring electron delocalization with the CHCS method in organic polymers with different stacking distances, would be a logical next step through which to probe electron delocalization upon resonant excitation at the sulfur *K*-edge.

Combining HAXPES and ever-relevant biomolecules to further the existing knowledge on DNA is another promising potential project, in which by means of liquid-jet HAXPES, aqueous DNA and aqueous methylated DNA could be measured, since methylation is an essential process in repression of gene transcription. DNA is also used for metal sensing [207], where metals can be detected by DNA on a parts-per-billion level. Metal binding can be carried out via DNA-based catalysts, however, the binding processes are not well-understood, in this light, exploring delocalization or CT processes might offer new insights hitherto unexplored with HAXPES.

A direct extension of the last project presented in this thesis, could be the study of methionine with HAXPES to probe for the presence of CT. In this case, the replacement of the hydrogen atom by a methyl group, and an additional methylene in the amino acid structure could completely hinder the CT process. On the other hand the remaining electron density on the sulfur atom in methionine could still allow for charge transfer by coordination of a water molecule to the sulfur atom. Another possibility is applying liquid-jet HAXPES with selenocysteine, which is considered as the 21st amino acid. Selenocysteine is much more reactive than cysteine, with selenols being more acidic and more reducing than thiols [208, 209]. Consequently, selenocysteine is a promising candidate for observing CT through HAXPES, as the CT process may be manifested more prominently in Auger electron spectra.

Complex systems, such as proteins, and metalloenzymes, are excellent candidates to study using XFELs, where the extremely short and tunable pulses allow for experiments to be measured under in-situ and in-operando conditions in real time [210]. Combining XFEL radiation with our recent experience with RAS and RIXS measurements of L-cysteine and RIXS measurements of solvated transition metals would potentially allow us to explore e.g. rubredoxins, whose active sites consist of iron, sulfur, and are involved in electron transfer processes in biological systems.

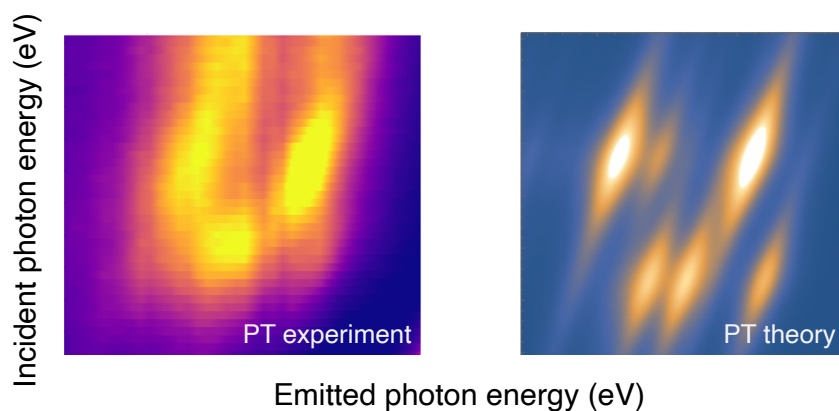


Figure 6.1: Experimental (left) and theoretical (right) $K\beta$ RIXS planes for PT in powder form.

In terms of future studies, we have measured a variety of samples using RIXS, using the newly commissioned MOSARIX setup. From samples in the solid state such as PT, bithiophene, L-cysteine. To samples in the liquid phase, such as FeCl_3 , and KCl. RIXS has the advantage that it is not encumbered by surface charge effects. In PT, we are investigating conjugation and hyper-conjugation effects in core-excited molecules, which have been previously probed in gaseous systems by RAS [160]. As a natural continuation of the study, we have extended the investigation towards the solid state. Analysis of the experimental data obtained with MOSARIX and theoretical RIXS calculations are currently in progress. In Fig 6.1 is shown a comparison of experimental and preliminary theoretical results of PT.

Bibliography

- [1] H. Hertz. Ueber einen Einfluss des ultravioletten Lichtes auf die electrische Entladung. Ann. Phys. Chem., 267(8):983–1000, 1887.
- [2] A. Einstein. Über einen die Erzeugung und Verwandlung des Lichtes betreffenden heuristischen Gesichtspunkt. Ann. Phys., 322(6):132–148, 1905.
- [3] M. O. Krause. Atomic radiative and radiationless yields for *K* and *L* shells. Journal of Physical and Chemical Reference Data, 8(2):307–327, April 1979.
- [4] M Kuchiev and S Sheinerman. Post-collision interaction in atomic processes. Sov. Phys. Usp., 32:569, 1989.
- [5] V Schmidt. Photoionization of atoms using synchrotron radiation. Rep. Prog. Phys., 55(9):1483–1659, September 1992.
- [6] D. L. Hansen, G. B. Armen, M. E. Arrasate, J. Cotter, G. R. Fisher, K. T. Leung, J. C. Levin, R. Martin, P. Neill, R. C. C. Perera, I. A. Sellin, M. Simon, Y. Uehara, B. Vanderford, S. B. Whitfield, and D. W. Lindle. Postcollision-interaction effects in HCl following photofragmentation near the chlorine K edge. Phys. Rev. A, 57(6):R4090–R4093, June 1998.
- [7] D. L. Hansen, W. C. Stolte, O. Hemmers, R. Guillemin, and D. W. Lindle. Anion formation moderated by post-collision interaction following core-level pho-

- toexcitation of CO. Journal of Physics B: Atomic, Molecular and Optical Physics, 35(17):L381–L386, August 2002. Publisher: IOP Publishing.
- [8] M. K. Odling-Smee, E. Sokell, A. A. Wills, and P. Hammond. Observation of post-collision interaction (PCI) in HBr using two-dimensional photoelectron spectroscopy. Journal of Physics B: Atomic, Molecular and Optical Physics, 32(11):2529–2537, January 1999. Publisher: IOP Publishing.
- [9] R. Guillemin, S. Sheinerman, C. Bomme, L. Journal, T. Marin, T. Marchenko, R. K. Kushawaha, N. Trcera, M. N. Piancastelli, and M. Simon. Ultrafast Dynamics in Postcollision Interaction after Multiple Auger Decays in Argon 1 s Photoionization. Phys. Rev. Lett., 109(1):013001, July 2012.
- [10] C Bomme, R Guillemin, S Sheinerman, T Marin, L Journal, T Marchenko, R K Kushawaha, N Trcera, M N Piancastelli, and M Simon. Post-collision interaction manifestation in molecular systems probed by photoelectron-molecular ion coincidences. J. Phys. B: At. Mol. Opt. Phys., 46(21):215101, November 2013.
- [11] R. Guillemin, S. Sheinerman, R. Püttner, T. Marchenko, G. Goldsztejn, L. Journal, R. K. Kushawaha, D. Céolin, M. N. Piancastelli, and M. Simon. Postcollision interaction effects in K L L Auger spectra following argon 1 s photoionization. Phys. Rev. A, 92(1):012503, July 2015.
- [12] Nicolas Velasquez, Oksana Travnikova, Renaud Guillemin, Iyas Ismail, Loïc Journal, Jessica B. Martins, Dimitris Koulentianos, Denis Céolin, Laure Fillaud, Maria Luiza M. Rocco, Ralph Püttner, Maria Novella Piancastelli, Marc Simon, Sergei Sheinerman, Leonid Gerchikov, and Tatiana Marchenko. Generalization of the post-collision interaction effect from gas-phase to solid-state systems demonstrated in thiophene and its polymers. Phys. Rev. Research, 5(1):013048, January 2023.
- [13] M. Yu. Kuchiev and S. A. Sheinerman. Resonant processes involving the production of three charged particles. Sov. Phys. JETP, 63(5):986–990, May 1986.

- [14] M.N. Piancastelli. Auger resonant Raman studies of atoms and molecules. Journal of Electron Spectroscopy and Related Phenomena, 107(1):1–26, March 2000.
- [15] P. Eisenberger, P. M. Platzman, and H. Winick. X-Ray Resonant Raman Scattering: Observation of Characteristic Radiation Narrower than the Lifetime Width. Phys. Rev. Lett., 36(11):623–626, March 1976.
- [16] George S. Brown, Mau Hsiung Chen, Bernd Crasemann, and Gene E. Ice. Observation of the Auger Resonant Raman Effect. Phys. Rev. Lett., 45(24):1937–1940, December 1980.
- [17] G. Bradley Armen, Teijo Åberg, Jon C. Levin, Bernd Crasemann, Mau Hsiung Chen, Gene E. Ice, and George S. Brown. Threshold Excitation of Short-Lived Atomic Inner-Shell Hole States with Synchrotron Radiation. Phys. Rev. Lett., 54(11):1142–1145, March 1985.
- [18] A. Kivimäki, A. Naves de Brito, S. Aksela, H. Aksela, O.-P. Sairanen, A. Ausmees, S. J. Osborne, L. B. Dantas, and S. Svensson. Subnatural linewidths in the Kr M 5 N 2 , 3 N 2 , 3 and Xe N 5 O 2 , 3 O 2 , 3 resonant Auger spectra. Phys. Rev. Lett., 71(26):4307–4310, December 1993.
- [19] S. Aksela, E. Kukk, H. Aksela, and S. Svensson. Experimental Verification of the Line-Shape Distortion in Resonance Auger Spectra. Phys. Rev. Lett., 74(15):2917–2920, April 1995.
- [20] E. Kukk, S. Aksela, and H. Aksela. Features of the Auger resonant Raman effect in experimental spectra. Phys. Rev. A, 53(5):3271–3277, May 1996.
- [21] T. Marchenko, G. Goldsztejn, K. Jankala, O. Travnikova, L. Journel, R. Guillemin, N. Sisourat, D. Ceolin, M. Zitnik, M. Kavcic, K. Bucar, A. Mihelic, B. Cunha de Miranda, I. Ismail, A. F. Lago, F. Gel'mukhanov, R. Puttner, M. N. Piancastelli, and M. Simon. Potential Energy Surface Reconstruction and Lifetime Determination of

- Molecular Double-Core-Hole States in the Hard X-Ray Regime. Phys. Rev. Lett., 119(13):133001, September 2017.
- [22] J. R. Taylor. Scattering Theory: The quantum Theory on Nonrelativistic Collisions. Wiley, New York, 1972.
- [23] T Aberg. Unified Theory of Auger Electron Emission. Physica Scripta T, 1992(T41):71–76, 1992.
- [24] M. Simon, L. Journal, R. Guillemin, W. C. Stolte, I. Minkov, F. Gel'mukhanov, P. Sałek, H. Ågren, S. Carniato, R. Taïeb, A. C. Hudson, and D. W. Lindle. Femtosecond nuclear motion of HCl probed by resonant x-ray Raman scattering in the Cl 1 s region. Phys. Rev. A, 73(2):020706, February 2006.
- [25] Faris Gel'mukhanov and Hans Ågren. Resonant X-ray Raman scattering. Physics Reports, 312(3):87–330, 1999.
- [26] G Bradley Armen, Helena Aksela, Teijo Åberg, and Seppo Aksela. The resonant Auger effect. J. Phys. B: At. Mol. Opt. Phys., 33(2):R49–R92, January 2000.
- [27] Maria Novella Piancastelli, Gildas Goldsztejn, Tatiana Marchenko, Renaud Guillemin, Rajesh K Kushawaha, Loïc Journal, Stéphane Carniato, Jean-Pascal Rueff, Denis Céolin, and Marc Simon. Core-hole-clock spectroscopies in the tender x-ray domain. J. Phys. B: At. Mol. Opt. Phys., 47(12):124031, June 2014.
- [28] O. Björneholm, A. Nilsson, A. Sandell, B. Hernnäs, and N. Mrtensson. Determination of time scales for charge-transfer screening in physisorbed molecules. Phys. Rev. Lett., 68(12):1892–1895, March 1992.
- [29] O. Björneholm, S. Sundin, S. Svensson, R. R. T. Marinho, A. Naves de Brito, F. Gel'mukhanov, and H. Ågren. Femtosecond Dissociation of Core-Excited HCl Monitored by Frequency Detuning. Phys. Rev. Lett., 79(17):3150–3153, October 1997.

- [30] P. A. Brühwiler, O. Karis, and N. Mårtensson. Charge-transfer dynamics studied using resonant core spectroscopies. Rev. Mod. Phys., 74(3):703–740, July 2002.
- [31] Dietrich Menzel. Ultrafast charge transfer at surfaces accessed by core electron spectroscopies. Chem. Soc. Rev., 37(10):2212, 2008.
- [32] A. Baev, P. Sałek, F.Kh. Gel'mukhanov, H. Ågren, A. Naves de Brito, O. Björneholm, and S. Svensson. Picturing molecular femtosecond processes through an ultra-fast controllable X-ray shutter. Chemical Physics, 289(1):51–56, April 2003.
- [33] P. Skytt, P. Glans, J.-H. Guo, K. Gunnelin, C. Sâthe, J. Nordgren, F. Kh. Gel'mukhanov, A. Cesar, and H. Ågren. Quenching of Symmetry Breaking in Resonant Inelastic X-Ray Scattering by Detuned Excitation. Phys. Rev. Lett., 77(25):5035–5038, December 1996.
- [34] Faris Gel'mukhanov, Paweł Sałek, Timofei Privalov, and Hans Ågren. Duration of x-ray Raman scattering. Phys. Rev. A, 59(1):380–389, 1999.
- [35] Faris Gel'mukhanov, Michael Odelius, Sergey P. Polyutov, Alexander Föhlisch, and Victor Kimberg. Dynamics of resonant x-ray and Auger scattering. Rev. Mod. Phys., 93(3):035001, July 2021.
- [36] O. Travnikova, N. Sisourat, T. Marchenko, G. Goldsztejn, R. Guillemin, L. Journal, D. Céolin, I. Ismail, A. F. Lago, R. Püttner, M. N. Piancastelli, and M. Simon. Sub-femtosecond Control of Molecular Fragmentation by Hard X-Ray Photons. Phys. Rev. Lett., 118(21):213001, May 2017.
- [37] T. Marchenko, L. Journal, T. Marin, R. Guillemin, S. Carniato, M. Žitnik, M. Kavčič, K. Bučar, A. Mihelič, J. Hoszowska, W. Cao, and M. Simon. Resonant inelastic x-ray scattering at the limit of subfemtosecond natural lifetime. The Journal of Chemical Physics, 134(14):144308, April 2011.
- [38] M. Drescher, M. Hentschel, R. Kienberger, M. Uiberacker, V. Yakovlev, A. Scrinzi,

- Th. Westerwalbesloh, U. Kleineberg, U. Heinzmann, and F. Krausz. Time-resolved atomic inner-shell spectroscopy. Nature, 419(6909):803–807, October 2002.
- [39] F. Calegari, D. Ayuso, A. Trabattoni, L. Belshaw, S. De Camillis, S. Anumula, F. Frassetto, L. Poletto, A. Palacios, P. Decleva, J. B. Greenwood, F. Martín, and M. Nisoli. Ultrafast electron dynamics in phenylalanine initiated by attosecond pulses. Science, 346(6207):336–339, October 2014.
- [40] S Serkez, G Geloni, S Tomin, G Feng, E V Gryzlova, A N Grum-Grzhimailo, and M Meyer. Overview of options for generating high-brightness attosecond x-ray pulses at free-electron lasers and applications at the European XFEL. J. Opt., 20(2):024005, February 2018.
- [41] Daniel E. Rivas, Svitozar Serkez, Thomas M. Baumann, Rebecca Boll, Marie Kristin Czwalinna, Simon Dold, Alberto de Fanis, Natalia Gerasimova, Patrik Grychtol, Björn Lautenschlager, Maximilian Lederer, Tomasz Jezyński, Daniel Kane, Tommaso Mazza, Joachim Meier, Jost Müller, Florent Pallas, Dimitrios Rompotis, Philipp Schmidt, Sebastian Schulz, Sergey Usenko, Sandhya Venkatesan, Jinxiong Wang, and Michael Meyer. High-temporal-resolution X-ray spectroscopy with free-electron and optical lasers. Optica, 9(4):429, April 2022.
- [42] S. Nishikida and S. Ikeda. Studies on the shake-up satellites of auger spectra for potassium and calcium compounds. Journal of Electron Spectroscopy and Related Phenomena, 13(1):49–58, January 1978.
- [43] O Björneholm, A Sandell, A Nilsson, N Mårtensson, and J N Andersen. Autoionization of Adsorbates. Phys. Scr., T41:217–225, January 1992.
- [44] Hiromi Ikeura-Sekiguchi and Tetsuhiro Sekiguchi. Attosecond Electron Delocalization in the Conduction Band through the Phosphate Backbone of Genomic DNA. Phys. Rev. Lett., 99(22):228102, November 2007.

- [45] Scott R. Rajski, Brian A. Jackson, and Jacqueline K. Barton. DNA repair: models for damage and mismatch recognition. Mutation Research/Fundamental and Molecular Mechanisms of Mutagenesis, 447(1):49–72, January 2000. Publisher: Elsevier BV.
- [46] W Wurth and D Menzel. Ultrafast electron dynamics at surfaces probed by resonant Auger spectroscopy. Chemical Physics, 251(1-3):141–149, January 2000.
- [47] M. O. Krause and J. H. Oliver. Natural widths of atomic K and L levels, K α X-ray lines and several K L Auger lines. Journal of Physical and Chemical Reference Data, 8(2):329–338, April 1979. Publisher: AIP Publishing.
- [48] Alan J. Heeger. Nobel Lecture: Semiconducting and metallic polymers: The fourth generation of polymeric materials. Rev. Mod. Phys., 73(3):681–700, September 2001.
- [49] Manu Jaiswal and Reghu Menon. Polymer electronic materials: a review of charge transport. Polym. Int., 55(12):1371–1384, December 2006.
- [50] Li Wang, Wei Chen, and Andrew Thye Shen Wee. Charge transfer across the molecule/metal interface using the core hole clock technique. Surface Science Reports, page 22, 2008.
- [51] R Friedlein. Ultra-fast charge transfer in organic electronic materials and at hybrid interfaces studied using the core-hole clock technique. Journal of Electron Spectroscopy and Related Phenomena, page 6, 2011.
- [52] Hiromi Ikeura-Sekiguchi and Tetsuhiro Sekiguchi. Unoccupied electronic states in polythiophene as probed by XAS and RAS: Unoccupied electronic states in polythiophene as probed by XAS. Surf. Interface Anal., 40(3-4):673–675, March 2008.

- [53] C. Arantes, B. G. A. L. Borges, B. Beck, G. Araújo, L. S. Roman, and M. L. M. Rocco. Femtosecond Electron Delocalization in Poly(thiophene) Probed by Resonant Auger Spectroscopy. *J. Phys. Chem. C*, 117(16):8208–8213, April 2013.
- [54] Badia Boudaiffa, Pierre Cloutier, Darel Hunting, Michael A. Huels, and Léon Sanche. Resonant Formation of DNA Strand Breaks by Low-Energy (3 to 20 eV) Electrons. *Science*, 287(5458):1658–1660, March 2000.
- [55] Vincenzo Carravetta, Anderson Herbert de Abreu Gomes, Susanna Monti, Alexandra Mocellin, Ricardo R. T. Marinho, Olle Björneholm, Hans Ågren, and Arnaldo Naves de Brito. pH-dependent X-ray Photoelectron Chemical Shifts and Surface Distribution of Cysteine in Aqueous Solution. *J. Phys. Chem. B*, 123(17):3776–3785, May 2019.
- [56] F. Meyer, M. Blum, A. Benkert, D. Hauschild, S. Nagarajan, R. G. Wilks, J. Andersson, W. Yang, M. Zharnikov, M. Bär, C. Heske, F. Reinert, and L. Weinhardt. “Building Block Picture” of the Electronic Structure of Aqueous Cysteine Derived from Resonant Inelastic Soft X-ray Scattering. *J. Phys. Chem. B*, 118(46):13142–13150, November 2014.
- [57] Ritimukta Sarangi, Patrick Frank, Maurizio Benfatto, Silvia Morante, Velia Minicozzi, Britt Hedman, and Keith O. Hodgson. The x-ray absorption spectroscopy model of solvation about sulfur in aqueous L-cysteine. *The Journal of Chemical Physics*, 137(20):205103, November 2012.
- [58] Emiliana Damian Risberg, Farideh Jalilehvand, Bonnie O. Leung, Lars G. M. Pettersson, and Magnus Sandström. Theoretical and experimental sulfur K-edge X-ray absorption spectroscopic study of cysteine, cystine, homocysteine, penicillamine, methionine and methionine sulfoxide. *Dalton Trans.*, 38(18):3542, 2009. Publisher: Royal Society of Chemistry (RSC).
- [59] Edwin M. McMillan. The Synchrotron—A Proposed High Energy Particle Acceler-

- ator. Phys. Rev., 68(5-6):143–144, September 1945.
- [60] Phil R. Willmott. An introduction to synchrotron radiation: techniques and applications. John Wiley & sons, Hoboken, 2nd ed edition, 2019.
- [61] F. R. Elder, A. M. Gurewitsch, R. V. Langmuir, and H. C. Pollock. Radiation from Electrons in a Synchrotron. Phys. Rev., 71(11):829–830, June 1947.
- [62] Settimio Mobilio, Federico Boscherini, and Carlo Meneghini, editors. Synchrotron Radiation: Basics, Methods and Applications. Springer Berlin Heidelberg, Berlin, Heidelberg, 2015.
- [63] D. H. Tomboulian and P. L. Hartman. Spectral and Angular Distribution of Ultraviolet Radiation from the 300-Mev Cornell Synchrotron. Phys. Rev., 102(6):1423–1447, June 1956.
- [64] Jens Als-Nielsen and Des McMorrow. Elements of Modern X-ray Physics. Wiley, 1 edition, March 2011.
- [65] W. Friedrich, P. Knipping, and M. von Laue. Interferenz-Erscheinungen bei Röntgenstrahlen. Mathematisch-Physikalische Klasse: Sitzungsberichte. Verlag der Kgl. Bayer. Akad. der Wiss., 1912.
- [66] Gavin Poludniowski, Artur Omar, Robert Bujila, and Pedro Andreo. Technical Note: SpekPy v2.0—a software toolkit for modeling x-ray tube spectra. Medical Physics, 48(7):3630–3637, July 2021.
- [67] J.-P. Rueff, J. M. Ablett, D. Céolin, D. Prieur, Th. Moreno, V. Balédent, B. Lassalle-Kaiser, J. E. Rault, M. Simon, and A. Shukla. The GALAXIES beamline at the SOLEIL synchrotron: inelastic X-ray scattering and photoelectron spectroscopy in the hard X-ray range. J Synchrotron Rad, 22(1):175–179, January 2015.
- [68] J. M. Ablett, D. Prieur, D. Céolin, B. Lassalle-Kaiser, B. Lebert, M. Sauvage, Th.

- Moreno, S. Bac, V. Balédent, A. Oyono, M. Morand, F. Gélebart, A. Shukla, and J.-P. Rueff. The GALAXIES inelastic hard X-ray scattering end-station at Synchrotron SOLEIL. J Synchrotron Rad, 26(1):263–271, January 2019.
- [69] D. Céolin, J.M. Ablett, D. Prieur, T. Moreno, J.-P. Rueff, T. Marchenko, L. Journal, R. Guillemin, B. Pilette, T. Marin, and M. Simon. Hard X-ray photoelectron spectroscopy on the GALAXIES beamline at the SOLEIL synchrotron. Journal of Electron Spectroscopy and Related Phenomena, 190:188–192, October 2013.
- [70] D. Koulentianos, R. Püttner, G. Goldsztejn, T. Marchenko, O. Travnikova, L. Journal, R. Guillemin, D. Céolin, M. N. Piancastelli, M. Simon, and R. Feifel. KL double core hole pre-edge states of HCl. Phys. Chem. Chem. Phys., 20(4):2724–2730, 2018.
- [71] Joseph Ladislav Wiza. MICROCHANNEL PLATE DETECTORS. Nuclear Instruments and Methods, 162:587–601, 1979.
- [72] Manfred Faubel. (54) LIQUID TRAP FOR COLLECTING LIQUIDS, 2007.
- [73] J.-P. Rueff, J. E. Rault, J. M. Ablett, Y. Utsumi, and D. Céolin. HAXPES for Materials Science at the GALAXIES Beamline. Synchrotron Radiation News, 31(4):4–9, July 2018.
- [74] Joseph Woicik, editor. Hard X-ray Photoelectron Spectroscopy (HAXPES), volume 59 of Springer Series in Surface Sciences. Springer International Publishing, Cham, 2016.
- [75] M N Piancastelli, R Guillemin, T Marchenko, L Journal, O Travnikova, T Marin, G Goldsztejn, B Cunha de Miranda, I Ismail, and M Simon. New achievements on relaxation dynamics of atoms and molecules photoexcited in the tender x-ray domain at synchrotron SOLEIL. J. Phys. B: At. Mol. Opt. Phys., 50(4):042001, February 2017.
- [76] Marc Simon, Ralph Püttner, Tatiana Marchenko, Renaud Guillemin, Rajesh K.

- Kushawaha, Loïc Journal, Gildas Goldsztejn, Maria Novella Piancastelli, James M. Ablett, Jean-Pascal Rueff, and Denis Céolin. Atomic Auger Doppler effects upon emission of fast photoelectrons. Nat Commun, 5(1):4069, September 2014.
- [77] D. Céolin, T. Marchenko, R. Guillemin, L. Journal, R. K. Kushawaha, S. Carniato, S.-M. Huttula, J. P. Rueff, G. B. Armen, M. N. Piancastelli, and M. Simon. Auger resonant-Raman study at the Ar *K* edge as probe of electronic-state-lifetime interferences. Phys. Rev. A, 91(2):022502, February 2015.
- [78] Lorenz S. Cederbaum, Francesco Tarantelli, A. Sgamellotti, and Jochen Schirmer. On double vacancies in the core. The Journal of Chemical Physics, 85:6513–6523, 1986. Publisher: AIP Publishing.
- [79] Ralph Püttner, Gildas Goldsztejn, Denis Céolin, Jean-Pascal Rueff, Thierry Moreno, Rajesh K. Kushawaha, Tatiana Marchenko, Renaud Guillemin, Loïc Journal, Dennis W. Lindle, Maria Novella Piancastelli, and Marc Simon. Direct Observation of Double-Core-Hole Shake-Up States in Photoemission. Phys. Rev. Lett., 114(9):093001, March 2015.
- [80] T. Marchenko, L. Inhester, G. Goldsztejn, O. Travnikova, L. Journal, R. Guillemin, I. Ismail, D. Koulentianos, D. Céolin, R. Püttner, M. N. Piancastelli, and M. Simon. Ultrafast nuclear dynamics in the doubly-core-ionized water molecule observed via Auger spectroscopy. Phys. Rev. A, 98(6):063403, December 2018.
- [81] E. Kukk. Spectrum Analysis by Curve Fitting (SPANCF) Macro Package for Igor Pro, 2009.
- [82] L Avaldi, G Dawber, R Camilloni, G C King, M Roper, M R F Siggel, G Stefani, and M Zitnik. Near-threshold photoionization of the Ar 2p subshell. J. Phys. B: At. Mol. Opt. Phys., 27(17):3953–3966, September 1994.
- [83] A. Kramida, Yu. Ralchenko, J. Reader, and and NIST ASD Team. NIST Atomic Spec-

- tra Database (ver. 5.10), 2022. Published: NIST Atomic Spectra Database (ver. 5.10), [Online]. Available: <https://physics.nist.gov/asd> [2023, April 17]. National Institute of Standards and Technology, Gaithersburg, MD.
- [84] E. B. Saloman. Energy Levels and Observed Spectral Lines of Ionized Argon, Ar II through Ar XVIII. Journal of Physical and Chemical Reference Data, 39(3):033101, September 2010.
- [85] James A. R. Samson. Line Broadening in Photoelectron Spectroscopy. Review of Scientific Instruments, 40(9):1174–1177, September 1969.
- [86] G. Greczynski and L. Hultman. X-ray photoelectron spectroscopy: Towards reliable binding energy referencing. Progress in Materials Science, 107:100591, January 2020.
- [87] Bernd Winter, Stephan Thürmer, and Iain Wilkinson. Absolute Electronic Energetics and Quantitative Work Functions of Liquids from Photoelectron Spectroscopy. Acc. Chem. Res., 56(2):77–85, January 2023.
- [88] Michele Pugini, Bruno Credidio, Irina Walter, Sebastian Malerz, Florian Trinter, Dominik Stemer, Uwe Hergenhausen, Gerard Meijer, Iain Wilkinson, Bernd Winter, and Stephan Thürmer. How to measure work functions from aqueous solutions. Chem. Sci., 14(35):9574–9588, 2023.
- [89] Charles Kittel. Introduction to solid state physics. Wiley, Hoboken, NJ, 8. ed. edition, 2005.
- [90] Lin Lin, Ryan Jacobs, Tianyu Ma, Dongzheng Chen, John Booske, and Dane Morgan. Work Function: Fundamentals, Measurement, Calculation, Engineering, and Applications. Phys. Rev. Applied, 19(3):037001, March 2023.
- [91] Siegfried Hofmann. Auger- and X-Ray Photoelectron Spectroscopy in Materials Science: A User-Oriented Guide, volume 49 of Springer Series in Surface Sciences.

Springer Berlin Heidelberg, Berlin, Heidelberg, 2013.

- [92] Farideh Jalilehvand. Sulfur: not a “silent” element any more. Chem. Soc. Rev., 35(12):1256–1268, 2006.
- [93] G. Vereecke and P. G. Rouxhet. Surface charging of insulating samples in x-ray photoelectron spectroscopy. Surf. Interface Anal., 26(7):490–497, June 1998.
- [94] H. Sirringhaus, P. J. Brown, R. H. Friend, M. M. Nielsen, K. Bechgaard, B. M. W. Langeveld-Voss, A. J. H. Spiering, R. A. J. Janssen, E. W. Meijer, P. Herwig, and D. M. de Leeuw. Two-dimensional charge transport in self-organized, high-mobility conjugated polymers. Nature, 401(6754):685–688, October 1999.
- [95] Dean M. DeLongchamp, Brandon M. Vogel, Youngsuk Jung, Marc C. Gurau, Curt A. Richter, Oleg A. Kirillov, Jan Obrzut, Daniel A. Fischer, Sharadha Sambasivan, Lee J. Richter, and Eric K. Lin. Variations in Semiconducting Polymer Microstructure and Hole Mobility with Spin-Coating Speed. Chem. Mater., 17(23):5610–5612, November 2005.
- [96] M E Nicho, W Jaimes, M E Rivas-Aguilar, Hailin Hu, and M A Quevedo-Lopez. Synthesis of poly (3-hexylthiophene-2,5-diy1) in presence of CdS nanoparticles: microscopic and spectroscopic studies. Rev. Mex. Fis., 2017.
- [97] Yeong Don Park. The Molecular Structures of Poly(3-hexylthiophene) Films Determine the Contact Properties at the Electrode/Semiconductor Interface. Bulletin of the Korean Chemical Society, 35(8):2277–2280, August 2014.
- [98] T. Miller and T.-C. Chiang. Solid-state screening effect on the post-collision interaction. Phys. Rev. B, 29(2):1121–1124, January 1984.
- [99] V. M. Mikushkin, A. V. Zakharevich, I. I. Pavletsov, S. E. Sysoev, V. V. Shnitov, M. Yu Kuchiev, and S. A. Sheinerman. Postcollision interaction in the excitation of a gold 4d vacancy by fast electrons. JETP Letters, 58(12):891–894, 1993.

- [100] B. Kassühlke, R. Romberg, P. Averkamp, and P. Feulner. Substrate Mediated Suppression of Postcollision Interaction Effects. Phys. Rev. Lett., 81(13):2771–2774, September 1998.
- [101] A. Lindblad, R. F. Fink, H. Bergersen, M. Lundwall, T. Rander, R. Feifel, G. Öhrwall, M. Tchapyguine, U. Hergenhahn, S. Svensson, and O. Björneholm. Postcollision interaction in noble gas clusters: Observation of differences in surface and bulk line shapes. The Journal of Chemical Physics, 123(21):211101, December 2005.
- [102] D.M Coward and S.M Thurgate. Post collision interaction in the L3–M4,5M4,5 Auger spectra in solid state copper. Journal of Electron Spectroscopy and Related Phenomena, 107(2):193–199, May 2000.
- [103] Tsveta Miteva, Nikolai V. Kryzhevoi, Nicolas Sisourat, Christophe Nicolas, Wandedared Pokapanich, Thanit Saisopa, Prayoon Songsiriritthigul, Yuttakarn Rattanachai, Andreas Dreuw, Jan Wenzel, Jérôme Palaudoux, Gunnar Öhrwall, Ralph Püttner, Lorenz S. Cederbaum, Jean-Pascal Rueff, and Denis Céolin. The All-Seeing Eye of Resonant Auger Electron Spectroscopy: A Study on Aqueous Solution Using Tender X-rays. J. Phys. Chem. Lett., 9(15):4457–4462, August 2018.
- [104] H. W. Berry. Energy Distribution of Electrons from Ionizing Collisions of Heavy Particles. Phys. Rev., 121(6):1714–1719, March 1961.
- [105] R. B. Barker and H. W. Berry. Electron Energy Distributions from Ionizing Collisions of Helium and Neon Ions with Helium. Phys. Rev., 151(1):14–19, November 1966.
- [106] G. N. Ogurtsov. Auger line shift due to the post-collision interaction at large excess energies. Journal of Physics B: Atomic and Molecular Physics, 16(23):L745–L748, December 1983. Publisher: IOP Publishing.
- [107] A Niehaus. Analysis of post-collision interactions in Auger processes following near-threshold inner-shell photoionization. J. Phys. B: At. Mol. Phys., 10(10):1845–

1857, July 1977.

- [108] K. Helenelund, S. Hedman, L. Asplund, U. Gelius, and K. Siegbahn. An Improved Model for Post-Collision Interaction (PCI) and High Resolution Ar LMM Auger Spectra Revealing New PCI Effects. Physica Scripta, 27(4):245–253, April 1983. Publisher: IOP Publishing.
- [109] A Russek and W Mehlhorn. Post-collision interaction and the Auger lineshape. J. Phys. B: At. Mol. Phys., 19(6):911–927, March 1986.
- [110] P. Straten, R. Morgenstern, and A. Niehaus. Angular dependent post-collision interaction in auger processes. Z Phys D - Atoms, Molecules and Clusters, 8(1):35–45, March 1988.
- [111] G. Bradley Armen, Jukka Tulkki, Teijo Aberg, and Bernd Crasemann. Quantum theory of post-collision interaction in inner-shell photoionization: Final-state interaction between two continuum electrons. Phys. Rev. A, 36(12):5606–5614, December 1987. Publisher: American Physical Society.
- [112] A. K. Kazansky and N. M. Kabachnik. Nonstationary theory for short-pulse near-threshold photoionization of inner atomic shells. Phys. Rev. A, 72(5):052714, November 2005. Publisher: American Physical Society.
- [113] H Kjeldsen, T D Thomas, P Lablanquie, M Lavollée, F Penent, M Hochlaf, and R I Hall. Post-collision interaction effects in near-threshold Ar -shell photoionization. J. Phys. B: At. Mol. Opt. Phys., 29(9):1689–1698, May 1996.
- [114] F. Penent, J. Palaudoux, P. Lablanquie, L. Andric, R. Feifel, and J. H. D. Eland. Multielectron Spectroscopy: The Xenon 4d Hole Double Auger Decay. Phys. Rev. Lett., 95(8):083002, August 2005. Publisher: American Physical Society.
- [115] R. Guillemin, L. Gerchikov, S. Sheinerman, M. Zmerli, T. Marin, L. Journal, O. Travnikova, T. Marchenko, B. Lassalle-Kaiser, M. N. Piancastelli, and M. Simon.

- Photoelectron–Auger-electron angular-momentum transfer in core-ionized Ar: Beyond the standard post-collision-interaction model. Phys. Rev. A, 99(6):063409, June 2019.
- [116] P. Lablanquie, S. Sheinerman, F. Penent, T. Aoto, Y. Hikosaka, and K. Ito. Dynamics of double photoionization near the Ar 2p threshold investigated by threshold electron–Auger electron coincidence spectroscopy. Journal of Physics B: Atomic, Molecular and Optical Physics, 38(1):L9–L18, December 2004. Publisher: IOP Publishing.
- [117] R. Valaski, C.D. Canestraro, L. Micaroni, R.M.Q. Mello, and L.S. Roman. Organic photovoltaic devices based on polythiophene films electrodeposited on FTO substrates. Solar Energy Materials and Solar Cells, 91(8):684–688, May 2007.
- [118] Eduard Nasybulin, Jeremy Feinstein, Marshall Cox, Ioannis Kymissis, and Kalle Levon. Electrochemically prepared polymer solar cell by three-layer deposition of poly(3,4-ethylenedioxythiophene)/poly(2,2-bithiophene)/fullerene (PEDOT/PBT/C60). Polymer, 52(16):3627–3632, July 2011.
- [119] Kang-Jun Baeg, Dongyoon Khim, Dong-Yu Kim, Jae Bon Koo, In-Kyu You, Won San Choi, and Yong-Young Noh. High mobility top-gated poly(3-hexylthiophene) field-effect transistors with high work-function Pt electrodes. Thin Solid Films, 518(14):4024–4029, May 2010.
- [120] S Sheinerman, P Lablanquie, F Penent, J Palaudoux, J H D Eland, T Aoto, Y Hikosaka, and K Ito. Electron correlation in Xe 4d Auger decay studied by slow photoelectron–Auger electron coincidence spectroscopy. J. Phys. B: At. Mol. Opt. Phys., 39(5):1017–1033, March 2006.
- [121] Michael P. Hughes, Katie D. Rosenthal, Niva A. Ran, Martin Seifrid, Guillermo C. Bazan, and Thuc-Quyen Nguyen. Determining the Dielectric Constants of Organic Photovoltaic Materials Using Impedance Spectroscopy. Adv. Funct. Mater.,

28(32):1801542, August 2018.

- [122] Marcus Böckmann, Thomas Schemme, Djurre H. de Jong, Cornelia Denz, Andreas Heuer, and Nikos L. Doltsinis. Structure of P3HT crystals, thin films, and solutions by UV/Vis spectral analysis. Phys. Chem. Chem. Phys., 17(43):28616–28625, 2015.
- [123] Ramadhar Singh, Jitendra Kumar, Rajiv K Singh, Ramesh C Rastogi, and Vikram Kumar. Low frequency ac conduction and dielectric relaxation in pristine poly(3-octylthiophene) films. New J. Phys., 9(2):40–40, February 2007.
- [124] M. Estrada, I. Mejia, A. Cerdeira, and B. Iñiguez. MIS polymeric structures and OTFTs using PMMA on P3HT layers. Solid-State Electronics, 52(1):53–59, January 2008.
- [125] Mustafa Okutan, Yusuf Yerli, S. Eren San, Faruk Yılmaz, Okan Günaydın, and Murat Durak. Dielectric properties of thiophene based conducting polymers. Synthetic Metals, 157(8-9):368–373, May 2007.
- [126] Oksana Travnikova, Minna Patanen, Johan Söderström, Andreas Lindblad, Joshua J. Kas, Fernando D. Vila, Denis Céolin, Tatiana Marchenko, Gildas Goldsztejn, Renaud Guillemin, Loïc Journal, Thomas X. Carroll, Knut J. Børve, Piero Decleva, John J. Rehr, Nils Mårtensson, Marc Simon, Svante Svensson, and Leif J. Sæthre. Energy-Dependent Relative Cross Sections in Carbon 1s Photoionization: Separation of Direct Shake and Inelastic Scattering Effects in Single Molecules. J. Phys. Chem. A, 123(35):7619–7636, September 2019.
- [127] C. Menéndez and F. Guinea. Electron-phonon scattering in polyparaphenylene. Phys. Rev. B, 28(4):2183–2190, August 1983.
- [128] R Mansfield. Impurity Scattering in Semiconductors. Proc. Phys. Soc. B, 69(1):76–82, January 1956.
- [129] A Jablonski. NIST Electron Inelastic-Mean-Free-Path Database - Version1.2, 2010.

Pages: 47.

- [130] A Jablonski. NIST Electron Effective-Absorption-Length Database -Version 1.3, 2011.
- [131] A Jablonski. The electron attenuation length revisited. Surface Science Reports, 47(2-3):33–91, June 2002.
- [132] Dai-Nam Le and Hieu T. Nguyen-Truong. Analytical Formula for the Electron Inelastic Mean Free Path. J. Phys. Chem. C, 125(34):18946–18951, September 2021.
- [133] A. Jablonski. Transport cross section for electrons at energies of surface-sensitive spectroscopies. Phys. Rev. B, 58(24):16470–16480, December 1998.
- [134] S. Tanuma, C. J. Powell, and D. R. Penn. Calculations of electron inelastic mean free paths. V. Data for 14 organic compounds over the 50-2000 eV range. Surf. Interface Anal., 21(3):165–176, March 1994.
- [135] Nenad Vukmirović and Lin-Wang Wang. Electronic Structure of Disordered Conjugated Polymers: Polythiophenes. J. Phys. Chem. B, 113(2):409–415, January 2009.
- [136] Muhammad Azhar Ansari, Shaikh Mohiuddin, Fatma Kandemirli, and Muhammad Imran Malik. Synthesis and characterization of poly(3-hexylthiophene): improvement of regioregularity and energy band gap. RSC Adv., 8(15):8319–8328, 2018.
- [137] Marianne Breinig, Mau Hsiung Chen, Gene E. Ice, Fernando Parente, Bernd Crasemann, and George S. Brown. Atomic inner-shell level energies determined by absorption spectrometry with synchrotron radiation. Phys. Rev. A, 22(2):520–528, August 1980.
- [138] A. P. Hitchcock, J. A. Horsley, and J. Stöhr. Inner shell excitation of thiophene and thiolane: Gas, solid, and monolayer states. The Journal of Chemical Physics,

85(9):4835–4848, November 1986.

- [139] Yunier Garcia-Basabe, Denis Ceolin, Aldo J. G. Zarbin, Lucimara S. Roman, and Maria Luiza M. Rocco. Ultrafast interface charge transfer dynamics on P3HT/MWCNT nanocomposites probed by resonant Auger spectroscopy. RSC Adv., 8(46):26416–26422, 2018.
- [140] Volkhard May and Oliver Kühn. Charge and Energy Transfer Dynamics in Molecular Systems. Wiley-VCH Verlag GmbH & Co. KGaA, 1999.
- [141] Hans Jakob Wörner, Christopher A. Arrell, Natalie Banerji, Andrea Cannizzo, Majed Chergui, Akshaya K. Das, Peter Hamm, Ursula Keller, Peter M. Kraus, Elisa Liberatore, Pablo Lopez-Tarifa, Matteo Lucchini, Markus Meuwly, Chris Milne, Jacques-E. Moser, Ursula Rothlisberger, Grigory Smolentsev, Joël Teuscher, Jeroen A. van Bokhoven, and Oliver Wenger. Charge migration and charge transfer in molecular systems. Structural Dynamics, 4(6):061508, November 2017.
- [142] N. Hartmann, G. Hartmann, R. Heider, M. S. Wagner, M. Ilchen, J. Buck, A. O. Lindahl, C. Benko, J. Grünert, J. Krzywinski, J. Liu, A. A. Lutman, A. Marinelli, T. Maxwell, A. A. Miahnahri, S. P. Moeller, M. Planas, J. Robinson, A. K. Kazan-sky, N. M. Kabachnik, J. Viefhaus, T. Feurer, R. Kienberger, R. N. Coffee, and W. Helml. Attosecond time–energy structure of X-ray free-electron laser pulses. Nature Photonics, 12(4):215–220, April 2018.
- [143] Jie Li, Jian Lu, Andrew Chew, Seunghwoi Han, Jialin Li, Yi Wu, He Wang, Shambhu Ghimire, and Zenghu Chang. Attosecond science based on high harmonic generation from gases and solids. Nature Communications, 11(1):2748, June 2020.
- [144] Joseph C. Genereux and Jacqueline K. Barton. Mechanisms for DNA Charge Transport. Chemical Reviews, 110(3):1642–1662, 2010. _eprint: <https://doi.org/10.1021/cr900228f>.

- [145] Theodore J. Zwang, Edmund C. M. Tse, and Jacqueline K. Barton. Sensing DNA through DNA Charge Transport. *ACS Chemical Biology*, 13(7):1799–1809, 2018. [_eprint: https://doi.org/10.1021/acscchembio.8b00347](https://doi.org/10.1021/acscchembio.8b00347).
- [146] D. Garratt, L. Misiakis, D. Wood, E. W. Larsen, M. Matthews, O. Alexander, P. Ye, S. Jarosch, C. Ferchaud, C. Strüber, A. S. Johnson, A. A. Bakulin, T. J. Penfold, and J. P. Marangos. Direct observation of ultrafast exciton localization in an organic semiconductor with soft X-ray transient absorption spectroscopy. *Nat Commun*, 13(1):3414, June 2022.
- [147] Samuel Andermatt, Jinwoong Cha, Florian Schiffmann, and Joost VandeVondele. Combining Linear-Scaling DFT with Subsystem DFT in Born–Oppenheimer and Ehrenfest Molecular Dynamics Simulations: From Molecules to a Virus in Solution. *Journal of Chemical Theory and Computation*, 12(7):3214–3227, 2016. [_eprint: https://doi.org/10.1021/acs.jctc.6b00398](https://doi.org/10.1021/acs.jctc.6b00398).
- [148] Hiromi Ikeura-Sekiguchi and Tetsuhiro Sekiguchi. Molecular ordering effect of regioregular poly(3-hexylthiophene) using sulfur K-edge X-ray absorption spectroscopy. *Jpn. J. Appl. Phys.*, 53(2S):02BB07, February 2014.
- [149] Faris Gel'mukhanov and Hans Ågren. Raman, non-Raman, and anti-Raman dispersion in resonant x-ray scattering spectra of molecules. *Phys. Rev. A*, 54(5):3960–3970, November 1996.
- [150] P. Hohenberg and W. Kohn. Inhomogeneous Electron Gas. *Phys. Rev.*, 136(3B):B864–B871, November 1964. Publisher: American Physical Society.
- [151] W. Kohn and L. J. Sham. Self-Consistent Equations Including Exchange and Correlation Effects. *Phys. Rev.*, 140(4A):A1133–A1138, November 1965. Publisher: American Physical Society.
- [152] John P. Perdew, Kieron Burke, and Matthias Ernzerhof. Generalized Gradient Ap-

- proximation Made Simple. Phys. Rev. Lett., 77(18):3865–3868, October 1996. Publisher: American Physical Society.
- [153] Stefan Grimme, Jens Antony, Stephan Ehrlich, and Helge Krieg. A consistent and accurate ab initio parametrization of density functional dispersion correction (DFT-D) for the 94 elements H-Pu. The Journal of Chemical Physics, 132(15):154104, 2010. eprint: <https://doi.org/10.1063/1.3382344>.
- [154] Thomas D. Kühne, Marcella Iannuzzi, Mauro Del Ben, Vladimir V. Rybkin, Patrick Seewald, Frederick Stein, Teodoro Laino, Rustam Z. Khaliullin, Ole Schütt, Florian Schiffmann, Dorothea Golze, Jan Wilhelm, Sergey Chulkov, Mohammad Hossein Bani-Hashemian, Valéry Weber, Urban Borštnik, Mathieu Taillefumier, Alice Shoshana Jakobovits, Alfio Lazzaro, Hans Pabst, Tiziano Müller, Robert Schade, Manuel Guidon, Samuel Andermatt, Nico Holmberg, Gregory K. Schenter, Anna Hehn, Augustin Bussy, Fabian Belleflamme, Gloria Tabacchi, Andreas Glöß, Michael Lass, Iain Bethune, Christopher J. Mundy, Christian Plessl, Matt Watkins, Joost VandeVondele, Matthias Krack, and Jürg Hutter. CP2K: An electronic structure and molecular dynamics software package - Quickstep: Efficient and accurate electronic structure calculations. J. Chem. Phys., 152(19):194103, May 2020.
- [155] S. Goedecker, M. Teter, and J. Hutter. Separable dual-space Gaussian pseudopotentials. Phys. Rev. B, 54(3):1703–1710, July 1996. Publisher: American Physical Society.
- [156] Ze-Fan Yao, Qi-Yi Li, Hao-Tian Wu, Yi-Fan Ding, Zi-Yuan Wang, Yang Lu, Jie-Yu Wang, and Jian Pei. Building crystal structures of conjugated polymers through X-ray diffraction and molecular modeling. SmartMat, 2(3):378–387, September 2021.
- [157] Koichi Momma and Fujio Izumi. VESTA3 for three-dimensional visualization of crystal, volumetric and morphology data. Journal of Applied Crystallography, 44(6):1272–1276, December 2011.

- [158] K. Yabana and G. F. Bertsch. Time-dependent local-density approximation in real time. *Phys. Rev. B*, 54(7):4484–4487, August 1996. Publisher: American Physical Society.
- [159] W Tang, E Sanville, and G Henkelman. A grid-based Bader analysis algorithm without lattice bias. *J. Phys.: Condens. Matter*, 21(8):084204, February 2009.
- [160] Jessica B. Martins, Carlos E. V. de Moura, Gildas Goldsztejn, Oksana Travnikova, Renaud Guillemin, Iyas Ismail, Loïc Journal, Dimitrios Koulentianos, Mario Barbatti, Alexandre F. Lago, Denis Céolin, Maria Luiza M. Rocco, Ralph Püttner, Maria Novella Piancastelli, Marc Simon, and Tatiana Marchenko. Electron delocalisation in conjugated sulfur heterocycles probed by resonant Auger spectroscopy. *Phys. Chem. Chem. Phys.*, 24(14):8477–8487, 2022.
- [161] Ralph Püttner, Philippe Holzhey, Mateja Hrast, Matjaz Žitnik, Gildas Goldsztejn, Tatiana Marchenko, Renaud Guillemin, Loïc Journal, Dimitris Koulentianos, Oksana Travnikova, Moustafa Zmerli, Denis Céolin, Yoshiro Azuma, Satoshi Kosugi, Alexandre F. Lago, Maria Novella Piancastelli, and Marc Simon. Argon K L L Auger spectrum: Initial states, core-hole lifetimes, shake, and knock-down processes. *Phys. Rev. A*, 102(5):052832, November 2020.
- [162] Y. Garcia-Basabe, B.G.A.L. Borges, D.C. Silva, A.G. Macedo, L. Micaroni, L.S. Roman, and M.L.M. Rocco. The interplay of electronic structure, molecular orientation and charge transport in organic semiconductors: Poly(thiophene) and poly(bithiophene). *Organic Electronics*, 14(11):2980–2986, November 2013.
- [163] Matheus Jacobs, Jannis Krumland, and Caterina Cocchi. Laser-Controlled Charge Transfer in a Two-Dimensional Organic/Inorganic Optical Coherent Nanojunction. *ACS Applied Nano Materials*, 5(4):5187–5195, 2022. _eprint: <https://doi.org/10.1021/acsanm.2c00253>.
- [164] Basile F. E. Curchod, Ursula Rothlisberger, and Ivano Tavernelli. Trajectory-

- Based Nonadiabatic Dynamics with Time-Dependent Density Functional Theory. ChemPhysChem, 14(7):1314–1340, 2013. _eprint: <https://chemistry-europe.onlinelibrary.wiley.com/doi/pdf/10.1002/cphc.201200941>.
- [165] Jeremy M. Berg, John L. Tymoczko, Gregory J. Gatto, and Lubert Stryer. Biochemistry. W.H. Freeman & Company, a Macmillan Education Imprint, New York, eighth edition edition, 2015.
- [166] Charles R. Cantor and Paul R. Schimmel. Biophysical chemistry. W.H. Freeman San Francisco, San Francisco, 1980.
- [167] Thomas E Creighton. Proteins: structures and molecular properties. Macmillan, 1993.
- [168] Aitor Manteca, Álvaro Alonso-Caballero, Marie Fertin, Simon Poly, David De Sancho, and Raul Perez-Jimenez. The influence of disulfide bonds on the mechanical stability of proteins is context dependent. Journal of Biological Chemistry, 292(32):13374–13380, August 2017.
- [169] Hans Neurath. Protein Structure and Enzyme Action. Rev. Mod. Phys., 31(1):185–190, January 1959.
- [170] Anwar Hossain and Kozi Asada. Purification of Dehydroascorbate Reductase from Spinach and Its Characterization as a Thiol Enzyme. Plant and Cell Physiology, January 1984.
- [171] Makoto Ide, Yasushi Maeda, and Hiromi Kitano. Effect of Hydrophobicity of Amino Acids on the Structure of Water. J. Phys. Chem. B, 101(35):7022–7026, August 1997. Publisher: American Chemical Society (ACS).
- [172] Kathrin M. Lange and Emad F. Aziz. Electronic structure of ions and molecules in solution: a view from modern soft X-ray spectroscopies. Chem. Soc. Rev., 42(16):6840, 2013.

- [173] T. Head-Gordon, J. M. Sorenson, A. Pertsemliadis, and R. M. Glaeser. Differences in hydration structure near hydrophobic and hydrophilic amino acids. Biophysical Journal, 73(4):2106–2115, October 1997. Publisher: Elsevier BV.
- [174] Ralf Ludwig. Water: From Clusters to the Bulk. Angew. Chem. Int. Ed., 40(10):1808–1827, May 2001. Publisher: Wiley.
- [175] Barbara Hribar, Noel T. Southall, Vojko Vlachy, and Ken A. Dill. How Ions Affect the Structure of Water. J. Am. Chem. Soc., 124(41):12302–12311, September 2002. Publisher: American Chemical Society (ACS).
- [176] Alan Cooper. Heat capacity effects in protein folding and ligand binding: a re-evaluation of the role of water in biomolecular thermodynamics. Biophysical Chemistry, 115(2-3):89–97, April 2005. Publisher: Elsevier BV.
- [177] Carla Mattos. Protein–water interactions in a dynamic world. Trends in Biochemical Sciences, 27(4):203–208, April 2002.
- [178] R. Mason. Charge transfer processes in biological systems. Discuss. Faraday Soc., 27:129, 1959.
- [179] Håkan Lepp, Emelie Svahn, Kristina Faxén, and Peter Brzezinski. Charge Transfer in the K Proton Pathway Linked to Electron Transfer to the Catalytic Site in Cytochrome *c* Oxidase. Biochemistry, 47(17):4929–4935, April 2008.
- [180] Meike Cordes and Bernd Giese. Electron transfer in peptides and proteins. Chem. Soc. Rev., 38(4):892, 2009. Publisher: Royal Society of Chemistry (RSC).
- [181] Stephan Eberhard, Giovanni Finazzi, and Francis-André Wollman. The Dynamics of Photosynthesis. Annu. Rev. Genet., 42(1):463–515, December 2008. Publisher: Annual Reviews.
- [182] D. Céolin, N. V. Kryzhevoi, Ch. Nicolas, W. Pokapanich, S. Choksakulporn,

- P. Songsiriritthigul, T. Saisopa, Y. Rattanachai, Y. Utsumi, J. Palaudoux, G. Ohrwall, and J.-P. Rueff. Ultrafast Charge Transfer Processes Accompanying K L L Auger Decay in Aqueous KCl Solution. Phys. Rev. Lett., 119(26):263003, December 2017.
- [183] A. I. Streltsov, N. V. Dobrodey, and L. S. Cederbaum. Charge transfer effects in molecule–negative ion complexes induced by core ionization. The Journal of Chemical Physics, 119(6):3051–3062, August 2003. Publisher: AIP Publishing.
- [184] Nikolai V. Kryzhevoi, Nickolay V. Dobrodey, and Lorenz S. Cederbaum. Charge transfer in the Cl-CO cluster induced by core ionization. The Journal of Chemical Physics, 122(10):104304, March 2005. Publisher: AIP Publishing.
- [185] Nikolai V. Kryzhevoi and Lorenz S. Cederbaum. Competitive charge- and energy-transfer processes following core ionization in the Na-CO cluster. The Journal of Chemical Physics, 123(15), October 2005. Publisher: AIP Publishing.
- [186] Nikolai V. Kryzhevoi, Francesco Tarantelli, and Lorenz S. Cederbaum. Tracing electron solvation in Li-(NH₃)_n clusters with K-shell photodetachment spectroscopy. Chemical Physics Letters, 626:85–89, April 2015. Publisher: Elsevier BV.
- [187] Nikolai V. Kryzhevoi and Lorenz S. Cederbaum. Core ionization of Na⁺ microsolvated in water and ammonia. The Journal of Chemical Physics, 130(8):084302, February 2009. Publisher: AIP Publishing.
- [188] Stephan Thürmer, Sebastian Malerz, Florian Trinter, Uwe Hergenbahn, Chin Lee, Daniel M. Neumark, Gerard Meijer, Bernd Winter, and Iain Wilkinson. Accurate vertical ionization energy and work function determinations of liquid water and aqueous solutions. Chem. Sci., 12(31):10558–10582, 2021.
- [189] Natalie Preissler, Franziska Buchner, Thomas Schultz, and Andrea Lübcke. Electrokinetic Charging and Evidence for Charge Evaporation in Liquid Microjets of Aqueous Salt Solution. J. Phys. Chem. B, 117(8):2422–2428, February 2013.

- [190] Junichi Nishitani, Shutaro Karashima, Christopher W. West, and Toshinori Suzuki. Surface potential of liquid microjet investigated using extreme ultraviolet photoelectron spectroscopy. The Journal of Chemical Physics, 152(14):144503, April 2020.
- [191] Naoya Kurahashi, Shutaro Karashima, Ying Tang, Takuya Horio, Bumaliya Abulimiti, Yoshi-Ichi Suzuki, Yoshihiro Ogi, Masaki Oura, and Toshinori Suzuki. Photoelectron spectroscopy of aqueous solutions: Streaming potentials of NaX (X = Cl, Br, and I) solutions and electron binding energies of liquid water and X⁻. The Journal of Chemical Physics, 140(17):174506, May 2014.
- [192] A. D. Becke. Density-functional exchange-energy approximation with correct asymptotic behavior. Phys. Rev. A, 38(6):3098–3100, September 1988. Publisher: American Physical Society (APS).
- [193] Chengteh Lee, Weitao Yang, and Robert G. Parr. Development of the Colle-Salvetti correlation-energy formula into a functional of the electron density. Phys. Rev. B, 37(2):785–789, January 1988. Publisher: American Physical Society (APS).
- [194] Marcella Iannuzzi, Thomas Chassaing, Thomas Wallman, and Jürg Hutter. Ground and Excited State Density Functional Calculations with the Gaussian and Augmented-Plane-Wave Method. Chimia, 59(7-8):499, July 2005.
- [195] Matteo Cavalleri, Michael Odelius, Dennis Nordlund, Anders Nilsson, and Lars G. M. Pettersson. Half or full core hole in density functional theory X-ray absorption spectrum calculations of water? Phys. Chem. Chem. Phys., 7(15):2854, 2005.
- [196] Matthias Krack, Alfredo Gambirasio, and Michele Parrinello. *Ab initio* x-ray scattering of liquid water. The Journal of Chemical Physics, 117(20):9409–9412, November 2002.
- [197] Ph Wernet, D Nordlund, U Bergmann, M Cavalleri, M Odelius, H Ogasawara, L Å Naslund, T K Hirsch, L Ojamae, P Glatzel, L G M Pettersson, and A Nilsson. The

- Structure of the First Coordination Shell in Liquid Water. Science, 304(5673):995–999, 2004.
- [198] By GERALD LIPPERT, JURG HUTTER, and MICHELE PARRINELLO. A hybrid Gaussian and plane wave density functional scheme. Molecular Physics, 92(3):477–488, 1997. Publisher: Taylor & Francis _eprint: <https://doi.org/10.1080/002689797170220>.
- [199] Shuichi Nosé. A unified formulation of the constant temperature molecular dynamics methods. The Journal of Chemical Physics, 81(1):511–519, July 1984. _eprint: https://pubs.aip.org/aip/jcp/article-pdf/81/1/511/9722086/511_1_online.pdf.
- [200] Cody M. Sterling, Chinnathambi Kamal, Alberto García-Fernández, Gabriel J. Man, Sebastian Svanström, Pabitra K. Nayak, Sergei M. Butorin, Håkan Rensmo, Ute B. Cappel, and Michael Odellius. Electronic Structure and Chemical Bonding in Methylammonium Lead Triiodide and Its Precursor Methylammonium Iodide. J. Phys. Chem. C, 126(47):20143–20154, December 2022.
- [201] Henry B. F. Dixon and Keith F. Tipton. Negatively co-operative ligand binding. Biochemical Journal, 133(4):837–842, August 1973.
- [202] Y. Hikosaka, Y. Velkov, E. Shigemasa, T. Kaneyasu, Y. Tamenori, J. Liu, and F. Gel'mukhanov. X-Ray Absorption Measured in the Resonant Auger Scattering Mode. Phys. Rev. Lett., 101(7):073001, August 2008.
- [203] Ingrid J. Pickering, Roger C. Prince, Thomas Divers, and Graham N. George. Sulfur K-edge X-ray absorption spectroscopy for determining the chemical speciation of sulfur in biological systems. FEBS Letters, 441(1):11–14, December 1998. Publisher: Wiley.
- [204] Joachim Stöhr. NEXAFS Spectroscopy, volume 25 of Springer Series in Surface Sciences. Springer Berlin Heidelberg, Berlin, Heidelberg, 1992.

- [205] Jaeon Chang, Abraham M. Lenhoff, and Stanley I. Sandler. Solvation Free Energy of Amino Acids and Side-Chain Analogues. J. Phys. Chem. B, 111(8):2098–2106, March 2007.
- [206] Shin-Pon Ju, Wen-Jay Lee, Ching-I Huang, Wei-Zen Cheng, and Yong-Ting Chung. Structure and dynamics of water surrounding the poly(methacrylic acid): A molecular dynamics study. The Journal of Chemical Physics, 126(22):224901, June 2007.
- [207] Wenhui Zhou, Runjhun Saran, and Juewen Liu. Metal Sensing by DNA. Chem. Rev., 117(12):8272–8325, June 2017.
- [208] Thressa C. Stadtman. SELENOCYSTEINE. Annu. Rev. Biochem., 65(1):83–100, June 1996.
- [209] Thomas Nauser, Daniel Steinmann, and Willem H. Koppenol. Why do proteins use selenocysteine instead of cysteine? Amino Acids, 42(1):39–44, January 2012.
- [210] Uwe Bergmann, Jan Kern, Robert W. Schoenlein, Philippe Wernet, Vittal K. Yachandra, and Junko Yano. Using X-ray free-electron lasers for spectroscopy of molecular catalysts and metalloenzymes. Nat Rev Phys, 3(4):264–282, March 2021.

Acknowledgments

I would like to express my deepest gratitude and appreciation to the individuals and organizations who have supported me throughout my journey in completing this doctoral thesis. Their unwavering encouragement, guidance, and assistance have been instrumental in shaping this work.

First and foremost, I am profoundly grateful to my supervisor, Tatiana Marchenko, for her exceptional mentorship, patience, and expertise. Her insightful feedback, valuable suggestions, and continuous encouragement have been pivotal in refining the direction and quality of this research. Should I become 1/10 of the scientist she is, I will consider myself content.

I extend my heartfelt thanks to the members of my thesis committee, Bernd Winter, Philippe Wernet, Caterina Vozzi, Jean-Hughes Fillion, and Laurent Nahon, for accepting to participate and evaluate this thesis.

I would also like to extend my appreciation to SMART-X for the (not only) financial support, which enabled me to carry out the necessary experiments, gather data, and attend conferences that contributed to the depth and breadth of this work. Within the SMART-X framework, I would also like to thank the partner institutions, Stockholm University, FASTLITE, CFEL-ATTO group at DESY, MBI in Berlin, and people who hosted and really welcomed me during diverse secondments.

I am indebted to my colleagues and peers, who have provided a stimulating intel-

lectual environment. The exchange of ideas, debates, and discussions have significantly influenced the development of this research. People from LCPMR and Marc Simon's group, from SOLEIL and the GALAXIES beamline, and from my time in Lund, thank you all.

My gratitude goes out to all the collaborators in the projects presented in this thesis, without whom this research would not have been possible. Their willingness to contribute their time and insights has been invaluable.

To my Chilean family, los amo, a pesar de todo! To my Swedish family, svensk mat är mycket bättre än fransk mat.

In closing, I am truly humbled and honored to have been surrounded by such a remarkable network of individuals who have shaped my academic and personal growth.

Sist men inte minst, Kamilla, min kära fru, in the words of the great, late, Peter O'Hanrahan, you didn't like it, but you had to go along with it.

Thank you, merci, gracias, tack.